NASA CONTRACTOR REPORT

NASA CR-25

NASA CR-2563

EXPERIMENTAL EVALUATION OF A MACH 3.5 AXISYMMETRIC INLET

J. Syberg and J. L. Koncsek

Prepared by
BOEING [redacted] COMPANY
Seattle, Wash. 98124
for Ames Research Center

NATIONAL AERONAUTICS AND SPACE ADMINISTRATION • WASHINGTON, D.C.

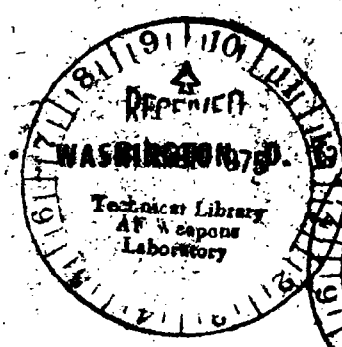

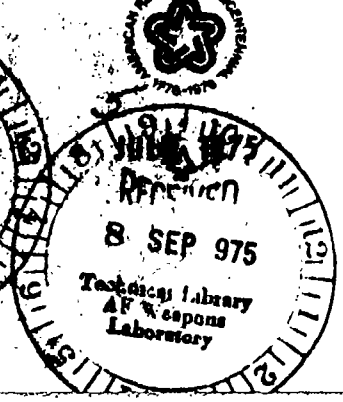

1. Report No.	2. Government Accession No.	3. Recipient's Catalog No.
NASA CR-2563		

4. Title and Subtitle	5. Report Date
"Experimental Evaluation of a Mach 3.5 Axisymmetric Inlet"	July 1975
	6. Performing Organization Code

7. Author(s)	8. Performing Organization Report No.
J. Syberg and J. L. Koncsek	D6-42494
	10. Work Unit No.

9. Performing Organization Name and Address	11. Contract or Grant No.
Boeing Commercial Airplane Company P.O. Box 3707 Seattle, Washington 98124	NAS 2-8236
	13. Type of Report and Period Covered
12. Sponsoring Agency Name and Address	Contractor Report
National Aeronautics & Space Administration Washington, D.C. 20546	14. Sponsoring Agency Code

15. Supplementary Notes

Project Managers: Norman E. Sorensen and Donald B. Smeltzer
Aerodynamcis Branch
NASA, Ames Research Center
Moffett Field, CA

16. Abstract

Wind tunnel test results for a large-scale inlet model designed for Mach 3.5 are presented and compared with analytical predictions. The inlet is an axisymmetric mixed-compression type with a lip diameter of 49.723 cm. The inlet design was developed using analytical procedures. Data are shown for freestream Mach numbers from 0.6 to 3.5. The test results indicate that boundary-layer bleed requirements can be accurately predicted. Good agreement was obtained with analytical predictions of the flowfield structure and boundary-layer development in the supersonic diffuser yielding high performance at the design Mach number. The highest engine-face total-pressure recovery at Mach 3.5 was 85.8%; this was obtained at 0.05 Mach tolerance with only 2.8% total-pressure distortion and 13.4% bleed. In the started Mach number range from 1.6 to 3.5, the total-pressure recovery in the throat, downstream of the terminal normal shock, ranged between 91% and 95%. Total-pressure losses in the subsonic diffuser varied from 3% to 13%. The higher losses occuring between Mach 2.5 and 3.2 were believed to be caused by the rapid rate of increase in the area of the diffuser just downstream of the throat, possibly coupled with inadequate centerbody throat bleed. In the unstarted mode at transonic speeds, the maximum inlet flow was over 99% of the theoretical maximum capture mass-flow.

17. Key Words (Suggested by Author(s))		18. Distribution Statement
Inlets	Axisymmetric	
Boundary layer	Bleed holes	UNCLASSIFIED-UNLIMITED
Bleed systems	Wind tunnel test	
Supersonic		STAR Category 07

19. Security Classif. (of this report)	20. Security Classif. (of this page)	21. No. of Pages	22. Price*
UNCLASSIFIED	UNCLASSIFIED	139	4.75

*For sale by the National Technical Information Service, Springfield, Virginia 22151

CONTENTS

FIGURES

FIGURES (Concluded)

TABLES

EXPERIMENTAL EVALUATION OF A MACH 3.5 AXISYMMETRIC INLET

By J. Syberg and J. L. Koncsek
The Boeing Company

SUMMARY

Wind tunnel test results for a large-scale inlet model designed for Mach 3.5 are presented and compared with analytical predictions. The inlet is an axisymmetric mixed-compression type with a lip diameter of 49.723 cm. The inlet design was developed using analytical procedures based on method-of-characteristic solutions of supersonic stream flows and finite difference calculations of boundary-layer development. Empirical coefficients were used in modeling the boundary-layer control system. This work is described in reference 1.

Test results are shown for a freestream Mach number range of 0.6 to 3.5. The test results agreed well with analytical predictions of the flowfield structure and boundary-layer development in the supersonic diffuser. The bleed flow rate requirements were accurately predicted. The empirical bleed hole flow coefficients used in the design were found to be somewhat optimistic. The best performance was obtained after the bleed area was enlarged to increase the bleed rates to the predicted requirements. The highest engine-face total-pressure recovery at Mach 3.5 was 85.8%. This recovery was obtained at a 0.05 Mach number tolerance with only 2.8% total-pressure distortion and 13.4% bleed.

The design point performance is higher by about 3% recovery for the same amount of bleed than that obtained by NASA on another inlet designed for Mach 3.5 (ref. 2). To our knowledge, the NASA inlet was the highest performance inlet previously tested at this Mach number. It is significant that the present inlet performed better than the NASA inlet at the design point with the predicted bleed configuration demonstrating the validity and usefulness of the analytical design process. The performance was later slightly improved to the level previously described by a minor change in bleed distribution and by the addition of centerbody vortex generators.

In the started Mach range from 1.6 to 3.5, the total-pressure recovery in the throat downstream of the terminal normal shock ranged between 91% and 95%. Total-pressure losses in the subsonic diffuser were 3% to 13%. The highest losses occurred between Mach 2.5 and 3.2 and were believed to be caused by the rapid rate of increase in area of the diffuser just downstream of the throat. The solution to this problem appears to be a redesign of the subsonic diffuser to improve the area distribution for extended centerbody positions, possibly combined with a redesign of the centerbody throat bleed system to improve the control of the interaction of the normal shock with the boundary layer. Note, however, that any change made in the subsonic diffuser to significantly reduce the rate of diffusion will also reduce the transonic flow capacity of the inlet.

In the unstarted mode at transonic speeds, the maximum inlet flow was over 99% of the theoretical maximum capture flow. In this mode the geometric throat area is 42.39% of the cowl lip area. The transonic performance of the inlet was favorably affected by boundary-layer bleed and was adversely affected by inactive bleed holes and vortex generators.

INTRODUCTION

The development of bleed systems for boundary-layer control in supersonic inlets has in the past depended mainly on extensive wind tunnel tests. The tests were complex, time consuming, and did not always allow optimization of the system. An analytical procedure has been developed for the design of bleed systems based on theoretical analysis and experimental data. Using the procedure allows analytic definition of a bleed system, which may then be optimized in the wind tunnel with less testing. Portions of the procedure and technology had been applied previously (refs. 3 and 4) but not as an entire package.

The procedure was applied recently to the design of a bleed system for an inlet designed for Mach 3.5 with the objective of providing satisfactory operation across a wide range of "started" Mach numbers with adequate tolerance to transient disturbances in freestream Mach number, angle of incidence, and engine-face corrected-weight flow. The work included the design of internal cowl and centerbody contours, design of the bleed pattern, bleed hole geometry, bleed plenum arrangement, bleed flow ducting and exits, and the prediction of bleed system performance. This work was carried out under contract NAS2-6643 (ref. 1).

The application of the procedure was the first time a completely analytical design of the bleed system had been done prior to model testing. As such, the main objective of the wind tunnel test was a thorough validation of the procedures. This document describes the results from a test conducted in the NASA-Ames Unitary Plan Wind Tunnels with a large-scale model of the M = 3.5 inlet. Comparisons of test data and analytical predictions are included.

The inlet was tested at freestream Mach numbers from 0.6 to 3.5. The corresponding Reynolds numbers based on the cowl lip diameter ranged from 2.8×10^6 at Mach 3.5 to about 7×10^6 of the transonic and subsonic Mach numbers. The angle-of-attack range for the test was 0° to 5° at the high supersonic Mach numbers and 0° to 8° at the lower Mach numbers.

SYMBOLS AND ABBREVIATIONS

A	Area
A/A_*	Sonic area ratio
A_{BLOCK}	Area equal to the reduction in effective throat area due to boundary-layer blockage
A_{BT}	Total bleed plenum exit area
A_{EFF}	Effective flow area
A_H	Bleed hole area
A_L	Cowl lip area = 0.1942 m^2
C_m	Inlet capture flow coefficient with the inlet in the external compression mode, $W_C/(\rho_* V_*)_\infty A_{TH}$
C_{WE}	Engine-face mass-flow corrected to standard sea level conditions
D	High frequency dynamic total-pressure probe
H_i	Boundary-layer shape factor
h_{TH}	Distance from cowl surface to centerbody surface at the throat station
L	Axial distance in subsonic diffuser from throat station
M	Freestream Mach number
M_L	Local Mach number
P	Static pressure
P_P	Pitot pressure
P_{PL}	Plenum pressure
P_T	Total pressure
$P_{T_{AV}}$	Area weighted average total pressure at engine face
$P_{T_{MAX}}$	Maximum individual total-pressure probe reading at engine face
$P_{T_{MIN}}$	Minimum individual total-pressure probe reading at engine face

P_{To}	Freestream total pressure
Q	Bleed hole mass-flow coefficient, $W/(\rho_* V_*)_\infty A_H$
R	Radius
$(Re_\theta)_{TR}$	Transition Reynolds number based on boundary-layer momentum thickness
R_L	Cowl lip radius = 24.86 cm
rms	The root mean square value of the time-varying component of the total pressure using a time period of one second
U/U_e	Ratio of the local velocity in the boundary layer to the velocity at the edge of the boundary layer
VG	Vortex generator
V_*	Velocity at sonic conditions
V_∞	Freestream velocity
W	Mass flow
W_{BT}	Total bleed mass-flow
W_C	Mass-flow captured by inlet
W_L	Lip mass-flow, $\rho_\infty V_\infty A_L$
X	Inlet station, referenced to tip of centerbody in design position
X_{CB}	Centerbody station, referenced to tip of centerbody
$(X/R_L)_{TR}$	Inlet station at which transition was predicted
Y,y	Distance from surface, used as boundary-layer profile coordinate
α	Model angle of attack
ΔC_{WE}	Difference between the engine-face corrected flow and the critical corrected flow for the same Mach number and centerbody position
ΔM	Mach number tolerance
$\Delta X/R_L$	Forward translation of the centerbody position from the design position normalized to the lip radius

δ	Boundary-layer thickness
δ^*	Boundary-layer displacement thickness
θ	Boundary-layer momentum thickness
ρ_*	Density at sonic conditions
ρ_∞	Freestream density
ρ/ρ_e	Ratio of the local density in the boundary layer to the density at the outer edge of the boundary layer

Subscripts:

C0	Cowl plenum 0
C1	Cowl plenum 1
C2	Cowl plenum 2
C3	Cowl plenum 3
CRIT	Critical inlet condition
D1	Centerbody support tube duct no. 1
D2	Centerbody support tube duct no. 2
D3	Centerbody support tube duct no. 3
MAX	Maximum
TH	Throat
∞	Freestream condition

TEST APPARATUS AND DATA REDUCTION

MODEL DESCRIPTION

A brief description of the physical features of the model is given here. The model design and design philosophy are summarized later in this report and are discussed in detail in reference 1.

Photographs of the model and model details are presented in figures 1 and 2. The inlet geometry is shown schematically in figure 3. The design contains three basic subsystems as follows:

1. The cowl assembly includes four bleed plenums with separate overboard exits for each plenum.

2. The centerbody assembly includes 12 bleed plenums and a slotted support tube in a "traveling" bleed arrangement. The centerbody support tube contains three ducts that remain separated through the support struts to separate overboard exits at the ends of the struts.

3. The inlet aft assembly guides the flow to the engine face and the secondary air ducts. Excess inlet airflow can be exited overboard through the bypass doors.

The inlet was coupled to a sting-mounted flow duct assembly with a variable plug valve at the aft end to simulate the flow demand of a jet engine (main duct flow).

The flow duct assembly, the inlet aft assembly, and the external cowl shell, including the structural members and the cowl bleed exit louvers, are the same hardware that were used in previous tests described in references 3 and 4. The internal cowl skin, the centerbody assembly, and the centerbody bleed exit nozzles were fabricated for the present test under contract NAS2-7640.

The present M = 3.5 inlet model is thus sized to mate to an existing inlet aft assembly and external cowl shell originally designed for the M = 2.65 inlet. Consequently, the lip and throat areas are too small relative to the compressor face area for a typical turbojet application. This produces a subsonic diffuser area ratio that is somewhat higher than those used on other M = 3.5 inlet models described in the literature. The diffuser area ratio at the design Mach number is about 5.0 to 1 for the present inlet model compared to about 3.5 to 1 for the NASA inlet (ref. 2).

The cowl lip diameter is 49.723 cm. Surface contours of the centerbody and internal cowl are listed in table 1. At the design Mach 3.5, the centerbody is in the fully retracted position ($\Delta X/R_L = 0$) providing a capture mass-flow ratio of unity. During operation at lower Mach numbers, the centerbody translates forward, thereby increasing the throat area to maintain the desired throat Mach number. During started operation, the geometric throat remains fixed on the cowl. This is a result of the design requirement of achieving the largest possible transonic flow capacity with this inlet. Because the throat moves aft on the centerbody as

the centerbody translates forward, a traveling bleed system was required. This provides bleed in the throat as well as near the oblique shock reflections in the supersonic diffuser at all conditions. Figure 4 illustrates the centerbody bleed schedule. The model stations and the diameters of the bleed holes in the individual cowl and centerbody bleed plenums are given in table 2. The variation in bleed hole diameter from bleed band to bleed band is a unique feature of the bleed system. This was done to achieve the desired bleed hole areas (i.e., bleed rates) while maintaining a hole spacing approximately equal to the hole diameter in each bleed band. A photograph of the centerbody forward bleed holes is shown in figure 2a.

The data obtained with the boundary-layer rakes were of fundamental importance in comparing the test results to analytical predictions. The rakes were designed for installation in quick disconnect sockets mounted flush with the surface, allowing the rakes to be changed easily, and thereby minimizing the loss of data because of damaged probes. Figure 2b shows a typical rake installation. The probes were made of 0.025-cm inside diameter tubing. The inner three probes were flattened to 0.01-cm inside dimension to improve the accuracy of measurement in the high velocity gradient part of the boundary layer near the surface.

MODEL INSTRUMENTATION AND CONTROL SYSTEMS

The model instrumentation consisted of pitot-pressure rakes and surface static taps. A total of 366 steady-state pressures were recorded for each correlation point. In addition, rms values from six dynamic pitot probes at the engine face were recorded. To detect possible unsteady flow behavior in the inlet, a cowl surface dynamic pressure was monitored. Pitot-pressure rakes were installed at the engine face and in the flow duct assembly. Five boundary-layer rakes were installed on the cowl and five on the centerbody. Two rakes were installed across the inlet primary flow duct near the cowl lip to calibrate the transonic flow. Locations and dimensions of the rakes are listed in table 3. Eighty surface static-pressure taps were located on the cowl and 41 taps on the centerbody and support tube. In addition, pressures were measured in the bleed plenums, the centerbody bleed ducts, and the bleed exits.

All pressures were read by scanivalves located within the model. The analog signals from the scanivalves and model position sensors were converted to digital output by the wind tunnel data system and transmitted to the central computer for processing.

The centerbody, the flow duct plug, the secondary air butterfly valves, and the bypass doors were positioned with electrohydraulic servocontrollers. The compressor face rotating total-pressure rakes were positioned with an electrical servosystem. All systems were operated remotely from a control console. Additional details of the model, the model control system, and the instrumentation and the data systems are described in reference 5.

DATA REDUCTION

The raw test data were processed by the central computer at the test site using a data reduction computer program designed specifically for this test. All pressures were nondimensionalized by dividing by wind tunnel total pressure. The data reduction program

contained subroutines to calculate the primary inlet flow, the secondary air flow, and the individual bleed exit flows. The various flow rates were calculated by the computer using the appropriate pressure and area parameters and previously defined calibration tables contained within the data reduction program. The compressor face total-pressure recovery and distortion, and various averaged pressures were also calculated. Pertinent model position parameters and tunnel conditions were also recorded.

Three additional computer programs were written to automate the final analysis of the computed data stored on magnetic tapes. The programs can be run from a remote keyboard terminal and require as inputs only the correlation point identification numbers and a code for the type of analysis desired. The first program reads the compressor fact total-pressure array; using an existing routine, it constructs isobar contour maps of the array. The second program has an on-line plotting capability with a cathode-ray tube display. The following plot options are available:

- Compressor face recovery, distortion, and total bleed versus Mach number
- The same parameters versus compressor face corrected flow
- Cowl or centerbody static-pressure profile versus inlet station
- Cowl or centerbody boundary-layer pitot-pressure profiles versus probe position
- Individual or average compressor face total-pressure rake profiles

Since several correlation points may be superimposed on the same plot, the effects of changes in configuration or test condition can be readily evaluated. This program was used primarily to screen the data for further analysis. Pertinent machine plots are contained in reference 6. These supplementary plots were assembled under a separate cover to provide access to the detailed data without unduly increasing the volume of the present report.

The third program reads the boundary-layer pitot-pressure data; using an existing routine, it calculates the local flow velocities. The program then fits a profile to the velocity points based on the law of the wall and the law of the wake. From the fitted profile, the skin friction and the boundary-layer integral properties are calculated; i.e., displacement, momentum, energy thicknesses, and shape factors. The automated analysis makes it possible to evaluate large volumes of data in a short time and thus present a comprehensive picture of the test results.

For the comparison of the predicted and measured boundary-layer properties, the following parameters are of prime interest (see ref. 1):

Displacement thickness

$$\delta^* = \int_0^{\delta} \left(1 - \frac{\rho U}{\rho_e U_e}\right) dy$$

Shape factor

$$H_i = \frac{\int_0^{\delta} \left(1 - \frac{U}{U_e}\right) dy}{\int_0^{\delta} \frac{U}{U_e}\left(1 - \frac{U}{U_e}\right) dy}$$

The shape factor is similar to the conventional parameter, δ^*/θ, except that in the calculation of H_i, the density terms have been eliminated. Thus for the Mach range of interest, H_i is essentially independent of the edge Mach number and the wall temperature recovery, and is as such a more useful indicator of the boundary-layer profile distortion. An H_i value above 1.8 corresponds to a highly distorted velocity profile, and the boundary-layer program will usually indicate separation if H_i exceeds a value of about 2.0. A "full" profile, similar to a one-seventh power law profile $\left[U/U_e = (y/\delta)^{1/7}\right]$, corresponds to $H_i = 1.28$. H_i and δ^*, as computed from the theoretical velocity profiles, were the primary parameters used in designing the bleed system. The experimental values were calculated from velocity curves fitted to the test data.

ANALYTICAL INLET DESIGN

PROCEDURE

The first step in the bleed system design procedure for a new inlet contour is to determine a centerbody translation schedule versus freestream Mach number that will provide efficient internal compression with adequate tolerance to unstarting caused by transient changes in Mach number and angle of incidence. These requirements can be met by maintaining the throat Mach number near 1.25 in the started Mach range.

Once the translation schedule has been established, the inviscid flow field is calculated using a method-of-characteristic program at small Mach number increments over the started Mach number range. The surface static-pressure distributions are plotted along with the characteristic network and shock-wave pattern. A map of surface static pressure versus centerbody translation or freestream Mach number is made to facilitate selection of bleed areas in regions of high static pressure. (High surface static pressures allow high bleed plenum pressures and, therefore, low bleed drag.) The surface Mach number distributions from the inviscid flow solutions are used as input for the boundary-layer calculations.

A computer program (ref. 7) is used to calculate the boundary-layer development without bleed along the cowl and centerbody for the predicted inviscid flow field. The program calculates boundary-layer profile distortion parameters along the surfaces, which are mapped versus centerbody translation and freestream Mach number for both the cowl and centerbody (figs. 5 and 6). These maps are then used to identify regions of high profile distortion (i.e., regions where boundary-layer separation is likely) and to determine bleed locations for optimum boundary-layer control.

When locating bleed regions, because of the finite cowl lip bluntness and displacement effects of the boundary layer, an additional consideration is that shock reflections and pressure gradients move forward in the actual inlet as compared to the inviscid calculation. Thus, if the boundary-layer analysis indicates that bleed is required in a given pressure gradient location or just ahead of a shock wave, the bleed is moved slightly forward.

Next, several alternate bleed configurations are studied at the design Mach number. For each of these configurations, the boundary-layer development is computed with bleed included. For the critical normal shock position, essentially all boundary-layer control upstream of the normal shock must come from forward bleed; thus, throat bleed is not included. On the basis of results obtained from these calculations, the design Mach number bleed system is modified to produce the lowest throat boundary-layer distortion and displacement thickness at the lowest possible bleed rates subject to the aforementioned constraints on bleed location. Knowing the bleed locations, flow rates, and local surface Mach numbers, the required bleed hole areas can be calculated for the selected hole angles.

Throat bleed rates are selected on the basis of past experience. Basically, the throat bleed rate required for normal shock/boundary-layer interaction control and good subsonic diffuser performance has been found to be a function of the throat blockage remaining aft of the selected forward bleed. An off-design bleed system that is compatible with the design

Mach number system is planned based on off-design requirements. Using the surface pressure and boundary-layer distortion maps, probable off-design problem areas are determined. Selected off-design cases are then run with various bleed configurations to cover the suspected problem areas. Results from these runs are used to modify and improve the system for off-design operation, possibly requiring modifications to the design Mach number bleed system.

This last step completes the definition of the entire bleed system. At this point the bleed rates and maximum allowable plenum pressures are determined for the remaining range of operation. The boundary-layer characteristics are then computed with bleed rates at small Mach number increments. If these calculations identify any new problem areas not previously anticipated, modifications of the bleed system are undertaken.

The combined flowfield analysis (ref. 8), an inviscid-viscous flowfield solution, is used to evaluate the effects of boundary layer and bleed on the flow field (whether the bleed is properly positioned to control the pressure gradients and shock reflections) and to check on the validity of the final bleed system design. Cases were run at Mach 3.5 and 2.7 for this bleed system checkout.

PREDICTIONS

The analytical predictions for the present inlet are described in detail in reference 1. These predictions are summarized below; however, for a complete understanding of the present report, it is recommended that reference 1 be carefully studied.

The results for the cowl bleed system are presented in a boundary-layer shape factor map in figure 7. As discussed under the "Procedure" section, only forward bleed is included in this analysis. The solution stops with a prediction of separation at the relatively strong second cowl shock reflection between Mach 2.8 and 3.4. Since the upstream H_i is low over this entire range, the separations are expected to be small with rapid redevelopment or to be contained within the shock/boundary-layer interaction. In addition, the shock reflection is close to the throat and thus subject to throat bleed control. As a result, little or no degradation of inlet performance is expected. The solution extends past the cowl throat over the remainder of the started Mach range, except at Mach 1.6. The only regions of high H_i are behind shock reflections (and of course behind the point of transition), and these redevelop rapidly to acceptably low values. The throat profiles are good with low H_i below Mach 2.8 and are probably also satisfactory between Mach 2.8 and 3.4. The second cowl shock reflection near Mach 3.5 is just ahead of the throat with resulting high H_i values. Figure 7 illustrates that the downstream redevelopment is rapid in this Mach number range. (H_i drops rapidly from 1.7.) In the actual inlet, this shock reflection will be moved forward because of cumulative viscous effects. This greater length for redevelopment will improve the throat H_i. Additionally, cowl throat bleed will be active in this region to provide profile improvement. Because of these effects, no problems are expected on the cowl in the throat region.

Figure 8 presents a map of boundary-layer H_i on the centerbody with the analytically designed bleed system. The centerbody boundary layer is predicted to separate upstream of the throat at several Mach numbers at the relatively strong second or third centerbody shock

reflections. The third shock reflection also produces subsonic flow in the reflection for Mach 1.8 to 2.0 and for Mach 2.9. These separations are expected to be small, to be contained within the shock/boundary-layer interaction, or to be reattached very quickly with rapid boundary-layer redevelopment, particularly since for all these cases, the bleed system provides for upstream profiles that generally have low H_i, indicating a "full" profile. Additionally, the solutions are generally close to the throat before separation is encountered. It is expected that these problems will result in little or no degradation of inlet performance. Figure 8 also shows that there are no regions of excessive profile distortion (high H_i) except behind oblique shock reflections. It may be seen that rapid boundary-layer redevelopment occurs in these regions and H_i returns to acceptable levels quite rapidly. Similar maps were developed for the boundary-layer displacement thickness shown in figures 9 and 10.

SUPERSONIC DIFFUSER PERFORMANCE

The primary objective of the present test program is to verify the analytical procedures used in the design of the supersonic diffuser. A detailed comparison of data with analytical results is presented in this section. Comparisons are made for the oblique shock system, the boundary-layer development, the bleed rates, and the throat recovery. For these data, the inlet normal shock is located far downstream of the throat so as to not obscure the performance of the supersonic diffuser. The test results obtained with the normal shock at or near the critical position are presented in later sections.

OBLIQUE SHOCK WAVE STRUCTURE

Since the various bleed plenums are positioned primarily to control oblique shock wave interactions, the actual locations of these interactions become a vital part of the evaluation of the bleed system design. The locations of the oblique shock reflections in the supersonic diffuser were estimated from the experimental static-pressure profiles at each 0.10 increment in Mach number between 1.6 and 3.5 for the primary bleed configuration. Comparisons with predictions from the inviscid analysis are shown in figures 11 and 12. The experimental shock locations generally occur slightly forward of the inviscid locations. This discrepancy, which results from the build-up of boundary layer on the inlet surfaces, was anticipated in the bleed system design (ref. 1, p. 5). Note in figure 12 that the third centerbody shock is very close to the predicted shock in the Mach range of 2.2 to 2.6, whereas it moves somewhat ahead of predicted shock below Mach 2.2 and above 2.6. This can be correlated with the shock reflection pressure ratios shown in figures 10 and 11 of reference 1. The predicted pressure ratios are relatively low for all shock reflections between Mach 2.2 and 2.6, while high pressure ratio shocks occur both below Mach 2.2 and above 2.6. The validity of using the inviscid shocks in the bleed design seems to be a function of the strength of the oblique shock system.

As described in reference 1, a combined inviscid/viscous flowfield analysis was conducted at Mach 3.5 and 2.7. Comparisons of the experimental static-pressure profiles with predictions from the inviscid as well as the combined analysis are presented in figures 13 and 14. The combined analysis, which takes into account the boundary-layer growth and bleed flow removal, closely predicts the forward displacement of the primary shock system and the existence of secondary waves.

Evidently using the inviscid flowfield analysis, as outlined previously in the "Analytical Inlet Design" section, is sufficient for locating the bleed regions if allowances are made for boundary layer and bleed based on prior experience and if the shock system strength stays within reasonable limits. However, the more time-consuming combined analysis provides a more precise picture of the actual flowfield structure.

BOUNDARY-LAYER DEVELOPMENT

The analytically designed bleed configuration (conf. 1) was tested in 0.10 Mach number increments between 1.6 and 3.5 to obtain a detailed comparison with the predicted boundary-layer properties and bleed rates in the supersonic diffuser of the inlet. Figure 15

shows the theoretical and experimental boundary-layer shape factors H_i and displacement thicknesses δ^* for the cowl and the centerbody at the design Mach number. As predicted, the boundary layer is well controlled with the analytically designed bleed system, and the goal of providing a "full" profile ($H_i \sim 1.28$) in the inlet throat is achieved on both surfaces. Thus, the boundary layer should be able to withstand the pressure rise from the normal shock without severe flow separation. This hypothesis is verified and later discussed in the "Started Inlet Performance" section.

Note in figure 15 that the boundary-layer properties evidently are predicted somewhat conservatively in the upstream portion of the diffuser (rake 1), whereas excellent agreement is observed further downstream. Part of the discrepancy at rake 1 may be due to boundary-layer transition occurring further downstream than predicted. The boundary-layer program requires an input to trigger transition. Prior experience with supersonic inlets installed in the NASA-Ames Unitary Plan Wind Tunnels indicated that laminar to turbulent transition can be assumed to occur when the Reynolds number Re_θ based on laminar momentum thickness reaches a value of 400 on the cowl and 600 on the centerbody cone. To study the effect of delayed transition, an analysis was conducted at Mach 3.5 using $Re_\theta = 800$ for transition on both the cowl and the centerbody. These results are compared with the experimental values in figure 16. The predicted boundary-layer shape factors on the forward rakes are still too high, but agreement with the displacement thickness is much better. It should be noted that the boundary-layer shape factor further downstream is only slightly affected by the increased transition Reynolds number despite the thinner boundary layers. As a result, the design analysis would have produced basically the same bleed system with slightly reduced bleed rates with a transition Reynolds number of 800.

Comparisons of predicted and experimental boundary-layer properties at the boundary-layer rake stations are presented in figures 17 through 20 for the started Mach range 1.6 to 3.5. Typical profiles, "full" as well as highly distorted, are shown in figures 21 and 22. The following conclusions are drawn:

Cowl rake 1—This rake is located between cowl bleed plenums 0 and 1. The experimental displacement thicknesses (fig. 17) are only about 50% of the predicted values. As previously discussed, this problem may be related to the transition criterion used in the analytical design. The shape factor (fig. 18) agrees well with predictions at the low Mach numbers but is better than predicted at the high Mach numbers, especially when the first cowl shock reflection moves downstream of the rake at about Mach 3.0. This difference in profile shape between prediction and experiment is discussed later.

Cowl rake 2—This rake is located immediately downstream of bleed plenum 1. The measured δ^* is still somewhat thinner than predicted, while the shape factors agree well throughout the Mach number range. Note that H_i never exceeds 1.30 indicating a well controlled boundary layer.

Cowl rake 3—This rake is located downstream of bleed plenum 2. Since the inlet throat moves ahead of this location below Mach 3.3 (see fig. 7), predictions are available only near the design Mach number. Again, the boundary layer

is well controlled throughout the Mach range. At Mach 3.4, the shape factor is higher than predicted because the second shock reflection has moved upstream from the predicted inviscid position and is located very close to the boundary-layer rake station (see fig. 11).

Cowl rake 4—This rake is located just downstream of the cowl throat plenum (plenum 3) and thus downstream of the throat. The boundary-layer profiles measured at this station have very high velocity gradients near the wall followed by very low gradients in the outer portion of the boundary layer (see fig. 21). It was difficult to curve fit this type of data with the wall-wake profile used for the data reduction. Data are, therefore, shown only where reasonably good profile fits were obtained. It can be concluded, however, that the desired boundary-layer condition (i.e., $H_i < 1.3$) is provided in the throat throughout the Mach range by the cowl boundary-layer bleed system.

Centerbody rake 1—This rake is located upstream of the first centerbody bleed plenum. The results are similar to the results discussed for cowl rake 1. The discrepancy in displacement thickness is also believed to be related to the transition criterion used in the analytical design procedures.

Centerbody rake 2—This rake is located between plenums F1 and F2. Since plenum F1 is active only between Mach 3.2 and 3.5, no bleed is located upstream of rake 2 below Mach 3.2 ($\Delta X/R_L > 0.30$). Higher than predicted H_i values are measured between Mach 1.8 and 2.0 when the rake is located within the first shock interaction (see fig. 12). Good agreement is obtained at the higher Mach numbers.

Centerbody rake 3—This rake is located just downstream of bleed plenum F2, which becomes active for $\Delta X/R_L \leqslant 0.72$ ($M \geqslant 2.6$). Good agreement with predictions is obtained at this station both with the F2 bleed opened and closed. It will be shown later that the slightly higher H_i values at the low Mach numbers are caused by the roughness from the inactive holes in plenums F1 and F2. (The roughness was not accounted for in the analysis.)

Centerbody rake 4—This rake is located between plenums T1 and T2 and in the throat at Mach 3.5 but moves upstream in the supersonic diffuser as the centerbody translates forward for off-design operation. Between Mach 3.1 and 3.3, it is located just downstream of the second shock reflection for which separation was predicted in the $M = 2.9$ to $M = 3.3$ range. High H_i values are measured in this range. Below Mach 2.9, H_i is higher than predicted, again largely as a result of the roughness from the inactive holes. However, the displacement thicknesses agree well with the predicted values.

Centerbody rake 5—This rake is located between plenums T2 and T3 and translates upstream of the throat below Mach 3.3. However, predictions are available only up to Mach 2.9 because of the predicted separation of the second shock. Note that the H_i values in the Mach range of 2.9 to 3.3 are low compared to the H_i values from rake 4 indicating a rapid redevelopment of the boundary layer downstream of the high pressure ratio second shock (see fig. 22). Below Mach 2.9, the experimental H_i values are close to predictions except between Mach 2.2 and 2.4 where the rake is located in the vicinity of the second shock reflection (see fig. 12).

BLEED SYSTEM PERFORMANCE

The preceding section presented a comparison of the experimental and predicted boundary-layer properties in the supersonic diffuser of the inlet. Since the boundary-layer development is strongly dependent on the bleed system, the comparison is meaningful only when combined with a comparison of measured and predicted bleed rates.

The bleed flow requirements are determined from the analytical boundary-layer development (described in ref. 1). Predictions of bleed area requirements are based on the analytical inviscid surface static pressures and empirical bleed hole flow coefficients. Differences between theoretical and experimental bleed rates can be caused by differences in the surface static pressures as well as differences in the flow coefficients.

To determine the local flow conditions and help in visualizing the flow phenomena in the bleed regions, detailed static-pressure plots were prepared for each test Mach number between 1.6 and 3.5. A sample of these plots for the cowl is shown in figure 23. The vertical bars indicate the locations of the bleed holes in the three forward cowl bleed plenums, and the height of the bars indicates the total pressures measured in the bleed plenums. The static-pressure taps located near the bleed holes are strongly affected by the bleed flow and show a marked decrease in pressure, probably due to local curvature of the streamlines. However, since the empirical bleed hole flow coefficients are based on zero-pressure-gradient (flat plate) data ignoring the surface pressure drop within the bleed region, these pressures will also be ignored for the present comparison of predicted and measured static pressures. At the lower Mach numbers, regions of rapid expansion and weak shocks occur near cowl plenums 1 and 2 causing wide fluctuations of static pressure in these regions. These waves can be traced to originate in regions of concentrated bleed on the centerbody. Thus in many cases it becomes difficult to determine the effective surface static pressure seen by the bleed holes in plenums 1 and 2.

Figures 24 through 26 present a comparison of measured and predicted bleed rates and surface static pressures for the three forward cowl plenums. The surface pressures for plenum 0 (fig. 24) are accurately predicted throughout the Mach number range, while the bleed rates are about 30% below the predicted values between Mach 2.7 and 3.5. When the first shock moves in front of the bleed plenum below Mach 2.7, the bleed rates agree with the predictions.

Two sets of pressures are shown for plenum 1 (fig. 25) since this plenum in the analytically designed bleed configuration (conf. 1) has two bands of open holes. These bands are 2.5 cm apart and are often located in significantly different static-pressure fields (see fig. 23). The experimental static pressures and bleed rates are generally in good agreement with predictions, except below Mach 2.1. The bleed rates shown below Mach 2.1 may be somewhat in error because of unchoking of the bleed exits (indicated by bleed exit static pressures), which can possibly explain the low bleed rates.

It is evident from figure 23 that the surface pressures seen by the bleed holes in plenum 2 are difficult to define because of the strong pressure gradients usually present in this region and the strong influence of the boundary-layer suction on the static pressures as mentioned previously. Figure 26 shows the estimated average pressures compared to those used in the analytical bleed system design. While the pressures are in reasonable agreement with the predicted values, the bleed rates are about 30% lower than expected throughout the Mach number range. Part of this discrepancy may be linked to the fact that this bleed region consists of four closely spaced rows of holes that remove a large percentage of the boundary layer (about 30% at M = 3.5). The rapid turning of the flow decreases the static pressures on the aft holes to an extent that possibly should have been taken into account in the analytical design of this bleed region. That is, the estimated average pressure across the bleed holes should have been reduced leading to a larger bleed hole area to obtain the desired bleed flow rate.

A similar comparison of experimental and predicted bleed rates for the centerbody is discussed later. Due to the complexity of the traveling bleed system, it may be helpful for the reader to frequently refer back to the bleed schedule shown in figure 4, but a thorough study of reference 1 is recommended to fully understand the centerbody bleed system.

A sample of the detailed centerbody surface static-pressure plots that were prepared at each test Mach number is shown in figure 27. The bars again indicate the locations of the active forward bleed holes, and the height of the bars indicates the pressures measured in the bleed plenums. Note that the bleed plenum pressures in a few cases are equal to or only slightly below the surface static pressures, suggesting unchoked bleed holes. This will occur either when the opening between the bleed plenum and the support tube duct is too small to pass the choked bleed-hole flow or when the bleed duct exit is too small to pass all of the flow from the various plenums connected to that duct. A typical example of the latter is seen at Mach 2.7. Plenums F2, T1, and T4 are connected to support tube duct D2. However, the total pressure required in the duct to remove all of the bleed from these plenums is too high to allow choked operation of the holes in F2. The duct is pressurized by the bleed from T1 and T4 increasing the pressure in plenum F2 to the level of the surface pressure. Thus, only a small amount of bleed is allowed to flow through the 20° bleed holes in F2. Since choked bleed holes were assumed in all bleed plenums for the analytical design, the predicted bleed rates are higher than the experimental bleed rates for such cases.

Figures 28 and 29 present a comparison of measured and predicted bleed rates and surface static pressures for the two forward bleed ducts D1 and D2 in the centerbody bleed system. The data are shown versus centerbody position rather than Mach number to facilitate correlation with the centerbody bleed schedule (fig. 4). The Mach number corresponding to

a given centerbody position can also be obtained from figure 4. It is evident from figures 28 and 29 that the surface pressures for the individual bleed plenums in general are well predicted.

The largest discrepancy occurs for plenum T7 because the third shock interaction has moved forward of the inviscid shock (see fig. 27) influencing the pressure on T7. The bleed rates are generally lower than predicted by 10% to 20%. As mentioned before, choking in the bleed ducting with resultant bleed hole unchoking causes larger deviations in a few cases.

The bleed rates presented in this section were measured with the main duct plug valve wide open (i.e., with the normal shock far downstream in the subsonic diffuser) to avoid any influence of the terminal shock on the forward bleed rates. During inlet performance runs, when the normal shock is positioned near the throat, the forward centerbody bleed rates were found to increase slightly from the open plug values even though the surface pressures across the bleed regions remained unchanged. This indicates that a leakage path existed between the primary duct and the centerbody support tube. For the open plug runs, the pressure differential between these ducts is very small, while the primary duct pressure is much higher than the support tube duct pressures for the performance runs. Consequently, the indicated centerbody bleed rates for the performance runs are higher than the actual bleed rates. The estimated total error is about 0.007 W_L at Mach 3.5 decreasing to 0.002 W_L at Mach 2.6. No change in bleed rates was found below Mach 2.6.

The errors could be calculated only for the runs in which data were recorded with the normal shock located both far downstream in the diffuser and forward in the throat region. For most of the performance runs, data were recorded with the normal shock in the throat region only, preventing verification of an error in the bleed flow rate. Consequently, it was decided to ignore the error whenever total bleed rates are later discussed in the "Started Inlet Performance" section. This is considered justifiable since the error is only about 5% of the total bleed rate in the worst case (M = 3.5). The total bleed rates presented in this report are, therefore, slightly higher than the actual bleed rates. However, when detailed studies of the individual forward centerbody bleed regions are described, the flow rates have been adjusted based on the estimated errors.

SUPERSONIC DIFFUSER EFFICIENCY

The inlet is designed to maintain a nominal throat Mach number of 1.25. As the freestream Mach number is decreased, the centerbody must translate forward to meet this requirement. A theoretical translation schedule was established during the analytical design of the inlet, and all predictions were made using this schedule. The centerbody schedule was derived simply by using the throat Mach numbers from the inviscid method-of-characteristic program and by assuming that the decrease in throat flow rate due to removal of bleed flow in the supersonic diffuser just compensates for the reduction in throat area due to boundary-layer blockage. This rule of thumb was quite accurate when applied to lower cruise Mach number inlets (refs. 3 and 4). Consequently, for the present inlet the theoretical centerbody schedule was used as a baseline with which to judge the supersonic diffuser performance as will be seen.

The experimental centerbody translation schedule for operation with a throat Mach number of 1.25 was established by first defining the critical centerbody positions at each Mach number and then adding 0.05 Mach number to the critical schedule. For example, if the inlet unstarts at $\Delta X/R_L = 0.90$ at Mach 2.25, then the throat Mach number will be about 1.25 at Mach 2.30 and $\Delta X/R_L = 0.90$, because

$$\frac{(A/A_*)_{M=2.30}}{(A/A_*)_{M=2.25}} = \frac{2.193}{2.096} = 1.047 = (A/A_*)_{M=1.25}$$

It is assumed here that the inlet throat flow rate and throat recovery remain unchanged while increasing the freestream Mach number from 2.25 to 2.30. In addition, it is assumed that the inlet unstart at the critical $\Delta X/R_L$ occurs as a result of inlet choking ($M_{TH} = 1.0$) rather than because of a sudden boundary-layer separation that can reduce the effective throat area.

The theoretical and experimental translation schedules for bleed configuration 1 are shown in figure 30. The agreement is good except between Mach 2.8 and 3.2 where the centerbody is further out than expected, indicating some problems in the supersonic diffuser. As previously discussed in the "Analytical Inlet Design" section, boundary-layer separation was predicted at the second centerbody shock reflection in this Mach number range. Centerbody boundary-layer rakes 4 and 5 also showed high H_i values just downstream of the second shock reflection followed by rapid redevelopment. It appears that the second shock is indeed inducing separation causing premature inlet unstart as the centerbody is retracted.

To improve this situation, additional bleed holes in plenums T1 and T2 were opened. The centerbody translation schedule for this configuration (conf. 3) is also shown in figure 30. The experimental curve is now very close to the predicted schedule, indicating that the above problem has been alleviated.

Further, with a well controlled boundary layer, the strengths of the oblique shocks should be close to the theoretical inviscid strengths and the total-pressure losses in the supersonic diffuser then should be close to the predicted losses. This hypothesis can be verified by using the following expression for continuity:

$$\frac{W_{TH}}{W_L} = \left(\frac{P_T}{P_{To}}\right)_{TH} \left(\frac{A_{EFF}}{A_L}\right)_{TH} \frac{(A/A_*)_\infty}{(A/A_*)_{TH}}$$

or

$$\left(\frac{P_T}{P_{To}}\right)_{TH} = \frac{W_{TH}/W_L}{(A_{EFF}/A_L)_{TH}} \frac{(A/A_*)_{TH}}{(A/A_*)_\infty}$$

where

$$W_{TH}/W_L = W_C/W_L - (W_{BLEED}/W_L)_{SUPERSONIC\ DIFFUSER}$$

and

$$\left(A_{EFF}/A_L\right)_{TH} = A_{TH}/A_L - A_{BLOCK}/A_L = A_{TH}/A_L \left(1 - \frac{A_{BLOCK}}{A_{TH}}\right)$$

The throat total-pressure recovery can thus be computed if the throat blockage as well as the throat Mach number or $(A/A_*)_{TH}$ are known. Since the measured boundary-layer properties are close to the predicted values as shown in the preceding sections, it is reasonable to use the predicted throat blockage. The throat Mach numbers can be determined fairly accurately by an examination of the static pressures on the cowl and centerbody in the throat region with the normal shock at a supercritical position. Figure 31 shows the results of the study that was conducted for configuration 3. The throat total-pressure recovery agrees well with the predicted recovery, indicating that the actual oblique shock losses are close to the theoretical inviscid shock losses. Note from the above equations that an increase in the throat blockage (i.e., reduction in effective throat area) requires an increase in total pressure to pass the same mass-flow through the throat at the same throat Mach number. Therefore figure 31 also confirms that the experimental boundary-layer blockage cannot be much greater than predicted, since the throat total pressure is already 98% to 99% of the freestream total pressure.

CONSIDERATIONS FOR FUTURE DESIGN WORK

It has been shown that a high performance supersonic diffuser was achieved using the analytical procedures described in reference 1. The oblique shock system and surface static pressures are predicted accurately enough throughout the Mach number range, and the bleed plenums are positioned close enough to adequately control the boundary layer through the shocks and adverse pressure gradients. Although the bleed rates generally are lower than predicted, the actual boundary-layer properties are close to the predicted properties. The test results showed, however, that several areas within the analytical procedures can be improved to provide a more complete and accurate design. The most noticeable of these were bleed hole flow coefficients, surface roughness from inactive bleed holes, and boundary-layer transition and redevelopment. Special tests were conducted to explore these areas; the results are summarized following.

BLEED HOLE FLOW COEFFICIENTS

The individual bleed areas were sized to provide the desired amount of bleed using the empirical bleed hole flow coefficients (fig. 1 of ref. 1). The bleed exits were then sized to provide the maximum bleed plenum pressure without unchoking the bleed holes. As discussed previously, the experimental bleed rates are generally lower than predicted, indicating either premature unchoking of the holes (i.e., lower maximum allowable plenum pressure) or lower than expected maximum flow coefficient.

This problem was investigated in a separate study using cowl plenum 1. Only rows 5 and 6 were open to enable an accurate measurement of the average surface static pressure across the bleed region. Data were recorded at various Mach numbers and centerbody positions to obtain a large variation in surface conditions at the bleed region. This testing was repeated with different bleed exit settings to vary the bleed plenum pressure. The results are

presented in figure 32. The bleed rates have been converted to flow coefficients Q to obtain a direct comparison with the empirical data used in the bleed system design.

The test results again fall below the design curves (ref. 1). Along the design operating line, which was used for sizing the bleed exits, the actual flow coefficient is 12% less than the predicted value at Mach 1.4. The discrepancy increases to 22% at Mach 1.8. Note from figure 32 that the discrepancy decreases at lower plenum pressures, indicating that premature bleed hole unchoking is in part responsible for the lower bleed rates. For future bleed hole sizing, the curves shown in reference 1 for 20° bleed holes should be modified to reflect the present findings.

BLEED HOLE ROUGHNESS

Since the individual centerbody bleed plenums are active (i.e., transferring bleed) only within a limited range of centerbody translations, a large number of bleed holes are always inactive. These inactive holes create surface roughness that affects the boundary-layer development. At the high Mach numbers the inactive holes are located downstream of the throat, thus influencing the performance of the subsonic diffuser. As the freestream Mach number is reduced, more and more plenums become inactive in the forward part of the supersonic diffuser. This roughness was not accounted for in the boundary-layer calculations. One of the objectives of this experimental program was, therefore, to determine the significance of surface roughness created by the inactive bleed holes in the supersonic diffuser.

The roughness effect was evaluated by closing the bleed holes in plenums F1 and F2 to obtain a smooth surface. These bleed regions consist of relatively large bleed holes (see table 2) and, since they are inactive, are the largest contributors to surface roughness below Mach 2.6. Typical results of this study are shown in figure 33. Here plenums F2 and F3 are located downstream of the first shock reflection in a region of constant static pressure. Comparison of H_i values in the table show that the difference noted previously between the predicted and measured H_i values is evidently a direct result of the surface roughness from the inactive holes.

The overall inlet performance was also evaluated without the roughness from plenums F1 and F2. The critical recovery increased by a small amount (by about 0.003 P_{T_0} at M = 2.3 and by 0.01 P_{T_0} at M = 1.7) indicating that the roughness effect is felt even downstream of the forward bleed (see fig. 4). However, the relatively small performance improvements also indicate that the subsonic diffuser separations, which occur at most of the off-design Mach numbers (see the "Started Inlet Performance" section), are not a result of the surface roughness. It is thus concluded that inactive holes in the supersonic diffuser increase the boundary-layer profile distortion by a small amount resulting in a relatively small performance penalty. A small amount of forward bleed could be added to compensate for this effect.

BOUNDARY-LAYER TRANSITION AND REDEVELOPMENT

As discussed earlier, the bleed system was basically designed by first computing the boundary-layer development without bleed up to the point of separation. Bleed was then

located upstream of the separation, and the bleed rates were increased until separation was no longer indicated and acceptable boundary-layer characteristics were achieved. A typical example of this is seen on the cowl H_i maps without and with bleed in figures 5 and 7, respectively. Note that the first cowl shock reflection separates above Mach 2.9 without bleed. The analysis showed that bleed was needed close to the reflection at Mach 3.5 to provide adequate control at this Mach number. Bleed plenum 1, therefore, was positioned from station 4.2 to 4.35 as shown in figure 7. Since the first cowl shock moves ahead of this location at about Mach 3.1, some bleed was required upstream of plenum 1 to prevent boundary-layer separation between Mach 2.9 and 3.1. The boundary-layer analysis indicated that this could be accomplished with only a very small amount of bleed (about 0.0025 W_L). Two rows of 0.66-mm holes (plenum 0), therefore, were located as shown in figure 7 and table 2.

One of the test objectives was to determine if this bleed plenum can be eliminated without adversely affecting the inlet performance or if the first cowl shock reflection indeed separates between Mach 2.9 and 3.1 without upstream bleed. The inlet, therefore, was tested in this Mach number range with and without bleed from cowl plenum 0. Figure 34 shows the static-pressure distribution in the area of the shock reflection. There is no evidence of any change in the distributions that would indicate a change in shock structure.

A cowl boundary-layer rake was located at station 4.11; i.e., just upstream of the shock at Mach 3.1 and downstream at Mach 2.9. Since the static-pressure rise across the shock is nearly constant in this Mach range, it is assumed that the rake data can be treated as if the rake were translated through the shock reflection at Mach 3.0. Figure 35 shows the boundary-layer development and local Mach number change across the shock with and without the upstream bleed. The displacement thickness increases by about 25%, while the shape factor is only slightly higher when the bleed is shut off. The predicted boundary-layer development (with bleed) indicates a high H_i value ($\sim$1.4) upstream of the shock resulting in both a highly distorted profile (H_i, $\sim$ 1.9) downstream of the shock and an increase in displacement thickness. The data show a much lower H_i ($\sim$1.28) upstream of the shock and a smaller increase in H_i across the shock, as well as a slight reduction in δ^* even without bleed. It is concluded that plenum 0 can be eliminated without adversely affecting the inlet performance as long as the downstream bleed (plenum 1) is increased to compensate for the slightly thicker boundary layer.

It was shown previously in the "Boundary-Layer Development" section that the transition on both the cowl and the centerbody possibly occurred further downstream than predicted. This would explain the conservative δ^* predictions. However, the predicted H_i is also conservative in this region of the inlet and does not change significantly with the point of transition (compare figs. 15 and 16). The problem appears to be in the redevelopment region downstream of the transition. In this region, the boundary layer sees a slight adverse pressure gradient (ref. 1. fig. 5) that counteracts the natural redevelopment of the turbulent boundary layer. The effect of the adverse gradient is apparently overpredicted resulting in prediction of overly distorted boundary-layer profiles in the upstream portion of the supersonic diffuser. The present test results can be used to refine the redevelopment calculations in the boundary-layer program.

STARTED INLET PERFORMANCE

The performance of the inlet at the design point and at lower speeds in the started Mach number range is described following. Various configuration changes were made to identify the significant parameters governing the inlet behavior, to determine the accuracy of analytical predictions, and to upgrade performance. All geometry parameters for the inlet configurations considered in this section are listed in table 4. The reader may find it helpful to refer to the table during the course of the discussion. Note that whenever bleed hole changes were made, rows were opened or closed in pairs to maintain circumferentially uniform bleed.

Frequent references will be made to the critical and operating conditions. The critical point is defined as the minimum stable engine-face corrected flow just before the normal shock is expelled from the inlet, while the operating point is defined as the corrected flow 5% above the critical value (5% stability margin, or 5% supercritical).

DESIGN POINT PERFORMANCE

Engine-face recovery and distortion characteristics, and total bleed flow rates are shown in figure 36 for four bleed geometries. Configuration 1 is the primary bleed system designed using the analytical procedure. Configuration 16 has cowl plenum 0 closed and increased bleed area in cowl plenum 2. The exit areas are at high settings to choke the bleed holes. Configuration 21 has cowl plenum 0 reopened, and all exits reduced to increase the bleed plenum pressures. (Conf. 3 is of interest primarily during off-design operation and is shown in fig. 36 for reference only.)

The highest critical recovery, ($0.858\ P_{T_O}$), was recorded with configuration 21, while the highest operating recovery, ($0.837\ P_{T_O}$), was obtained with configuration 16. The performance improvements over configuration 1 are due to the increased bleed in cowl plenum 2 and the installation of vortex generators on the centerbody. The bleed is higher for configuration 16 than for configuration 1 as a result of the increased number of holes open in plenum 2 and the increased throat bleed due to the normal shock being further forward. For configuration 21 the bleed exit areas were reduced. Consequently, the throat bleed does not increase as much when the normal shock moves forward, and the total bleed is close to that of configuration 1. Table 5 lists the respective forward bleed flow rates. The experimental values are shown for $\Delta X/R_L = 0$ to allow comparison with design predictions.

In configuration 1 the bleed in cowl plenum 2 was considerably lower than predicted. Two additional rows of holes were opened in configuration 16 to increase the bleed to the predicted value. With the bleed rate in cowl plenum 2 closer to predictions, the performance improved as seen in figure 36. Table 5 also indicates that in configuration 21, with the exits reduced, the holes in centerbody plenums F1 and F2 were unchoked, while the cowl bleed holes were essentially unaffected. The bleed exit areas in configuration 21 are close to the values predicted in table 4 of reference 1 for maintaining choked flow through the bleed holes. The increased critical recovery (see fig. 36) is probably due to the presence of the centerbody vortex generators.

Static and total-pressure profiles in the throat region at the critical point are presented in figure 37 for configuration 21. The normal shock boundary-layer interaction is well controlled as indicated by the distinct pressure rise and the attached boundary-layer profiles downstream. The indicated recovery in the core flow is approximately 0.94 P_{T_0}. The pitot profiles for configurations 1 and 16 are compared with configuration 21 in figure 38. The upper plots show that the boundary-layer profile has improved on the cowl because of increasing the bleed in cowl plenum 2, and deteriorated on the centerbody because of reducing the bleed exit areas in configuration 21. The compressor face-rake profiles in figure 39 indicate that the latter effect was canceled by the centerbody vortex generators since configuration 21 has higher pressures than configuration 1 across the engine face at the critical point. The lower plots in figure 38 indicate a slight improvement in the cowl boundary layer for configuration 21. This is probably caused by opening cowl plenum 0 since all cowl rakes, including 1, 2, and 3, show fuller profiles. The effects of the reduced bleed exit areas for configuration 21 are again apparent, since the boundary-layer profiles on the centerbody have deteriorated compared to configuration 16. Compressor face total-pressure profiles are shown in figure 39. At the critical point, all three cases indicate higher recovery near the cowl than near the centerbody. At the operating point, the patterns are reversed with the higher recovery concentrated near the centerbody. The effect may be caused by the smaller reduction in throat bleed on the centerbody than on the cowl as the normal shock moves downstream, causing the flow to attach to the centerbody.

Individual bleed flow rates and plenum pressures for configurations 1 and 21 are compared in table 6. The bleed exit areas in configuration 1 are set to maintain choked flow through the bleed holes throughout the started Mach number range of inlet operation. The exit areas were reduced to the requirements of operation at Mach 3.5 in configuration 21 (discussed in ref. 1, p. 24). The change is reflected in table 6 by the higher bleed plenum pressures for configuration 21. As noted previously, the centerbody bleed holes were unchoked in this configuration. As a result of the unchoking of the centerbody bleed holes, the total bleed is less for configuration 21 than for configuration 1, even though the former has more total bleed hole area open (see table 4).

A series of configurations was tested to evaluate the accuracy of predicting bleed requirements with the analytical design procedure. The experimental approach involved observing the changes in the inlet performance resulting from changes in the quantity and distribution of forward bleed in the supersonic diffuser, using the design bleed system (conf. 1) as the baseline. Generally, the inlet performance will be poor if the centerbody cannot be retracted to the design position without unstarting the inlet or if the boundary-layer profile at the throat is highly distorted. Thus, the critical centerbody position quickly indicates problems in the supersonic diffuser and the boundary-layer shape factor identifies problems with the boundary layer.

The results of the study are summarized in figure 40. The throat bleed is not considered since only the forward bleed requirements were predicted by the analytical procedures. The data shown in figure 40 were obtained at $\Delta X/R_L = 0$ to allow comparison with theory. The following comments refer to these profiles.

Cowl plenum 1—The analytical design required 0.016 W_L bleed and four rows open in this plenum. Two of the four rows were closed in cowl plenum 1 after the bleed had been reduced in centerbody plenum F2. Data are not shown for this configuration since the inlet unstarted before the centerbody could be retracted to $\Delta X/R_L = 0$. The cowl holes were reopened in configuration 16 after F2 had been restored. The maximum recovery for configuration 16 was 0.014 P_{T_O} higher than for configuration 15. The conclusion may be made that when the inlet performance was otherwise good, reducing the bleed in plenum 1 by 50% resulted in a loss 0.014 P_{T_O} critical recovery.

Cowl plenum 2—The analytical design required 0.031 W_L bleed and four open rows. As noted previously, with four rows open the bleed flow rate was only 0.019 W_L. When the two remaining rows were opened, the bleed increased to 0.025 W_L. Figure 40 shows that a relatively minor improvement was obtained in the boundary-layer profile shape downstream of plenum 2; however, this was accompanied by 0.035 P_{T_O} increase in critical recovery. The plot also shows that the profile improved further when cowl plenum 1 was reopened in configuration 16. The initial improvement due to plenum 2 would have been less if plenum 1 had been at the high setting all along. These results illustrate the importance of considering the interaction of the various bleed regions in the design process.

Centerbody plenum F1—The analytical design required 0.010 W_L bleed and two rows open. This plenum was closed only for one configuration. The boundary-layer shape factor increased from 1.34 to 1.51 downstream of the plenum when the holes were closed, and the critical recovery decreased by 0.066 P_{T_O}. The drastic loss of recovery is convincing proof that bleed is required at this location. In configuration 18, the holes were reopened and the exit areas were reduced, thereby reducing the bleed to 0.007 W_L. This bleed rate in plenum F1 was sufficient to keep the shape factor just downstream of the plenum below the predicted value.

Centerbody plenum F2—The analytical design required 0.030 W_L bleed and four rows open. Closing of two rows in this plenum did not appear to have a significant influence on critical recovery. The shape factor just downstream of the plenum increased from 1.28 to 1.34, and the critical centerbody position increased from less than $\Delta X/R_L = -0.055$ (maximum retraction) to -0.038. After the bleed in cowl plenum 1 had been reduced, the holes in F2 were reopened in configuration 14. The latter change resulted in reducing the critical centerbody position from $\Delta X/R_L = +0.016$ to less than -0.055 and an increase in recovery of 0.011 P_{T_O}. Thus, it is seen that the effects of bleed are felt not only in the local boundary layer but can be propagated to the opposite surface, mainly via the shock structure. This again points out the importance of considering the interactions of bleed regions on the opposite surface as well as on the same surface.

These results show that in order to achieve good inlet performance the boundary layer must be controlled by bleeding the right amounts in the proper places. In general, decreasing the bleed below the design requirements in the forward plenums resulted in significant losses of recovery.

While numerous bleed configurations were tested, the best on-design performance only slightly exceeded that obtained with the predicted configuration (conf. 1). Furthermore, the improvements were achieved primarily by adjusting the bleed rates closer to the analytical predictions. (As has been noted, the bleed rates were lower than predicted for configuration 1.) These observations lead to the conclusion that the bleed rates were well predicted, enhancing the validity of the analytical procedure.

A minimum bleed configuration was presented in table 5 of reference 1. Using configuration 1 as the baseline, cowl plenum 0 was to be eliminated, and two rows of holes were to be plugged in each of cowl plenums 1, 2, and 3, and centerbody plenum F2. The associated discussion suggested this to be a hypothetical configuration to be attempted through a step-by-step reduction of bleed to explore the minimum possible bleed at Mach 3.5. The process was tried experimentally in configurations 10 through 13. The bleed reductions were implemented in each plenum, except cowl plenum 3. At this point the inlet unstarted at a centerbody position of $\Delta X/R_L = 0.016$ which corresponds to an effective throat area approximately 10% less than the predicted value, indicating flow separation at or upstream of the throat.

Inlet static-pressure distributions and boundary-layer pitot-pressure profiles downstream of the normal shock are shown in figure 41 for the last two configurations in the above series along with similar data for configuration 21. In configurations 12 and 13, the normal shock pressure rise appears to be spread out as opposed to the distinct shock in configuration 21. Also in configurations 12 and 13, both the cowl and centerbody profiles contain inflection points suggesting incipient separation. These last two were the only configurations tested that did not allow the centerbody to be retracted to the design position ($\Delta X/R_L = 0$) without unstarting the inlet.

OFF-DESIGN PERFORMANCE

A summary of critical engine-face performance and bleed rates at critical conditions between Mach 1.6 and 3.5 are presented in figures 42 and 43. As described previously, configuration 1 is the predicted bleed configuration while configuration 3 has additional bleed holes open in plenums T1 and T2 to improve the centerbody boundary-layer control at off-design Mach numbers.

The performance obtained with configuration 1 is high near the design Mach number but drops off sharply below Mach 3.3. The recovery increases linearly from Mach 3.1 to 2.5 until a 0.05 P_{T_0} increase in recovery occurs between Mach 2.5 and 2.4. Below Mach 2.4, the recovery again increases linearly reaching a value of 0.925 P_{T_0} at Mach 1.6.

In configuration 3 additional bleed holes (table 2, rows 14, 15, 18, and 19) were opened in plenums T1 and T2. This increases the forward centerbody bleed between Mach 2.3 and 3.3 and the throat bleed between Mach 3.3 and 3.5 (see fig. 4). Figure 42 indicates that considerable improvement in performance is obtained with configuration 3 in the Mach range from 2.3 to 3.3. The increases in the forward bleed rates are tabulated in table 7 for the individual Mach numbers in the 2.3 to 3.3 range. Also shown are the predicted bleed rates that were used for the boundary-layer analysis during the bleed system design.

It was previously shown in the "Bleed System Performance" section that the actual bleed hole flow coefficients were slightly lower than expected resulting in measured bleed rates lower than predicted. Configuration 3 merely increases the forward bleed rates on the centerbody to the predicted values in the 2.3 to 3.3 Mach number range.

The effect of the increased centerbody bleed on the boundary-layer control is demonstrated in figure 44. The centerbody static-pressure profiles upstream of the throat for configurations 1 and 3 are compared with the theoretical inviscid profile. The M = 3.1 case was chosen because it exhibits the lowest engine-face recovery (see fig. 42). The static-pressure profiles show that in configuration 1 the pressure rise across the second centerbody shock is only about half of the inviscid pressure rise, indicating boundary-layer separation. Boundary-layer rakes 4 and 5 are located near the shock interaction. The distorted profile on rake 4 confirms that the boundary layer is close to separation in the upstream portion of the shock/boundary-layer interaction. Reattachment occurs downstream of the shock (probably due to the bleed in plenum T2), but the profile shape is still distorted on rake 5.

In configuration 3, the static-pressure ratio across the shock is closer to the predicted value, but the gradual pressure rise indicates that separation still is present in the interaction region. The profile on rake 5 shows, however, that a rapid redevelopment has occurred downstream of the shock such that the boundary layer at the throat should be able to better withstand the normal shock pressure rise. Referring to the "Analytical Inlet Design" section, boundary-layer separation with rapid reattachment was predicted for this shock interaction in the Mach 2.4 to 3.3 range. This is evidently correct when the forward bleed rates are reasonably close to the predicted values, as is the case with configuration 3.

Even though the boundary-layer profile just upstream of the throat now appears to meet the design goal of $H_i \approx 1.28$ (see ref. 1), the inlet recovery still drops off below Mach 3.3 (see fig. 42). The data for configuration 3 seem to follow a common trend between Mach 1.6 and 3.1, suggesting that the flow phenomenon responsible for the excessive losses also is common.

The data for configuration 3 were analyzed to estimate the magnitude of the losses attributable to the various loss mechanisms in the inlet. The results of the analysis are illustrated in figure 45. The oblique shock losses were previously estimated under the "Supersonic Diffuser Efficiency" section, where it was concluded that the supersonic diffuser performance was high and in close agreement with predictions throughout the started Mach range. The normal shock total-pressure losses are based on the experimental throat Mach numbers shown in figure 31 for configuration 3. The combined oblique and normal shock losses check with the maximum pitot-pressure measurements from the cowl

throat boundary-layer rakes. (Note that the centerbody rakes translate forward of the throat during off-design operation, and only cowl rakes 3 and 4 provide a valid measure of the throat pitot pressure.) The total-pressure loss in the throat boundary layers just downstream of the normal shock could be measured at Mach 3.5, since the aft centerbody rakes are downstream of the throat. Figure 46 shows the throat static and total-pressure profiles at the critical condition for configuration 3. A mass averaged integration of the aft total-pressure profile indicates that the losses in the boundary layer are equivalent to a total-pressure deficiency of 0.044 P_{T_O} across the profile. Figure 31 shows that the throat boundary-layer blockage upstream of the normal shock varies only a small amount with freestream Mach number. It was also shown that the throat Mach numbers are nearly the same at all test conditions. Therefore, it is reasonable to assume that the boundary-layer total-pressure loss just downstream of the normal shock is nearly constant. The blockage losses shown in figure 45 for the off-design Mach numbers were computed by assuming the loss to be proportional to the upstream blockage rate using the ratio determined at Mach 3.5.

Subtracting the engine-face recovery from the recovery derived from the cumulative losses yields the subsonic diffuser losses. Figure 45 shows that the recovery at the subsonic diffuser entry ranges bewteen 0.91 and 0.95 P_{T_O}. Above Mach 1.9, between 0.08 and 0.15 P_{T_O} of this recovery is lost in the subsonic diffuser, meaning that over one-half of the total-pressure losses up to the engine face occur in the subsonic diffuser.

Compressor face total-pressure profiles are shown in figure 47. At all Mach numbers below 3.5, the total pressure of the flow near the centerbody is consistently lower than the total pressure of the flow near the cowl, indicating separation on the centerbody. Figures 48 and 49 show the inlet static-pressure distributions at two Mach numbers, 3.5 and 2.7, respectively. The ideal inviscid pressure distribution curves superimposed on the figures were calculated from the geometric area variations assuming a normal shock throat Mach number of 1.3 and 0.92 P_{T_O} recovery downstream of the shock. Figure 48 indicates that at Mach 3.5, good diffusion is obtained initially downstream of the normal shock. The data begin to deviate from the ideal curve near station 4.9, probably caused by a rapid increase in boundary-layer displacement thickness. Near station 5.7 the static pressure becomes essentially constant, suggesting flow separation. Approximately 25% of the diffuser entry dynamic pressure (q) is lost in mixing, yielding an overall recovery of 0.848 P_{T_O} at the engine face.

At Mach 2.7, figure 49 shows the cowl static-pressure distributions that are typical of the off-design conditions, exhibiting significant total-pressure loss near the centerbody at the engine face. The plot indicates separation immediately following the normal shock. The total-pressure loss in the diffuser is calculated to be approximately 40% of the initial dynamic pressure. To help visualize the subsonic diffuser separation problem, a computation was made to determine the reduction in effective flow area as a result of the separation. The results are shown in figure 50 together with the assumed recovery distribution. This distribution was derived by using an entrance recovery of 0.92 P_{T_O} downstream of the $M = 1.3$ normal shock, and an exit recovery equal to the compressor face recovery from figure 42. The high recovery in the upstream part of the diffuser is a result of the requirement of keeping the computed effective flow area equal to or smaller than the geometric area. The remainder of the curve was faired somewhat arbitrarily using estimated

mixing losses. The computed area curve is converted into inlet contours in figure 51. The extent of the separation agrees well with the total-pressure profile measured at the compressor face (fig. 47).

The foregoing evidence has shown that large diffuser separations originating at or near the normal shock are present at off-design Mach numbers, explaining the low recoveries at these conditions. It also explains the trend of increasing recovery with decreasing Mach number (fig. 42), since less and less diffusion is required as the throat area is increased for off-design Mach number operation. As discussed earlier, this extreme separation phenomenon does not take place near the design Mach number, probably because the initial rate of change of diffuser area is more gradual when the centerbody is retracted to the M = 3.5 position (see fig. 52). The solution to the off-design performance problem appears to be a redesign of the subsonic diffuser to improve the area distribution for extended centerbody positions, possibly combined with a redesign of the centerbody throat bleed system to improve the control of the normal shock/boundary-layer interactions. It should be noted, however, that it is not possible to significantly improve the initial diffuser area distributions without also reducing the transonic airflow capacity of the present inlet.

PERFORMANCE AT ANGLE OF ATTACK

The operating point of the supersonic diffuser is defined as the centerbody position, where the diffuser will tolerate a 0.05 freestream Mach number reduction without unstarting. At zero angle of attack, the operating point corresponds to a throat Mach number of approximately 1.25. If the flow enters the inlet at some angle of incidence, the centerbody must be translated forward to increase the throat area to accommodate the increased compression on the windward side and still maintain the 0.05 Mach tolerance. (In flight an inlet angle-of-attack sensor would be required to bias the centerbody position servosystem.)

Operating centerbody positions for various angles of attack for configuration 3 are plotted in figure 53. The agreement is good between the design schedule and the experimentally determined schedule at zero angle of attack as discussed previously for figure 30. (Centerbody positions were not predicted for the nonzero incidence cases, since the analytical program can calculate only axisymmetric and two-dimensional flow fields.) In general, the centerbody schedules at angle of attack have the same slope as the zero angle schedule, implying that the supersonic diffuser flow field is well controlled by the bleed system during angle-of-attack operation. Above Mach 3.1, the schedules at 3° and 5° deviate from the normal trends. At these conditions performance data were difficult to obtain.

Below Mach 2.5, inlet unstarts at 5° angle of attack could not be identified with the wind tunnel Schlieren system; therefore, 5° operating points are not shown for this Mach range.

Inlet performance at 0°, 1.5°, and at 3° angle of attack is shown in figure 54. The corresponding individual bleed flow rates and plenum pressures are presented in table 8. Between Mach 2.1 and 3.1, the effect of angle of attack on the performance is nearly constant. The critical recovery decreases by about 0.10 P_{T_O} when the inlet is pitched to 3°α. This large drop in inlet recovery is due primarily to the increase in average throat Mach number as will be seen.

Referring to figure 53, the operating centerbody positions for 3°α are displaced relative to the 0° positions by about $\Delta X/R_L = 0.10$ along the ordinate or by about Mach 0.16 along the abscissa. If, therefore, the inlet were tested at 0° with the centerbody located on the 3° operating line, the Mach tolerance would be $\Delta M = 0.21$. This corresponds to a throat Mach number of about 1.52 compared to about 1.25 on the 0° operating line. The increase in loss from the M = 1.25 normal shock to the M = 1.52 normal shock is 0.064 of the upstream total pressure. Since the amount of flow captured by the inlet is nearly constant when pitching from 0° to 3°α (as indicated by flow measurements), the average throat Mach number also remains unchanged with the throat Mach number decreasing on the leeward side and increasing on the windward side of the inlet. Assuming that the total-pressure loss across the critical normal shock in the nonuniform throat flow is at least as high as that across a uniform M = 1.52 normal shock, more than two-thirds of the drop in engine-face recovery (fig. 54) from 0° to 3°α can be explained simply by the increase in average throat Mach number.

Note in figure 54 that, compared to the 0° performance, the angle-of-attack performance further deteriorates above Mach 3.1. This problem is believed to be associated with an inadequacy in the centerbody bleed system to control the second centerbody shock reflection. Figure 4 illustrates that when the centerbody is retracted toward $\Delta X/R_L = 0$, plenum T2 shuts off to duct D1, and plenum F1 opens up at $\Delta X/R_L = 0.3$. Thus, only the forward bleed provided by plenums F2 and T1 is available at this particular position. Referring to figure 8, note that flow separation was predicted downstream of the second centerbody shock reflection in the neighborhood of $\Delta X/R_L = 0.3$. It was shown previously that the predicted separation was controlled by the bleed system, and the flow was attached downstream of the shock at zero angle of attack. When the inlet is pitched, the shock system moves forward and increases in strength on the leeward side of the inlet. It is believed that the strengthening of the oblique shock waves combined with the sudden reduction in centerbody bleed at $\Delta X/R_L = 0.3$ was the basic reason for the poor performance at angle of attack above Mach 3.1. It is also believed that the high Mach number angle-of-attack performance could be improved by an alteration of the support tube slot so as to slightly overlap the bleed in plenums F1 and T2.

An important characteristic of the inlet for control purposes is the operating angle-of-attack tolerance (that is, the maximum excursion from zero incidence where the inlet will remain started without any change in inlet geometry). The operating angle-of-attack tolerance was approximately 1° between Mach 3.5 and 2.5. The tolerance increased with decreasing Mach number to approximately 2.5° at Mach 1.6. Therefore, in a flight inlet the control system would need to be activated to translate the centerbody whenever the inlet angle of attack exceeded the above values.

VORTEX GENERATORS

Vortex generators were installed in the subsonic diffuser in an attempt to improve the inlet performance. The centerbody vortex generators shown in figure 2 increased the engine-face recovery by about 0.01 P_{T_O}. None of the generator patterns tested improved the off-design performance.

The effects on performance of three centerbody vortex generator patterns are compared in figure 55. Engine-face recovery, distortion, and total boundary-layer bleed are plotted as a function of supercritical margin. The supercritical margin is defined as the percentage increase in engine-face corrected flow from the minimum stable value. The generators used in configurations 4, 5, and 9 were triangular flat plates with the height and base dimensions shown in figure 55. They were installed at 20° to the flow direction in diverging pairs at the stations noted. The spacing of 2 to 1 indicates that the mean distance between two pairs was twice the mean distance between the two generators in one pair; this pattern required 24 pairs of generators.

Configuration 4 with the 1- by 2-cm generators at station 4.96 (approximately 0.25 R_L downstream of the throat) had the most beneficial effect on performance compared to the configuration without generators (conf. 3). The recovery increased 0.007 P_{T_O} at the critical point and 0.012 P_{T_O} at 5% supercritical margin. The distortion decreased by about 2%. When the same pattern was moved aft to station 5.11 (conf. 5), the generators became less effective probably as a result of a thicker boundary layer. Compared to configuration 3, the improvement in critical recovery was 0.005 P_{T_O}. Vortex generators were also installed at station 5.41 (conf. 9). This far aft of the throat the boundary layer was apparently so thick that even though the generators were larger (1.25- by 2.5-cm) they did not significantly affect the recovery. The vortex generators at the forward locations increased mixing and improved diffusion, while at the aft location they were too deeply immersed in the boundary layer to be effective.

The performance effects of rectangular and triangular centerbody vortex generators are compared in figure 56. Both configurations were tested with reduced bleed. The inlet recovery is higher with the triangular generators. However, it is not clear whether this is caused by the difference in the shape or in the height of the generators. Vortex generators were also installed on the cowl in various patterns. None of the tested configurations produced an improvement in performance.

Detailed study of the vortex generator data revealed that configurations 4 and 5 (fig. 55), which had the highest recovery, also had the critical normal shock further forward in the throat. This finding suggested additional investigation of the relationship of normal shock position and vortex generator geometry. The results are illustrated in figure 57. As the engine-face corrected flow decreases, the normal shock moves forward into the throat and pressurizes the throat bleed plenums. For a given bleed geometry, the throat bleed rate indicates the relative position of the normal shock. The configurations shown on the same plot in figure 57 have identical bleed geometries. An increase in recovery at the same bleed rate indicates increased diffuser efficiency, while a higher maximum bleed rate indicates that the normal shock is further forward at the critical point.

Figure 57 shows that compared to the configuration without vortex generators (conf. 3), the improvement obtained by configurations 4 and 5 are due in part to improved diffuser efficiency and in part to improved normal shock position. Configuration 9 did not show a significant change in either of these parameters. The higher recovery of configuration 21 as compared to configuration 22 appears to be due primarily to improved normal shock position. Figure 57 also indicates that when vortex generators were installed on the cowl, the normal shock could not move as far forward in the throat.

In conclusion, the vortex generators affected the inlet recovery by improving the subsonic diffuser efficiency and by allowing the normal shock to move further forward in the throat. The increased diffuser efficiency can be explained by improved diffusion due to increased mixing. However, the effect on the normal shock is probably a dynamic phenomenon and could not be sufficiently explained on the basis of the available data.

As noted earlier, no vortex generator pattern was found that would alleviate the off-design diffuser separation problem. Further, a comparison of critical inlet data in figure 58 for configurations 3 and 5 shows that at Mach 2.7, when the generators are located in the throat and interacting with the normal shock, the engine-face performance is reduced.

SUBSONIC DIFFUSER TURBULENCE LEVELS

Two arms of the compressor face rake were provided with three dynamic total-pressure probes each in addition to the steady-state instrumentation. The signals were processed individually to determine the rms average of the local unsteady pressure fluctuations within the bandwidth from 1 to 3000 Hz.

The maximum measured rms values are plotted versus steady-state distortion in figure 59. The data, which represent critical points, indicate that a correlation exists between engine-face rms turbulence and steady-state distortion. Comparing the recovery curve in figure 42 with figure 59, note that at the Mach numbers where high recovery was obtained, the rms values fall below the mean line in figure 59, while at the Mach numbers where the recovery was lower, the rms points are above the line. It appears that the decreased recovery is associated with increased flow turbulence. Two possible sources of the increased turbulence levels could be an increased unsteadiness of the normal shock or increased shear along flow separation boundaries in the subsonic diffuser, both of which would contribute to lower recoveries.

The effectiveness of the vortex generators is related to their ability to induce mixing of the high energy flow into the lower energy regions near the surface (illustrated in fig. 60). The lower plot shows the maximum measured rms values as a function of supercritical margin for four configurations discussed in the previous section. The lowest turbulence levels were obtained with the vortex generators that resulted in the highest recovery (conf. 4), while highest rms peaks were recorded with the other two vortex generator configurations (5 and 9). For the configurations where the vortex generators improved recovery (4 and 5), the rms values uniformly increase toward the centerbody indicating mixing near the surface. For configurations 3 and 9 where the generators had no effect on recovery, the turbulence is more randomly distributed through the profile.

RAMJET SIMULATION

A study was conducted to determine the feasibility of operating the inlet when coupled to a "wrap around" ramjet engine. In this concept a turbojet is contained within an annular ramjet duct. The inlet supplies both engines. At cruise operation, the turbojet is shut off and accepts no airflow. The inlet supply flow is ducted around the turbojet engine face into the ramjet annulus.

The ramjet mode was simulated by blocking off the inner part of the diffuser exit forming an annulus. The area was reduced from 0.744 A_L to 0.324 A_L. Figure 61 compares inlet performance obtained with the diffuser exit open and with the ramjet inserts installed. No significant differences in performance can be observed. With the ramjet inserts, there is a slight loss in recovery at the higher airflows and a slight improvement in distortion at the lower airflows. As expected, the inserts do not influence the flow in the throat, and the bleed rates are unchanged.

The increase in inlet throat area with decreasing Mach number limited testing of the ramjet configuration to Mach numbers above 2.5 (engine-face choking). However, data were recorded only at Mach 3.5 since meaningful performance comparisons could not be made at the lower Mach numbers because of the flow separations in the subsonic diffuser discussed previously.

TRANSONIC INLET PERFORMANCE

UNSTARTED INLET OPERATION

The inlet is designed to operate in the mixed compression mode above Mach 1.6 and in the unstarted (external compression) mode below Mach 1.6. In the unstarted mode, the centerbody is held fixed at $\Delta X/R_L = 1.50$. Only two centerbody bleed plenums, T6 and T7, are active in this position of the centerbody, while all cowl bleed plenums remain open. The inlet flow area distribution for the unstarted mode is shown in figure 62. Note that the throat is located just inside the cowl lip.

To obtain an accurate measurement of the flow entering the inlet (the capture flow), the flow was first calibrated using two 8-probe pitot-pressure rakes installed just downstream of the throat. Each rake had a Prandtl static probe at midspan. The rake pitot pressures and the local cowl, centerbody, and midspan static pressures were used to calculate the capture flow. One of the upstream cowl static pressures was calibrated as a function of mass-flow. Figure 63 shows the calibration curves for each test Mach number. For inlet performance testing, the lip rakes were removed and the capture flow was determined from these calibration curves. The capture mass-flow parameter (C_m) is defined as the ratio of the measured flow to the maximum ideal flow. The latter corresponds to uniform sonic flow through an area equivalent to the geometric throat area with freestream total temperature and total pressure. The maximum point on each curve corresponds to the maximum experimental capture flow at that Mach number.

Figure 64 compares the maximum experimental capture flow with ideal one-dimensional sonic flow at the throat. Between Mach 0.7 and 1.0, the throat blockage (due to boundary-layer growth) and flow nonuniformity cause a loss in flow capacity of about 1% ($<0.005\ W_L$). At Mach 0.6 the maximum capture flow was not obtained since the plug valve could not provide sufficient suction to choke the inlet.

At freestream Mach numbers above 1.0 and at low capture mass-flow ratios, an external normal shock is present upstream of the cowl lip to allow spillage of excess flow around the lip. As the capture mass-flow ratio is increased, the spillage is reduced and the normal shock moves toward the lip. The shock is swallowed when the spillage becomes zero. At this point the throat becomes supersonic, and the capture flow can no longer be increased. Thus above Mach 1.0, the capture flow is limited by starting the inlet rather than by choking the throat. The experimental started mass-flows ($1.1 \geqslant M \geqslant 1.3$) show excellent agreement with predictions.

The transonic performance of the inlet is summarized in figure 65. Engine-face recovery and distortion data are shown versus Mach number at capture mass-flow coefficients of 0.90, 0.95, and 0.98. The decrease in recovery from maximum recovery to the maximum flow is between 0.02 and 0.025 P_{T_O}, except at Mach 0.6. Figures 66 and 67 show the recoveries and distortions versus C_m for each test Mach number. In the range from Mach 0.7 to 0.95, inlet choking occurs at C_m of approximately 0.99 and at a recovery of approximately 0.955 P_{T_O}.

At Mach 0.6 the recovery decreases rapidly starting at $C_m \sim 0.91$. At C_m 0.975, the difference in recovery between Mach 0.7 and 0.6 is 0.03 P_{T_O} (fig. 66), although the inlet is operating with the same throat Mach number (about 0.83). The lower plot (without lip rakes) in figure 68 indicates that for Mach 0.6, the recovery deficiency at the compressor face occurs near the cowl. The upper plot shows the lip rake profiles for similar conditions. Note that the boundary layer appears to be thicker at the lip rake for Mach 0.6. The cowl boundary-layer rake profiles, corresponding to the compressor-face profiles, are shown in figure 69. The M = 0.6 boundary-layer profile progressively thickens, and at rake 4 a separated profile is indicated. At Mach 0.7, the boundary layer remains thin and no separation is indicated. It appears that at high capture mass-flow ratios (M = 0.6), the lip is separating, leading to thickening of the cowl boundary layer and a loss of recovery.

The inlet was tested in the unstarted mode at angle of attack up to 8°. Figure 70 shows engine-face recovery and distortion versus angle of attack at three different Mach numbers. Each curve corresponds to a constant corrected engine flow (constant plug setting). At Mach 0.6 the plug setting corresponds to a C_m of 0.90, which is just prior to the occurrence of the lip separation. At Mach 0.95 the performance is shown at a C_m of 0.98; i.e., at only 2% less than the maximum ideal capture flow. At Mach 1.3, data are shown for the minimum plug setting that will maintain buzz-free operation in the 0° to 8° angle-of-attack range. This plug setting corresponds to a C_m of 0.90 at $\alpha = 0°$ or about 0.02 W_L normal shock spillage.

BLEED HOLE ROUGHNESS AND VORTEX GENERATORS

The supersonic diffuser bleed system and the subsonic diffuser vortex generators are designed primarily to control or improve the inlet flow under started inlet conditions. During transonic operation, these components may create flow disturbances causing a reduction in inlet performance. A three-part study was conducted to investigate these effects. Configuration 1 was used as the baseline. In configuration 46 the centerbody forward bleed holes (plenums F1 and F2) were plugged to evaluate the effects of surface roughness due to inactive bleed holes. These are the largest and most forward bleed holes and, thus, were expected to have the largest influence on inlet performance and maximum capture flow. In configuration 47 the forward centerbody bleed holes were reopened, and all active bleed exits were sealed to determine the effects of bleed on transonic performance. In configuration 48 the bleed exits were opened up again, and vortex generators were installed on the centerbody.

Figures 71 and 72 show the effects of the bleed system on the inlet recovery and distortion at Mach 0.6 and 0.95, respectively. The inlet performance increased when the inactive bleed holes were plugged (conf. 46) and decreased when the active bleed exits were sealed (conf. 47). The mechanisms for these performance changes are illustrated in figure 73. The two upper plots show the boundary-layer pitot-pressure profiles just downstream of centerbody plenum F2. As it will be recalled in configuration 1, the bleed holes in F1 and F2 are open but not bleeding. In configuration 46 these holes are plugged and the surface smoothed. Figure 73 indicates that smoothing of the surface over the inactive bleed holes improves the boundary-layer profile leading to an increase of about 0.005 P_{T_O} in engine-face recovery for the condition shown ($C_m \sim 0.94$), or an increase of about 0.01 P_{T_O} near the maximum capture mass-flow ratio.

The lower plots in figure 73 compare the boundary-layer profiles at cowl rake 5 with open and sealed bleed exits. Closing of the exits affects primarily the cowl, since little bleed is removed from the centerbody in the transonic mode. Cowl rake 5 is located downstream of the last bleed region. Figure 73 indicates that bleed significantly improves the boundary-layer profile at Mach 0.95. For the configuration shown, the total bleed is approximately 0.032 W_L; the corresponding improvement in recovery is approximately 0.007 P_{T_O}. The effect of bleed can also be seen at Mach 0.6, although to a lesser extent. The experimental maximum capture mass-flow ratio for configuration 46 (forward centerbody bleed holes plugged and smooth) is compared with theory as well as with the maximum capture mass-flow ratio for configuration 1 (surface roughness from inactive holes) in figure 74. The capture flow in configuration 46 deviates from the ideal flow by less than 0.8% in the subsonic Mach number range.

Figures 75 and 76 show the effects of centerbody vortex generators on the transonic performance of the inlet at Mach 0.6 and 0.95, respectively. With the generators installed, the inlet recovery is reduced by approximately 0.01 P_{T_O} at Mach 0.6 and approximately 0.007 P_{T_O} at Mach 0.95 with a slight increase in distortion. In the transonic mode the vortex generators are located approximately 0.6 lip radius downstream of the inlet lip. In figure 77 the VG effect can be observed at the compressor face as a general reduction in the recovery over about 70% of the area outward from the centerbody support tube. Since the generators are considerably forward of the compressor face, sufficient mixing has taken place to make the loss of recovery nearly uniform throughout the affected area.

CONCLUDING REMARKS

An axisymmetric mixed-compression inlet was designed for a cruise Mach number of 3.5. Design of the internal contours and of the boundary-layer bleed system was accomplished through the application of an analytical design procedure. A large-scale model of the inlet was tested in the NASA-ARC Unitary Plan Wind Tunnels from Mach 0.6 to 3.5.

The test results showed overall agreement with design predictions of the flowfield structure and boundary-layer development in the supersonic diffuser. In general, the bleed rate requirements were accurately predicted, but the actual bleed flow rates were lower than predicted by about 20%. The best performance at Mach 3.5 was obtained with two extra rows of holes open in one of the forward cowl bleed plenums as compared to the design bleed geometry. The best off-design performance was obtained with two extra rows of holes open in the first and second throat plenums of the centerbody. Neither of these changes increased the bleed flow rate above the predicted requirements.

The design point performance of the inlet was compared with that of the NASA model reported in reference 2. Both inlets were designed for about 98.5% inviscid total-pressure recovery in the throat. The best configuration tested on the present model had 3% higher recovery at the engine face for the same amount of bleed. Furthermore, this performance was obtained with a subsonic diffuser area ratio of 5.0 to 1 compared to about 3.5 to 1 on the NASA model. It is significant that the present inlet performed better than the NASA inlet at the design point with the initial bleed configuration demonstrating the validity of the analytical design procedures. It was possible to obtain only a slight improvement in performance by redistributing the bleed and installing vortex generators.

In the started Mach number range, the total-pressure recovery downstream of the terminal normal shock exceeded 90% of the freestream total pressure. Significant total-pressure losses occurred in the subsonic diffuser below Mach 3.2. The losses are believed to be caused by the initial rapid increase in diffuser area just downstream of the throat, possibly coupled with inadequate centerbody throat bleed. While centerbody vortex generators did increase the engine-face recovery by about 1% at the design Mach number, no vortex generator pattern was found that would improve the off-design performance.

The feasibility of operating the inlet when coupled to a "wrap around" ramjet engine was evaluated. In this concept a turbojet is contained within an annular ramjet duct. At cruise operation the turbojet is shut off and accepts no airflow. Simulated cruise operation at Mach 3.5 did not affect inlet performance on the present model.

In the unstarted mode at transonic speeds, the inlet could capture over 99% of the theoretical maximum (choked) capture flow. Inlet performance increased when inactive bleed holes were sealed and decreased when plenum exits for the active bleed holes were closed. Additionally, recovery decreased when vortex generators were installed on the centerbody.

The following points should be noted with respect to future design work.

1. The bleed hole flow coefficients from reference 1 should be modified to reflect the findings from this test.

2. In a traveling bleed system a slight increase in the centerbody forward bleed rate is desirable during off-design operation to compensate for the roughness effects of inactive bleed holes.

3. The analytical boundary-layer transition and redevelopment criteria should be revised on the basis of the present findings.

4. Substantial gains could be achieved with the tested inlet by redesigning the subsonic diffuser to alleviate the separations encountered during off-design started operation. However, the transonic airflow capacity must be reduced to obtain significant improvements in the diffuser area distributions.

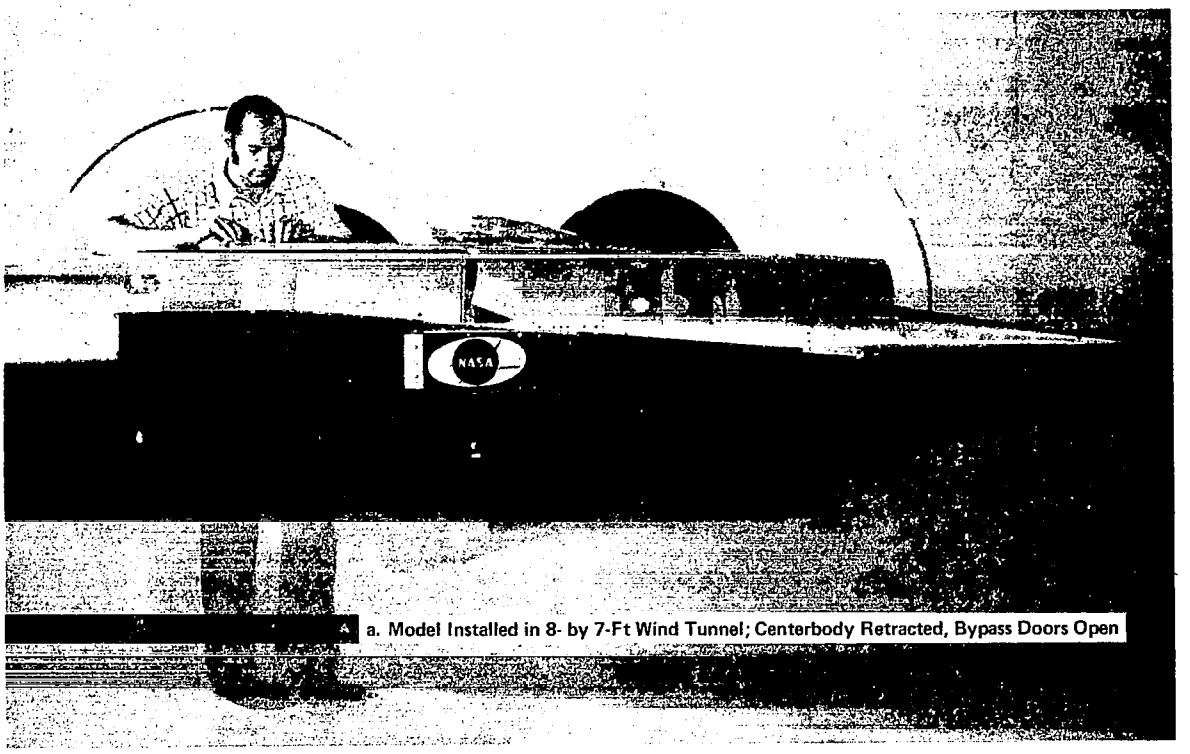

a. Model Installed in 8- by 7-Ft Wind Tunnel; Centerbody Retracted, Bypass Doors Open

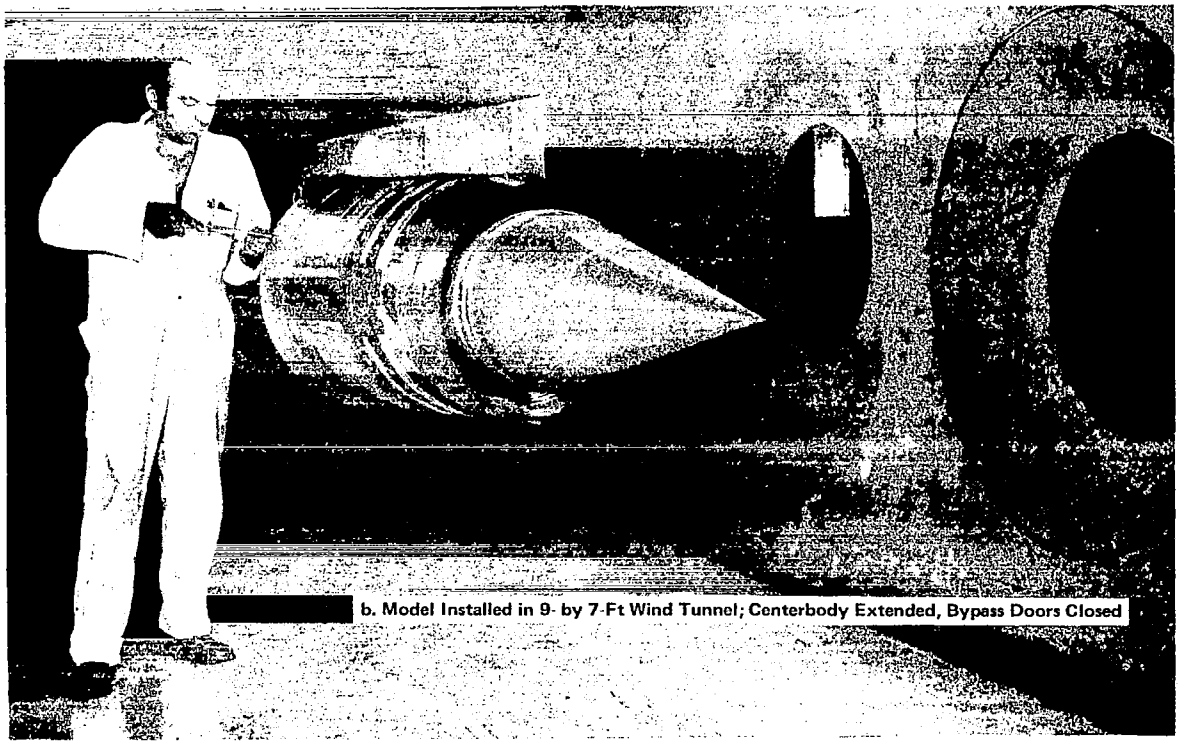

b. Model Installed in 9- by 7-Ft Wind Tunnel; Centerbody Extended, Bypass Doors Closed

Figure 1.—Mach 3.5 Inlet Model

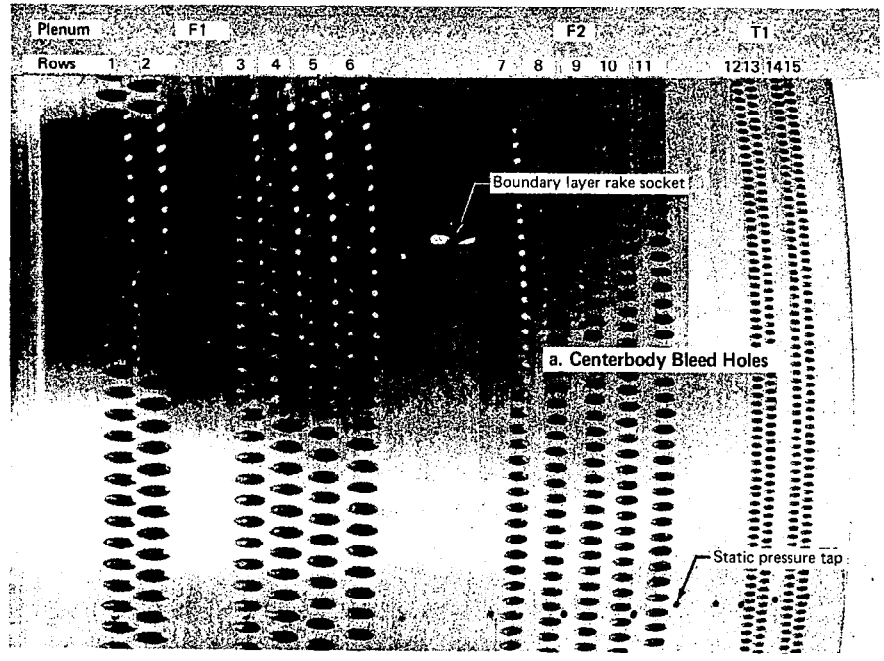

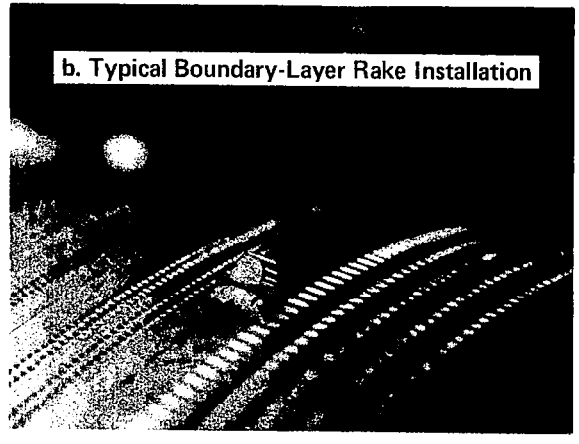

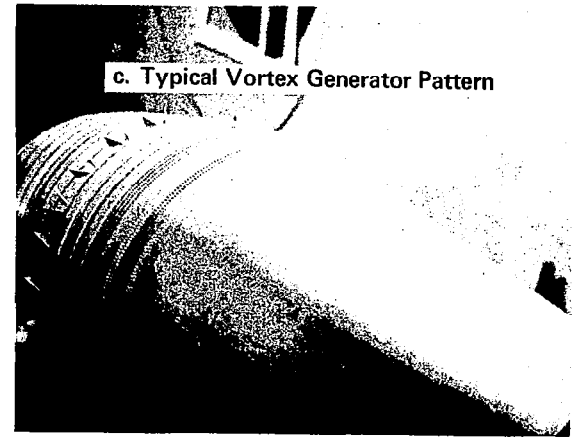

Figure 2.—Model Details

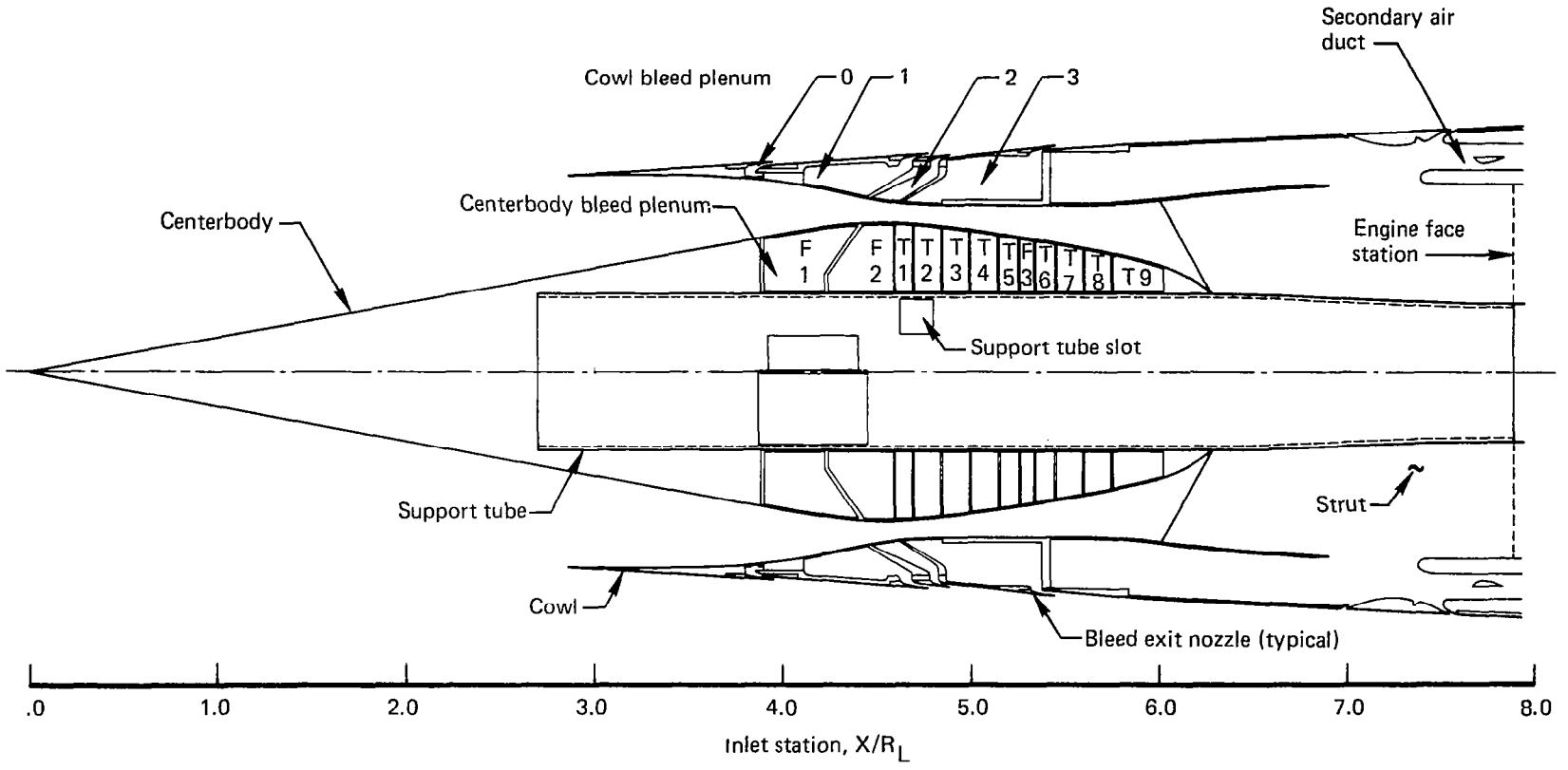

Figure 3.—Mach 3.5 Inlet Model Schematic

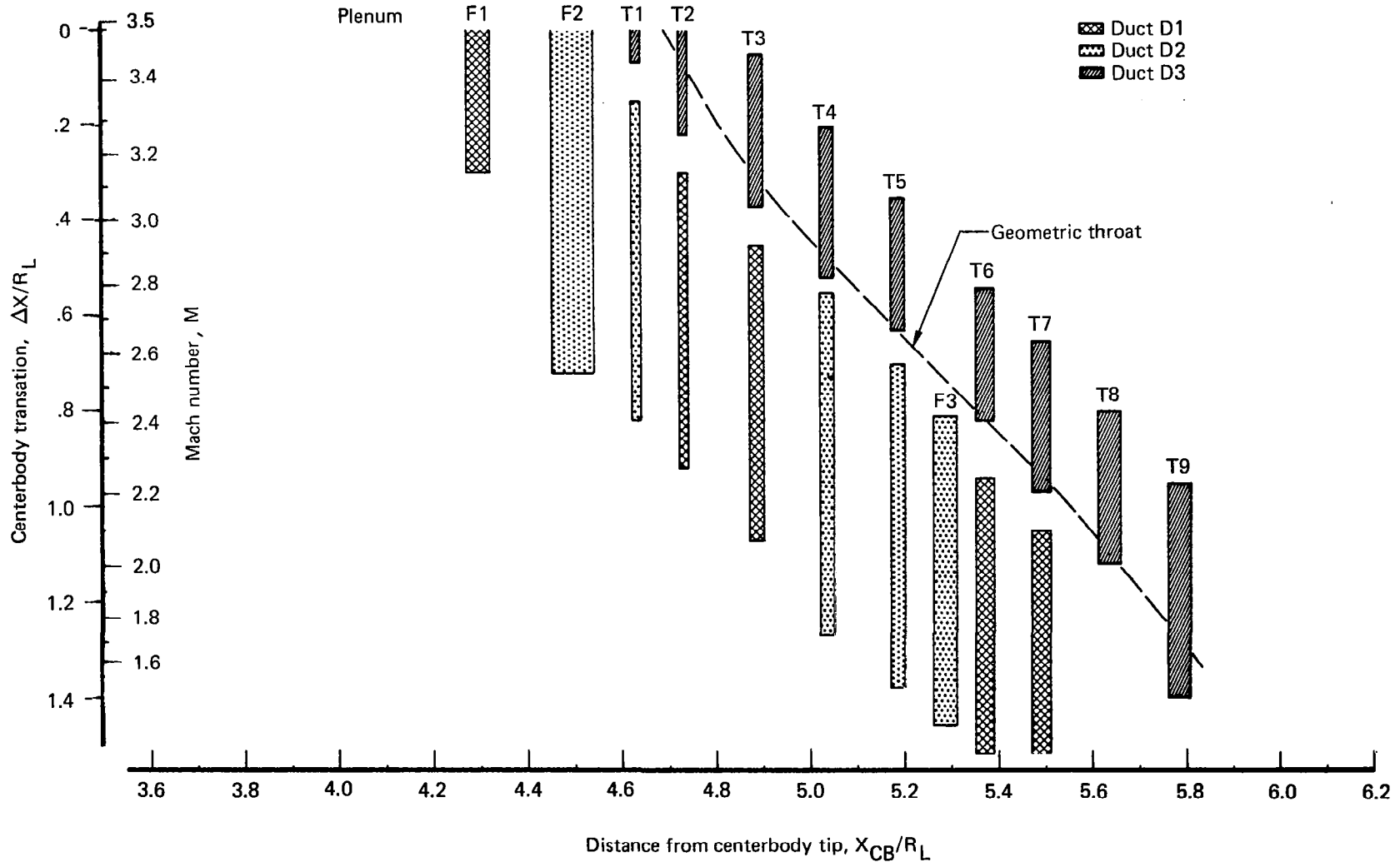

Figure 4.—Centerbody Bleed Schedule

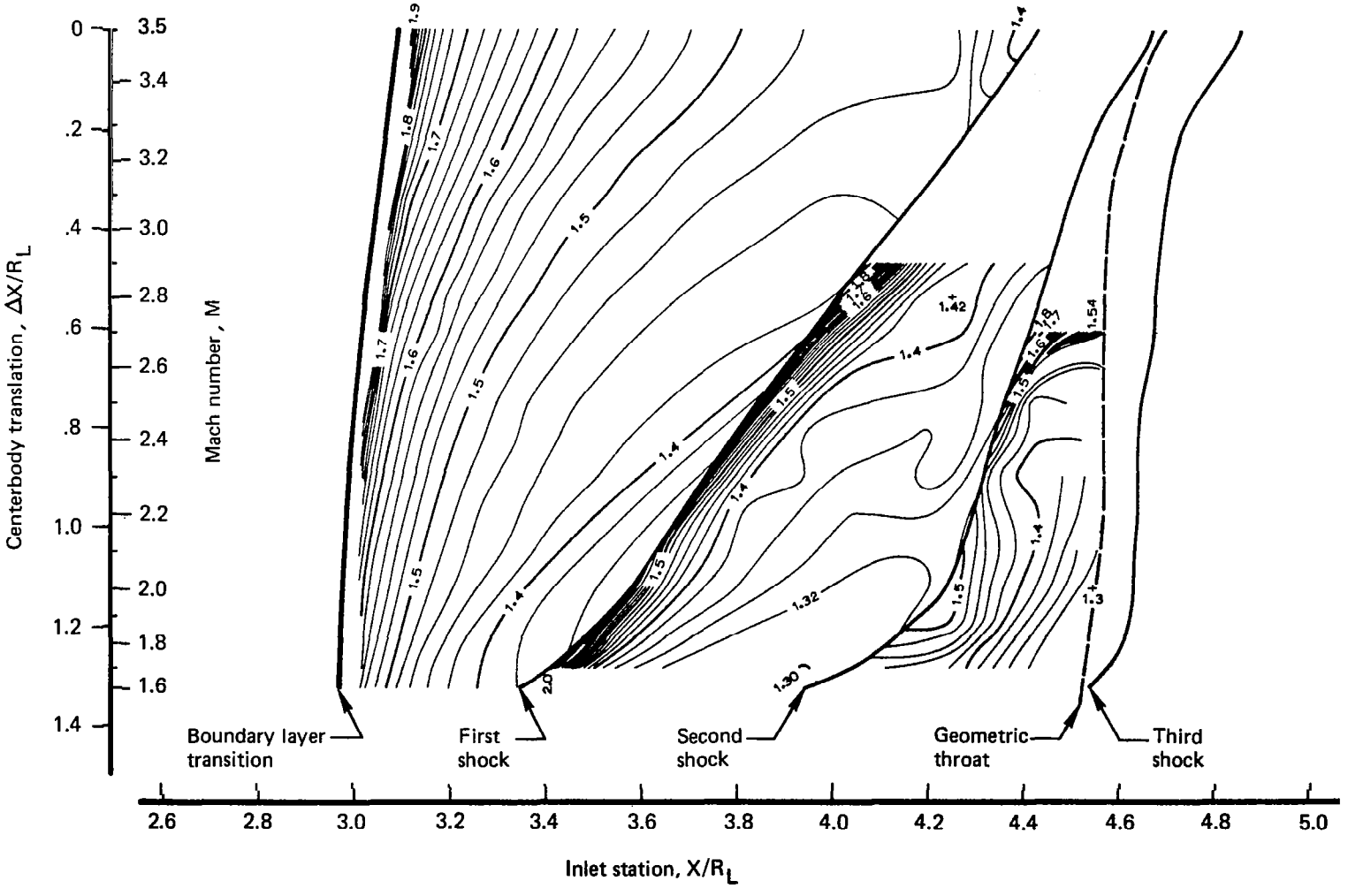

Figure 5.—Map of Cowl Boundary-Layer Shape Factor, H_i, No Bleed

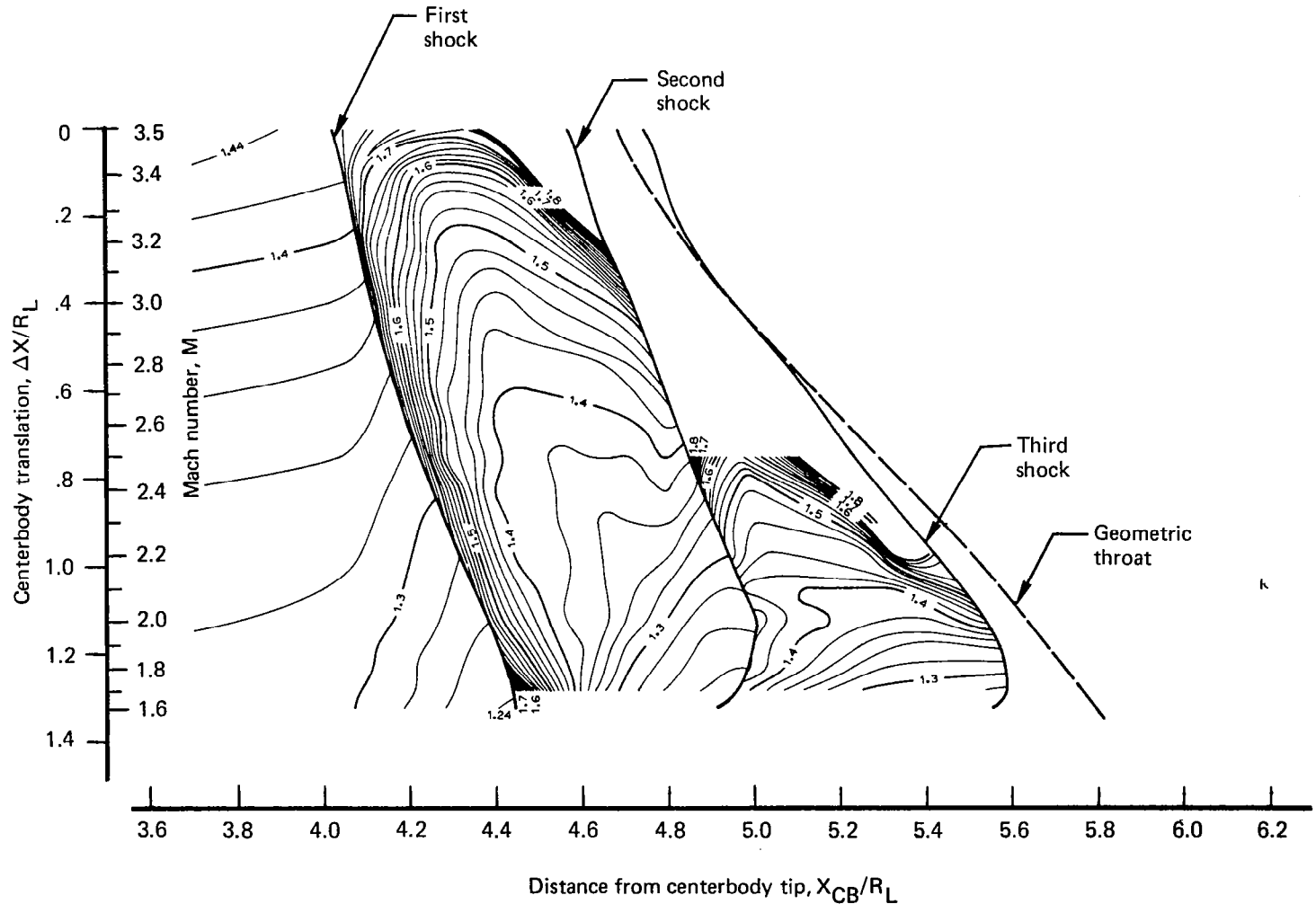

Figure 6.—Map of Centerbody Boundary-Layer Shape Factor, H_i, No Bleed

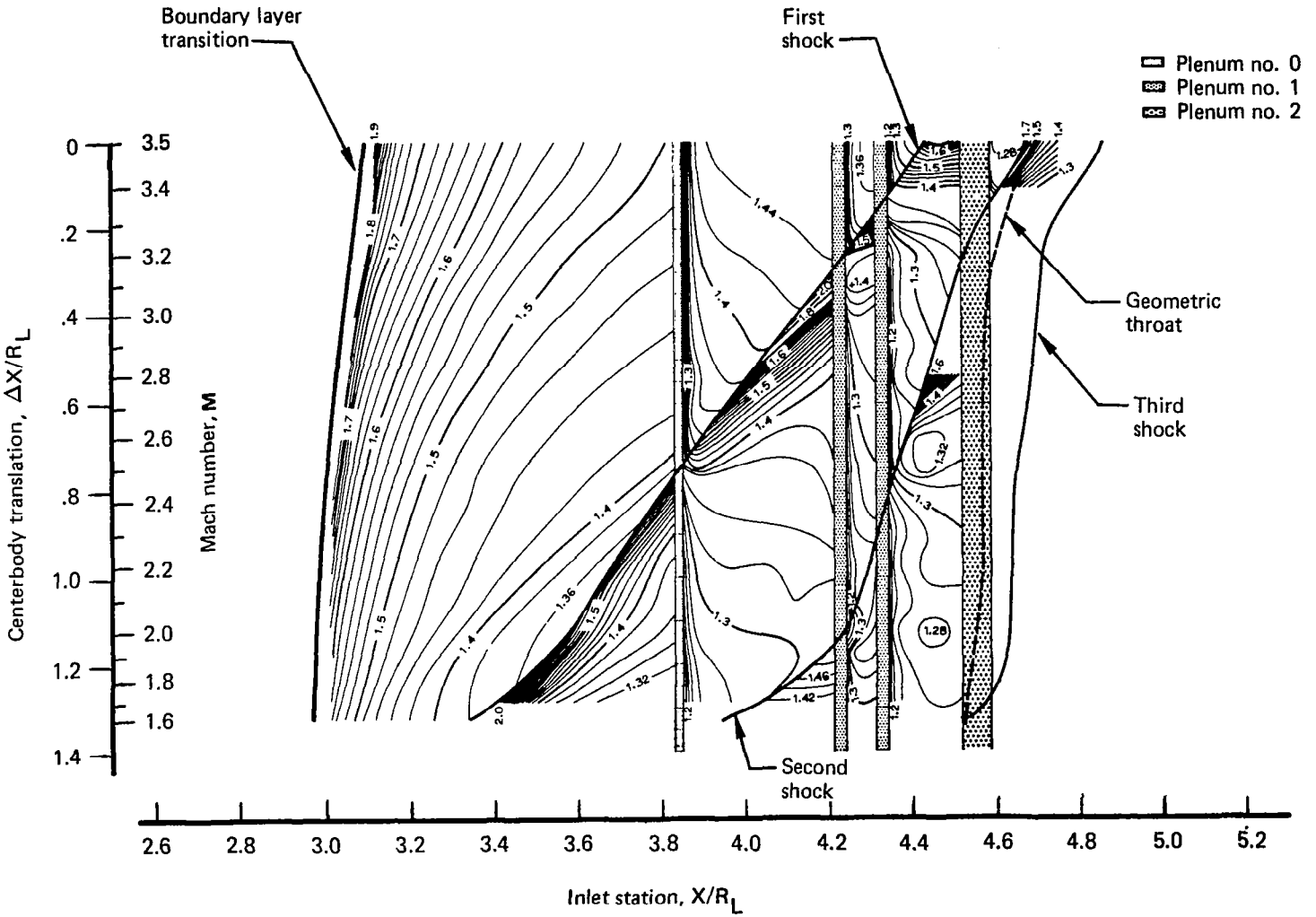

Figure 7.—Cowl H_i Map With Proposed Bleed System

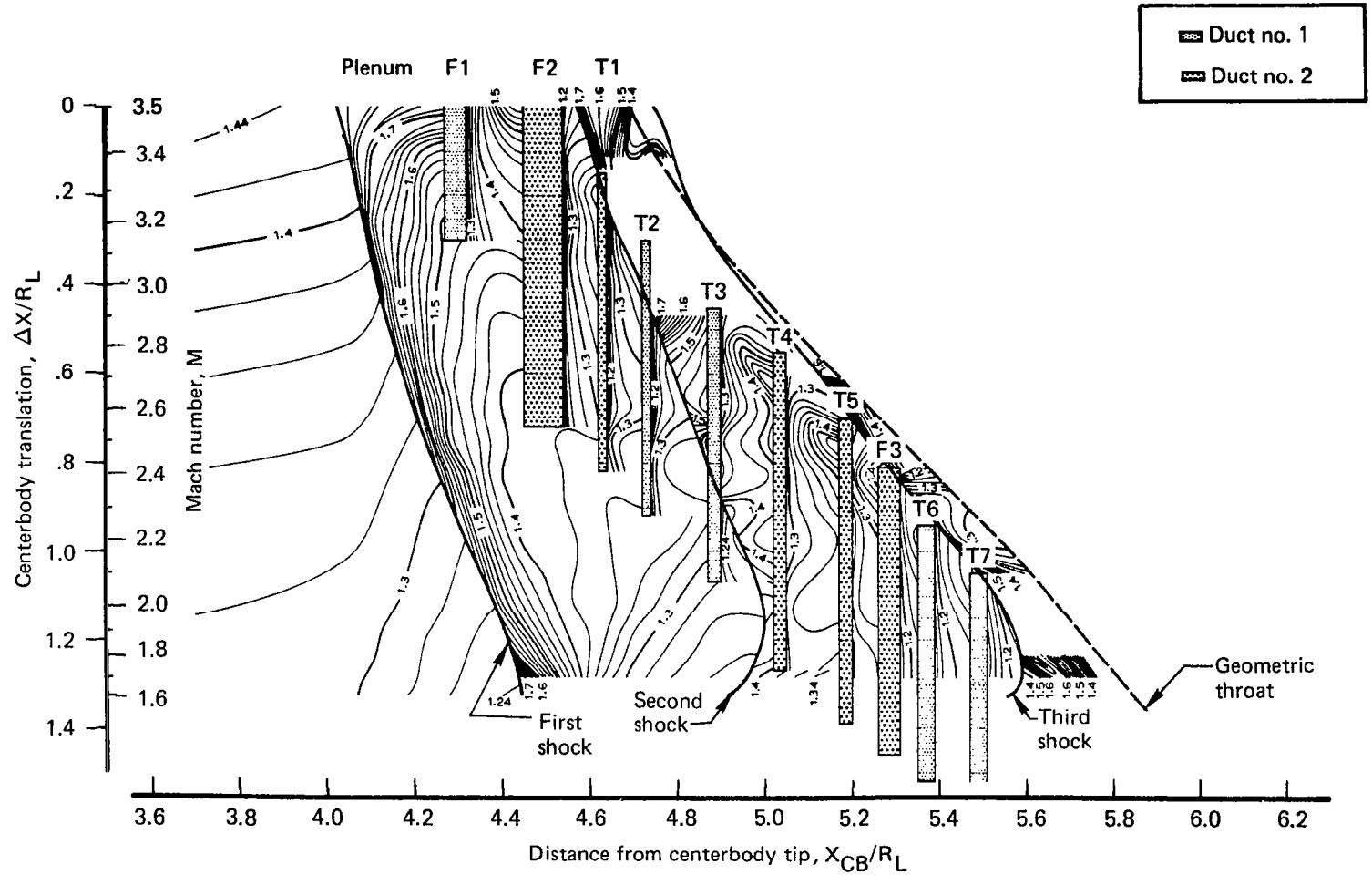

Figure 8.—Centerbody H_i Map With Proposed Bleed System

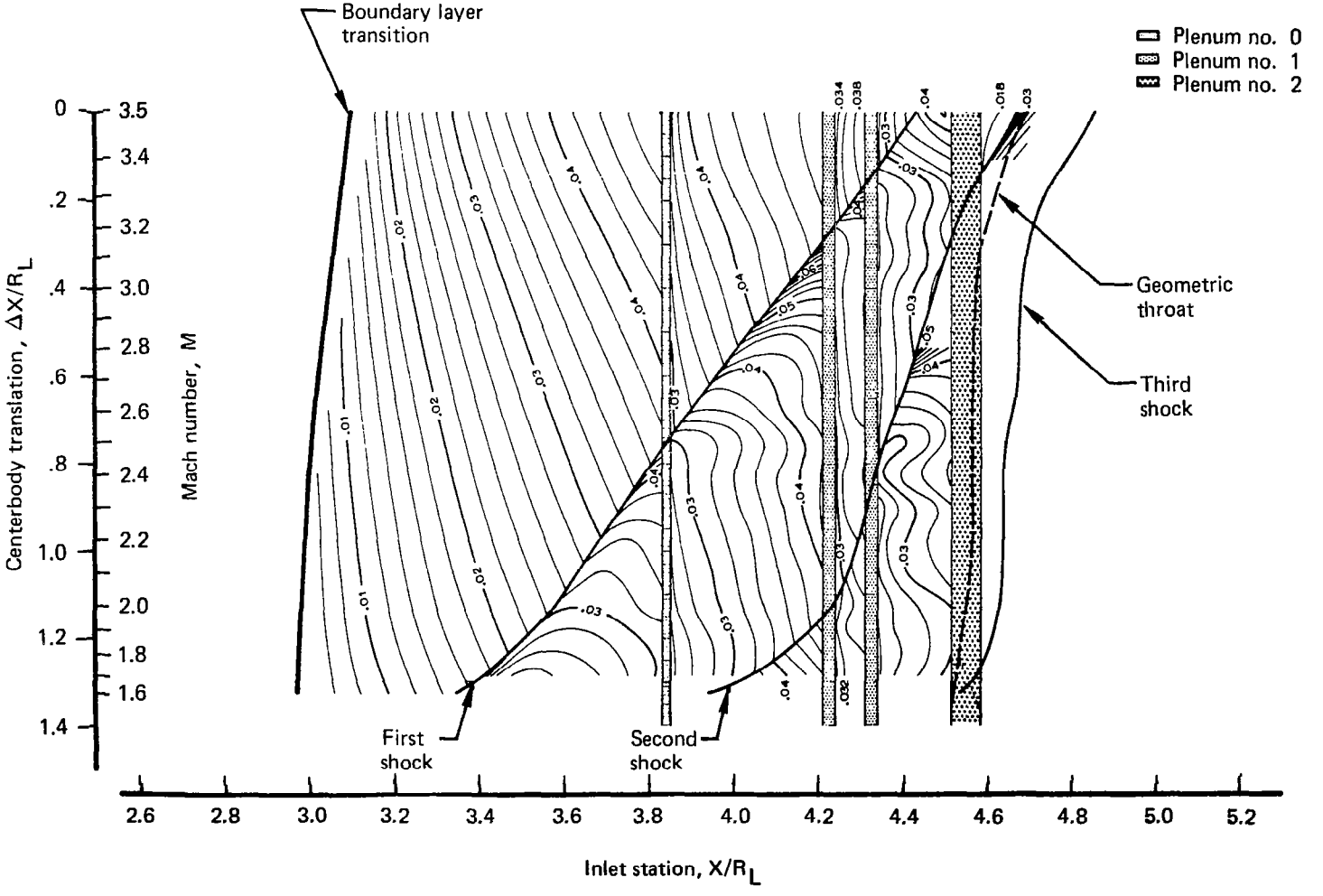

Figure 9.– Cowl δ Map With Proposed Bleed System*

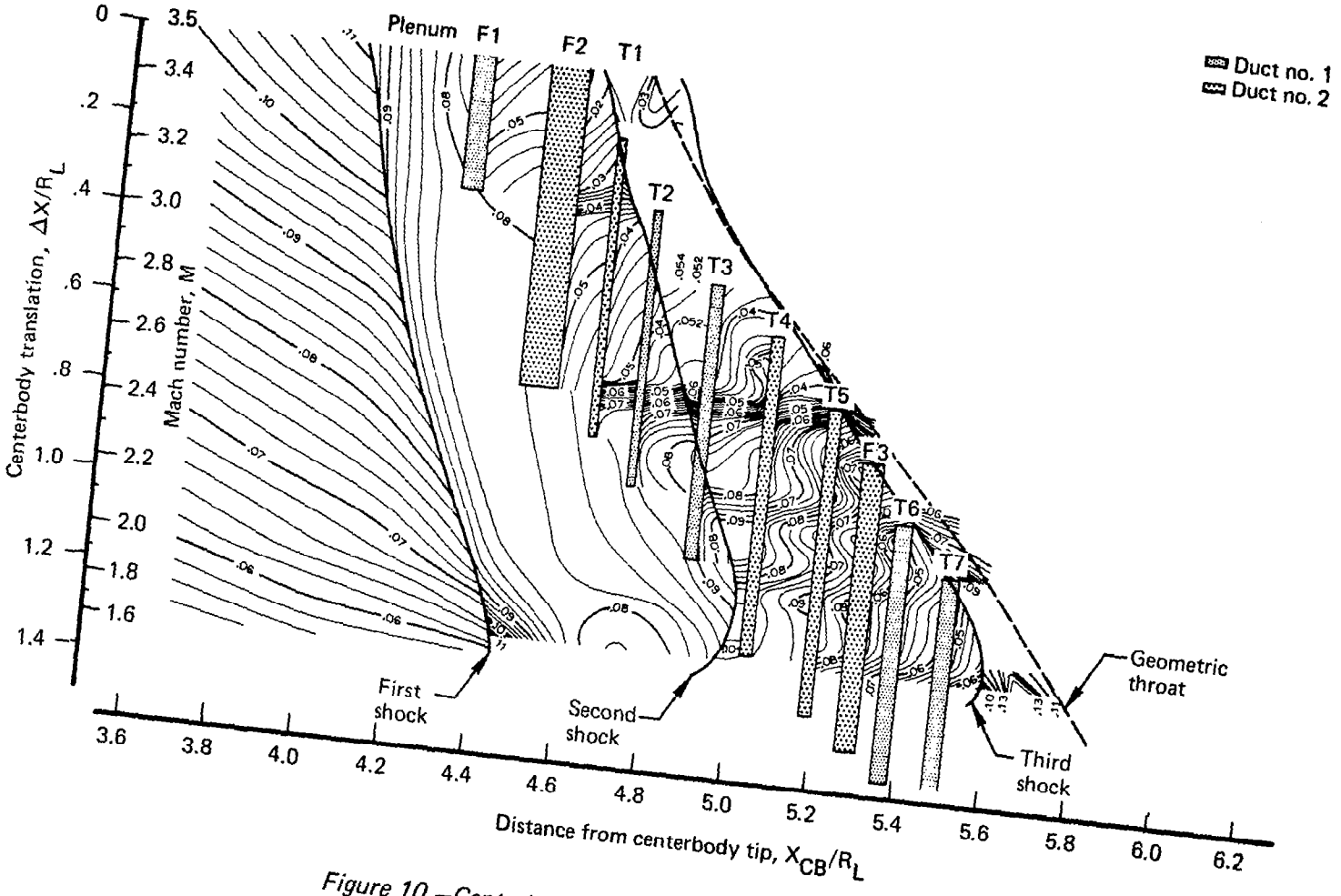

Figure 10.—Centerbody δ^* Map With Proposed Bleed System

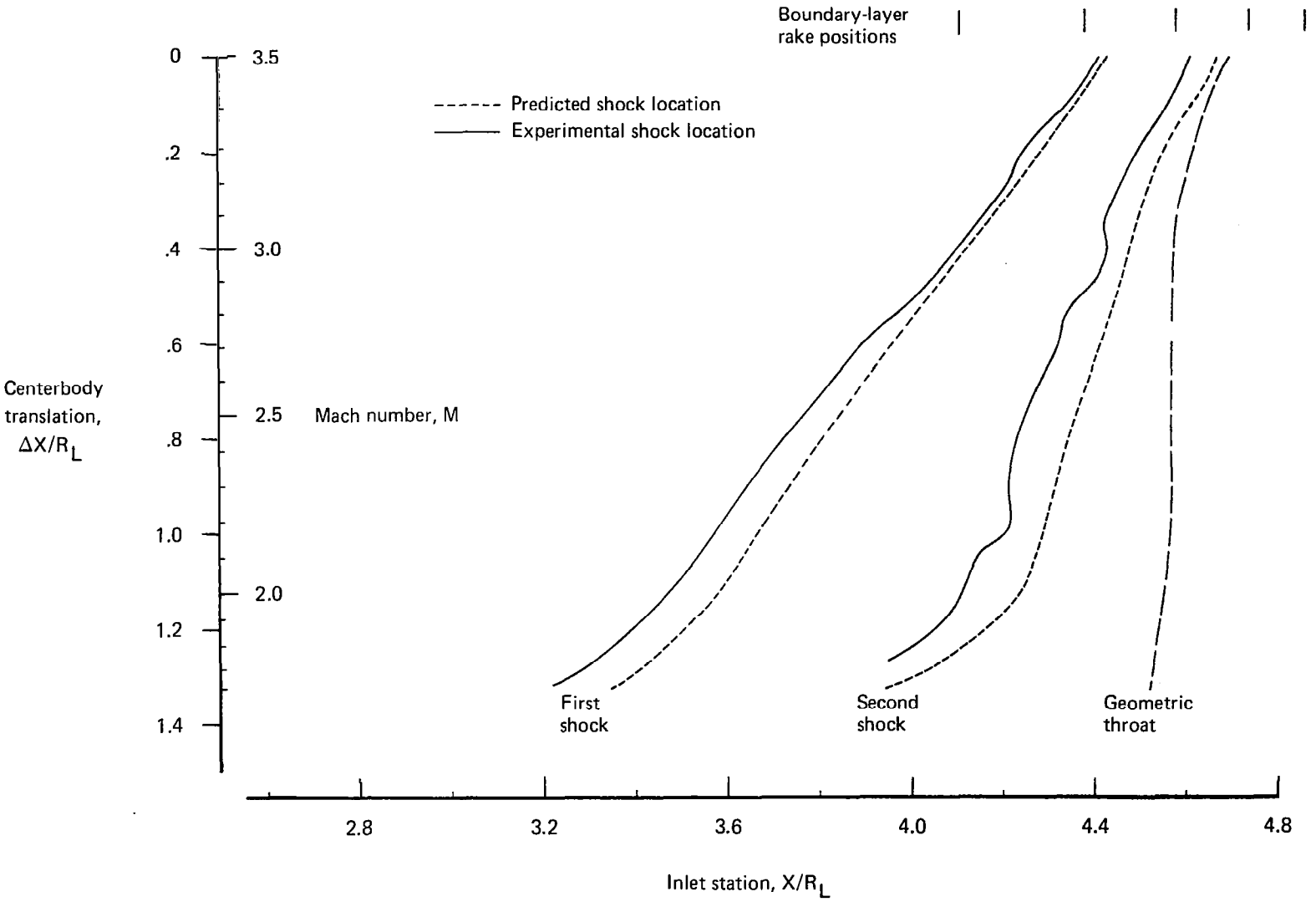

Figure 11.—Cowl Shock Map, Configuration 1

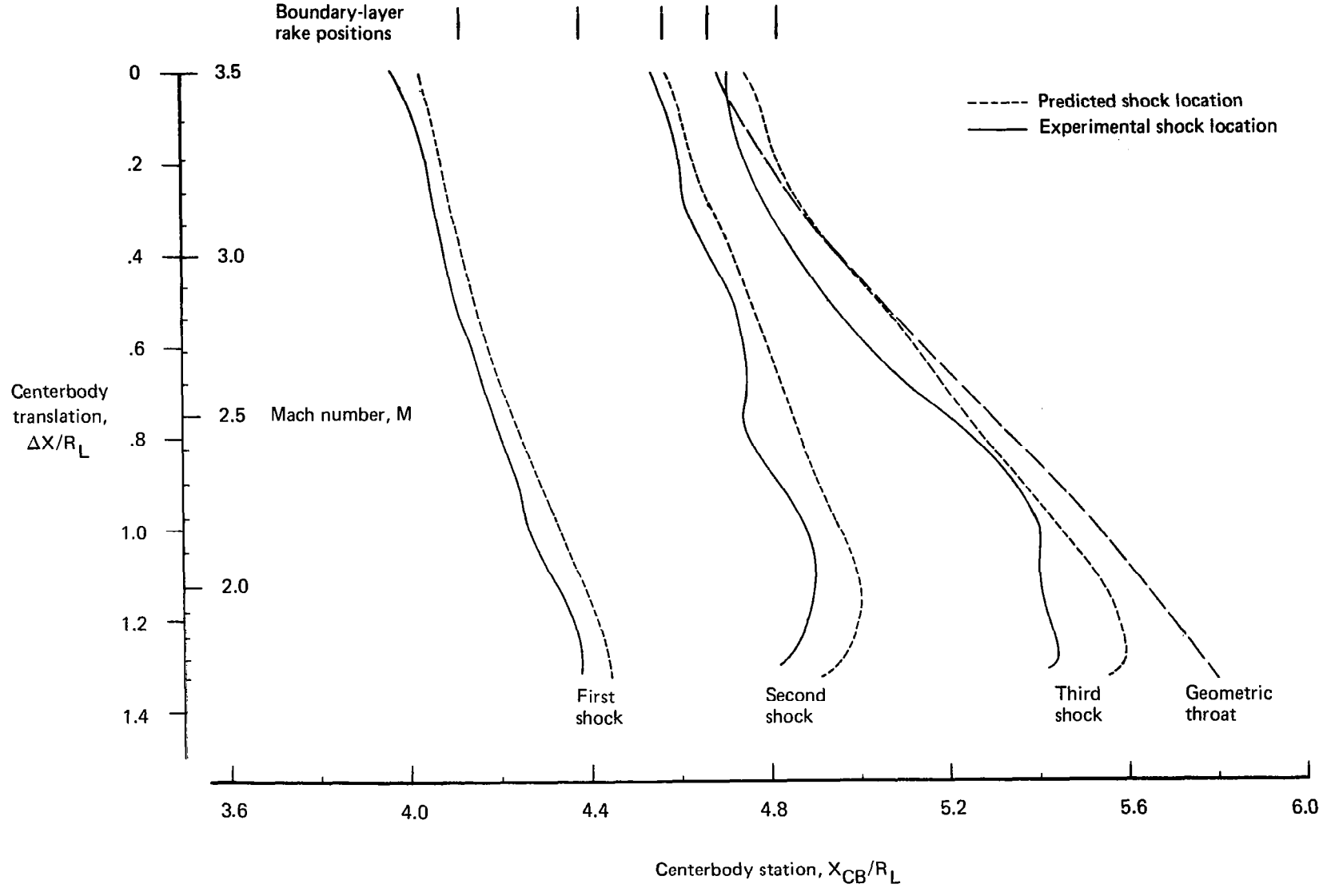

Figure 12.—Centerbody Shock Map, Configuration 1

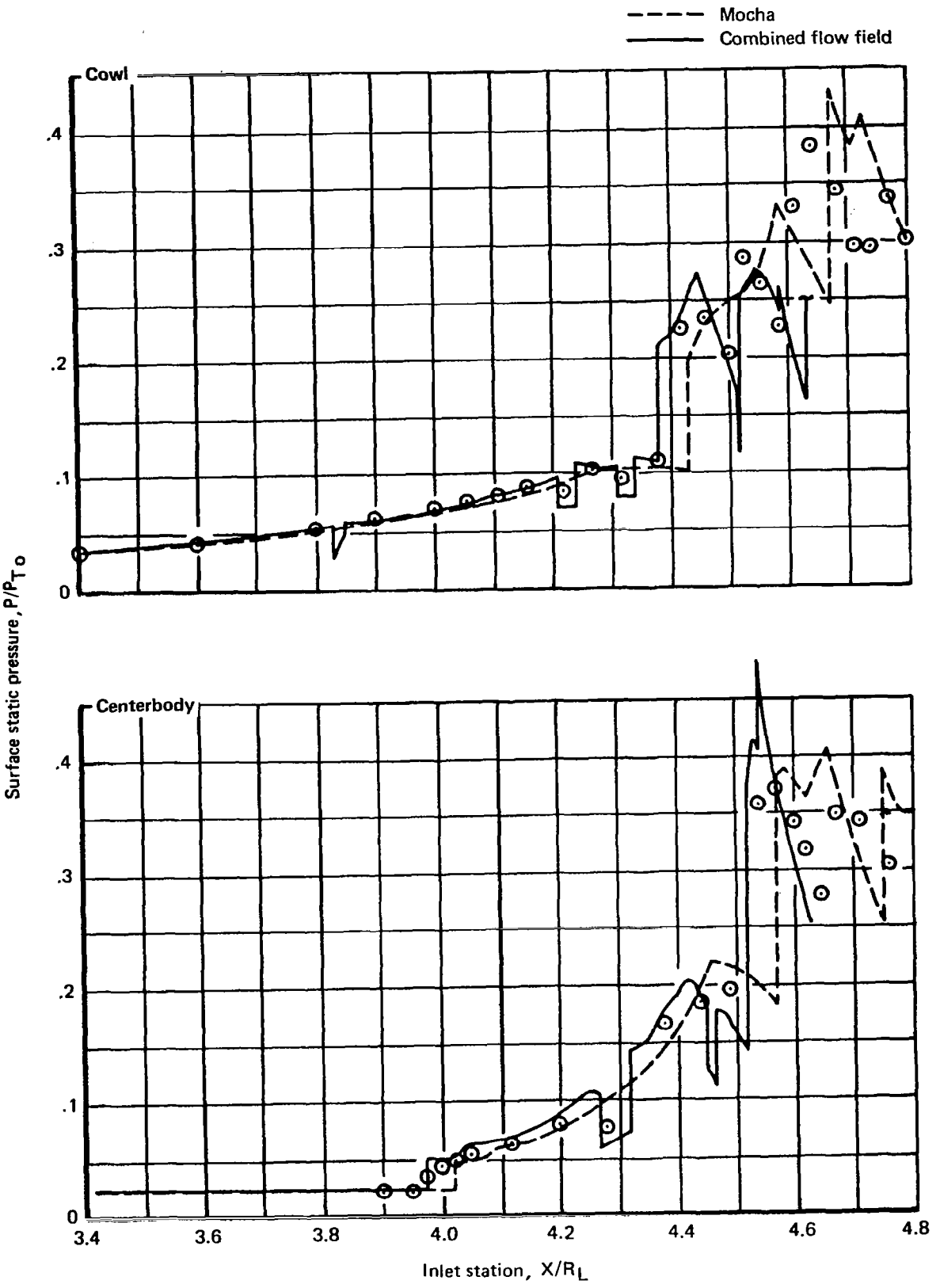

Figure 13.—Supersonic Diffuser Static-Pressure Profiles, $M = 3.5$, $\Delta X/R_L = 0$

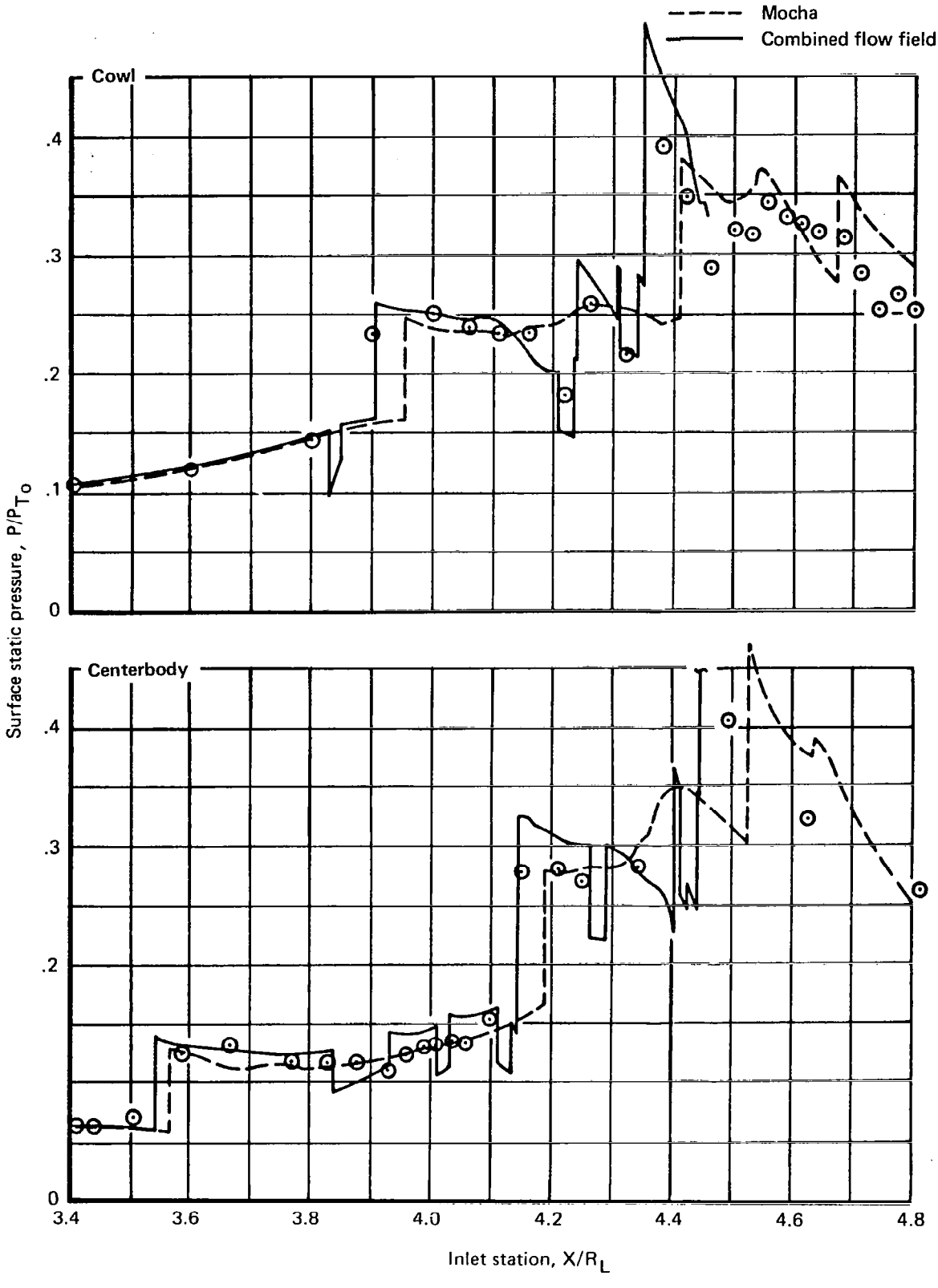

Figure 14.—Supersonic Diffuser Static-Pressure Profiles, M = 2.7, $\Delta X/R_L$ = 0.610

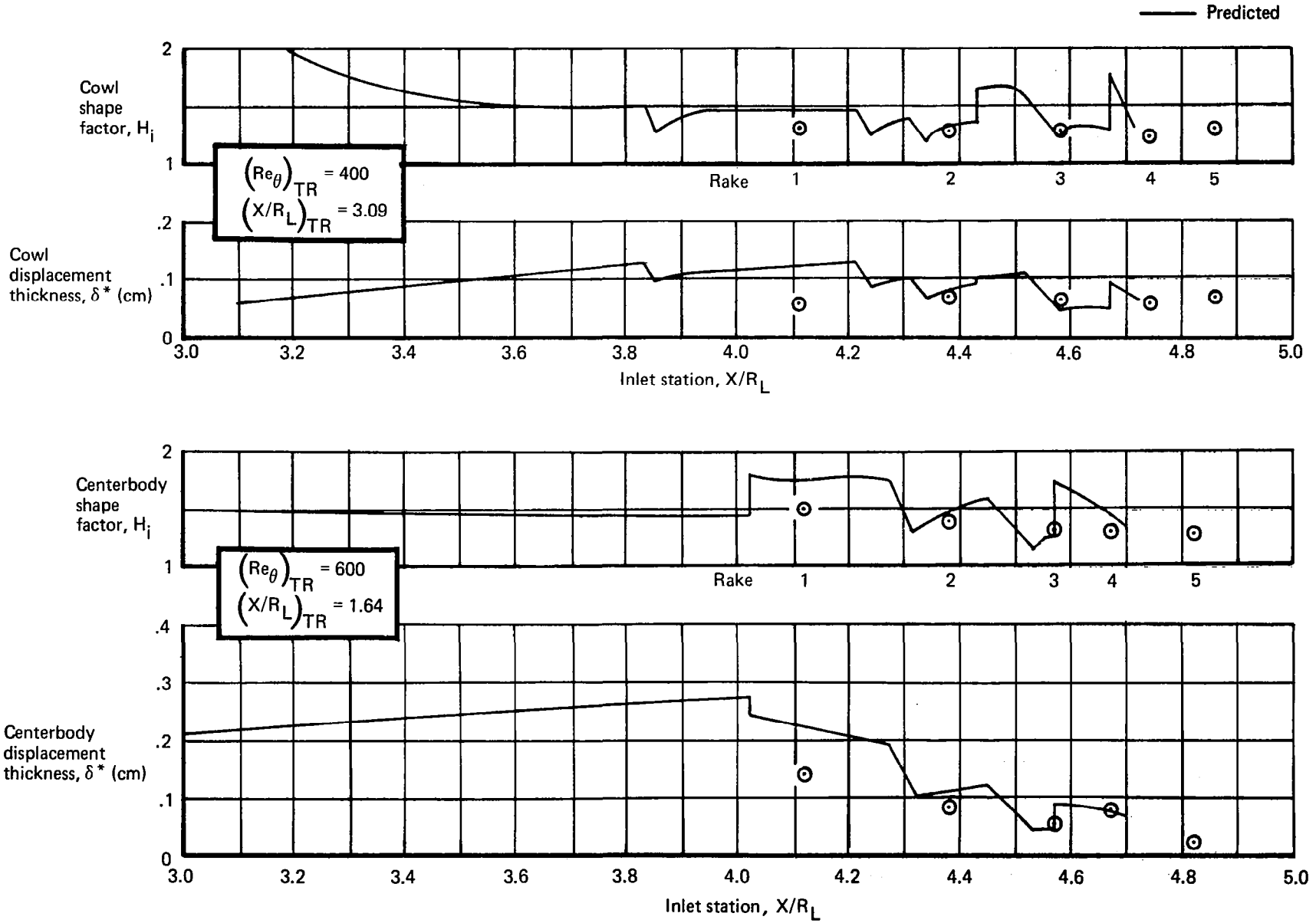

Figure 15.–Boundary-Layer Development, M = 3.5

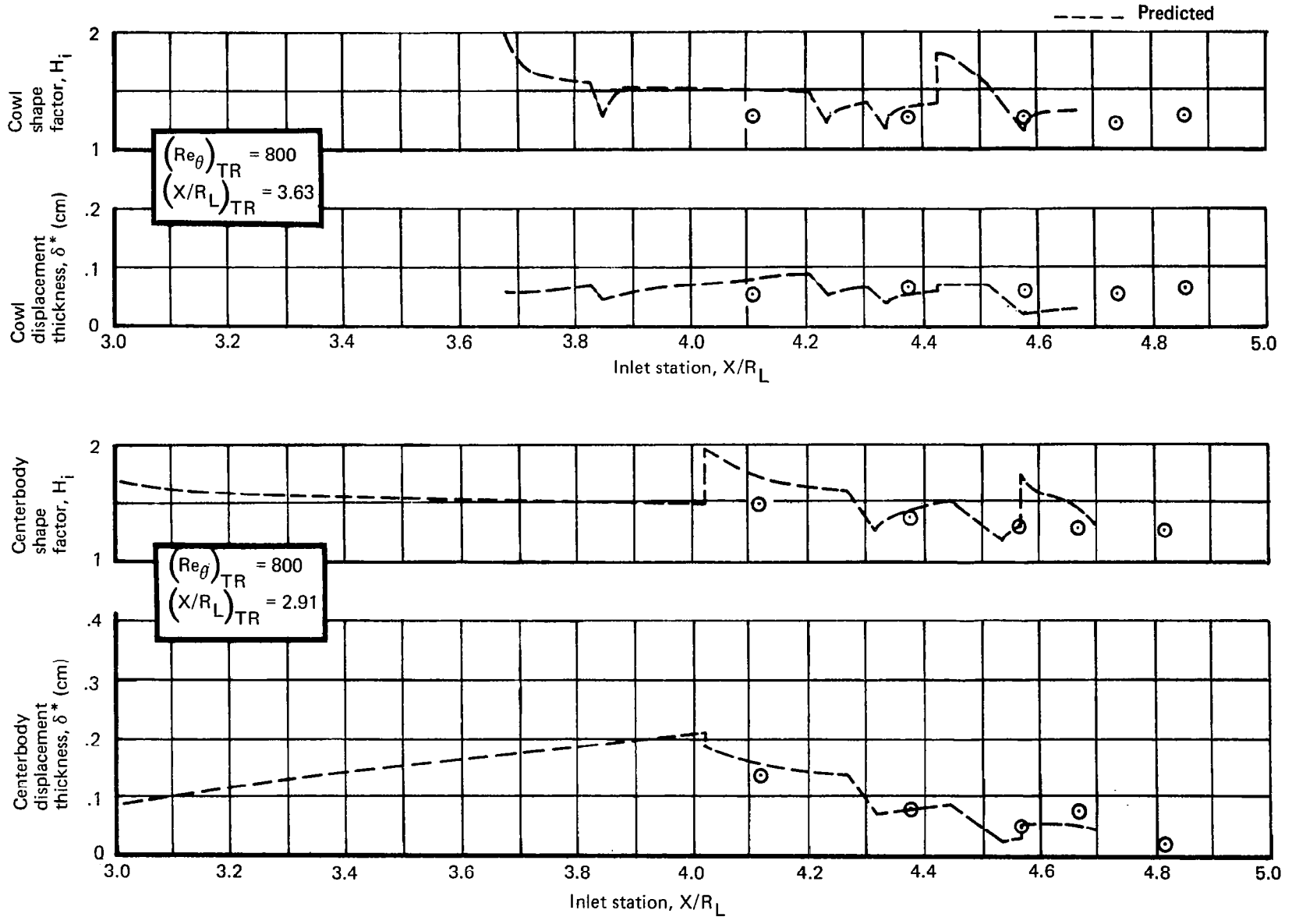

Figure 16.—Predicted Boundary-Layer Development With Revised Transition Criteria

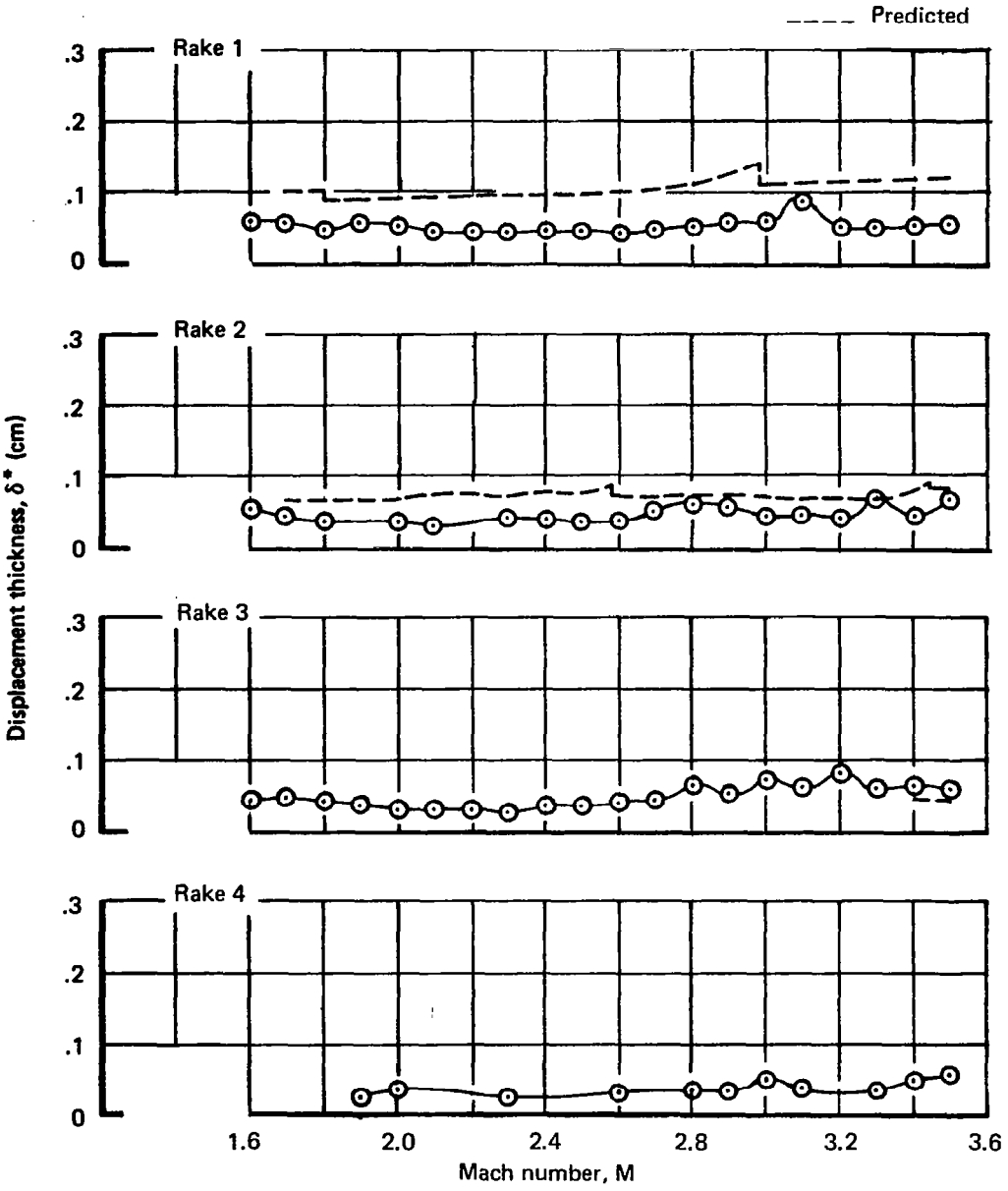

Figure 17.—Cowl Boundary-Layer Displacement Thickness

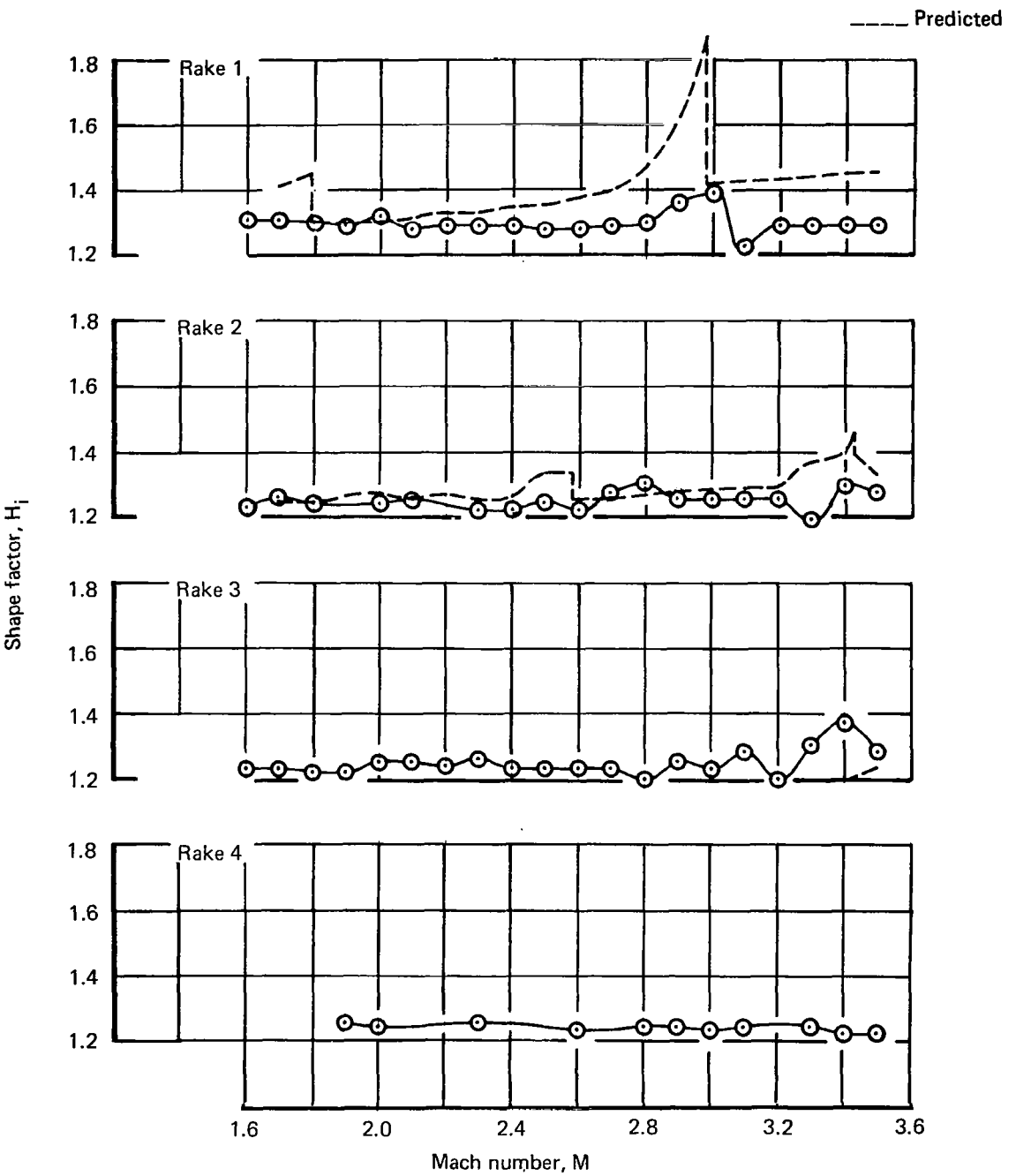

Figure 18.—Cowl Boundary-Layer Shape Factor

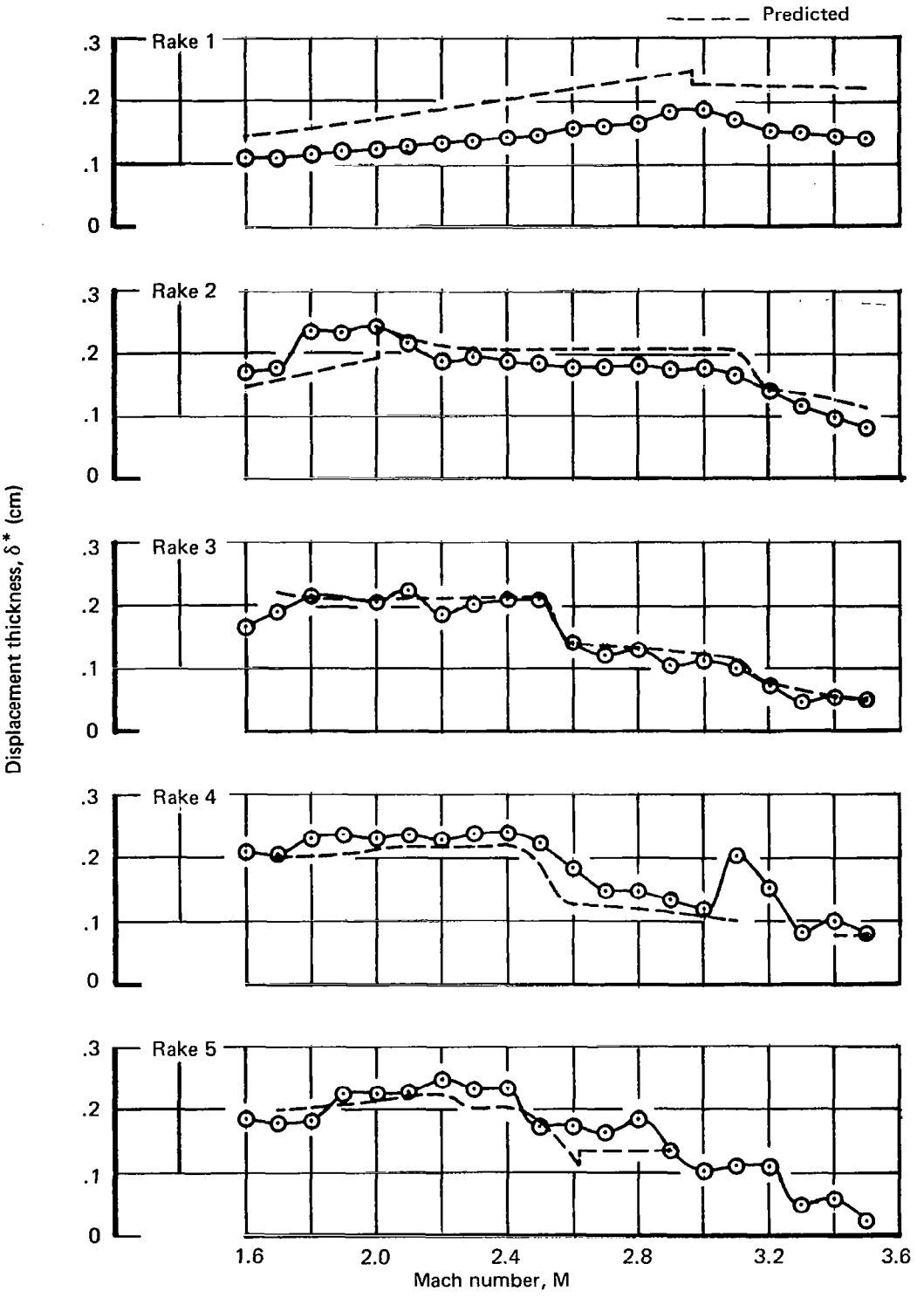

Figure 19.—Centerbody Boundary-Layer Displacement Thickness

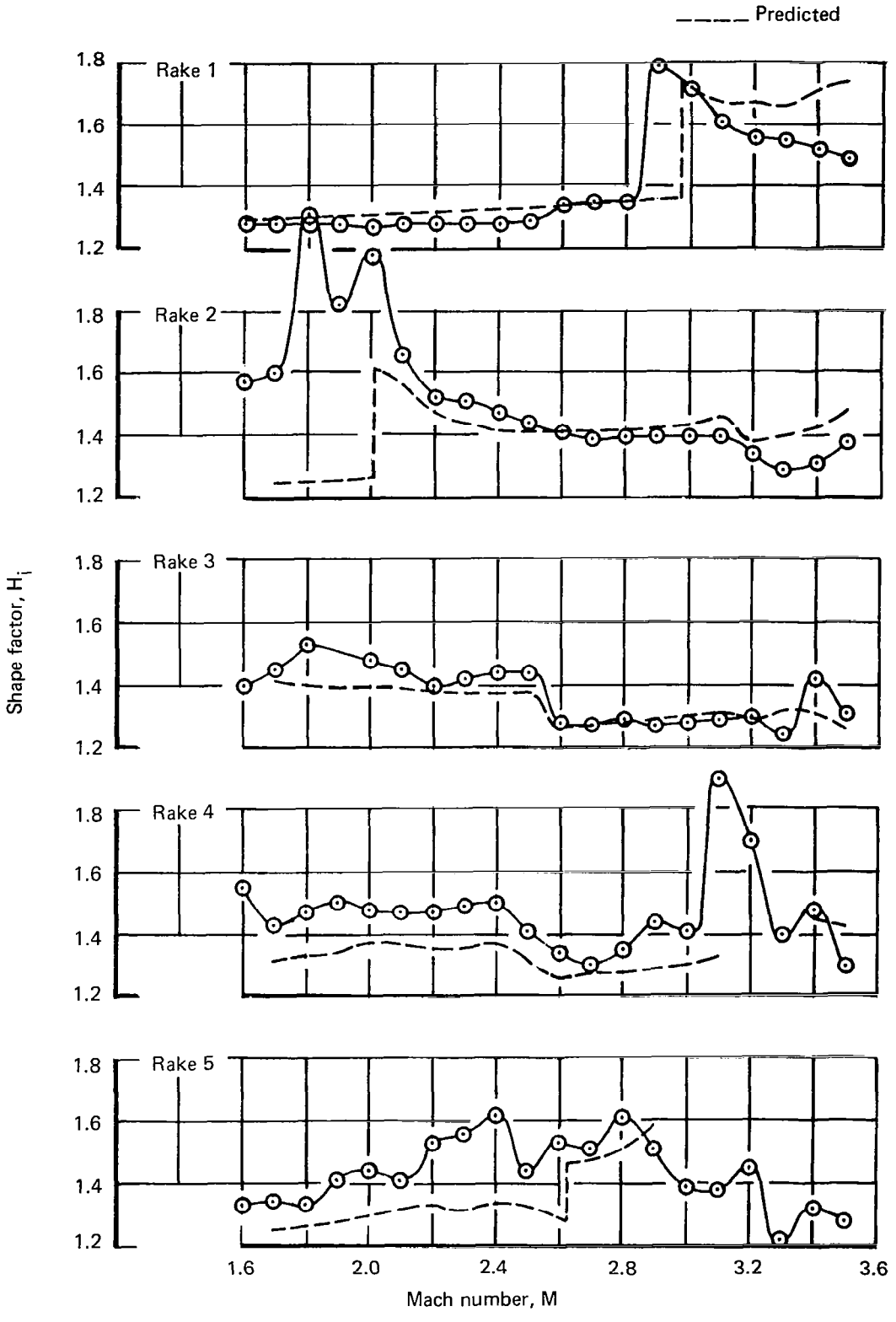

Figure 20.–Centerbody Boundary-Layer Shape Factor

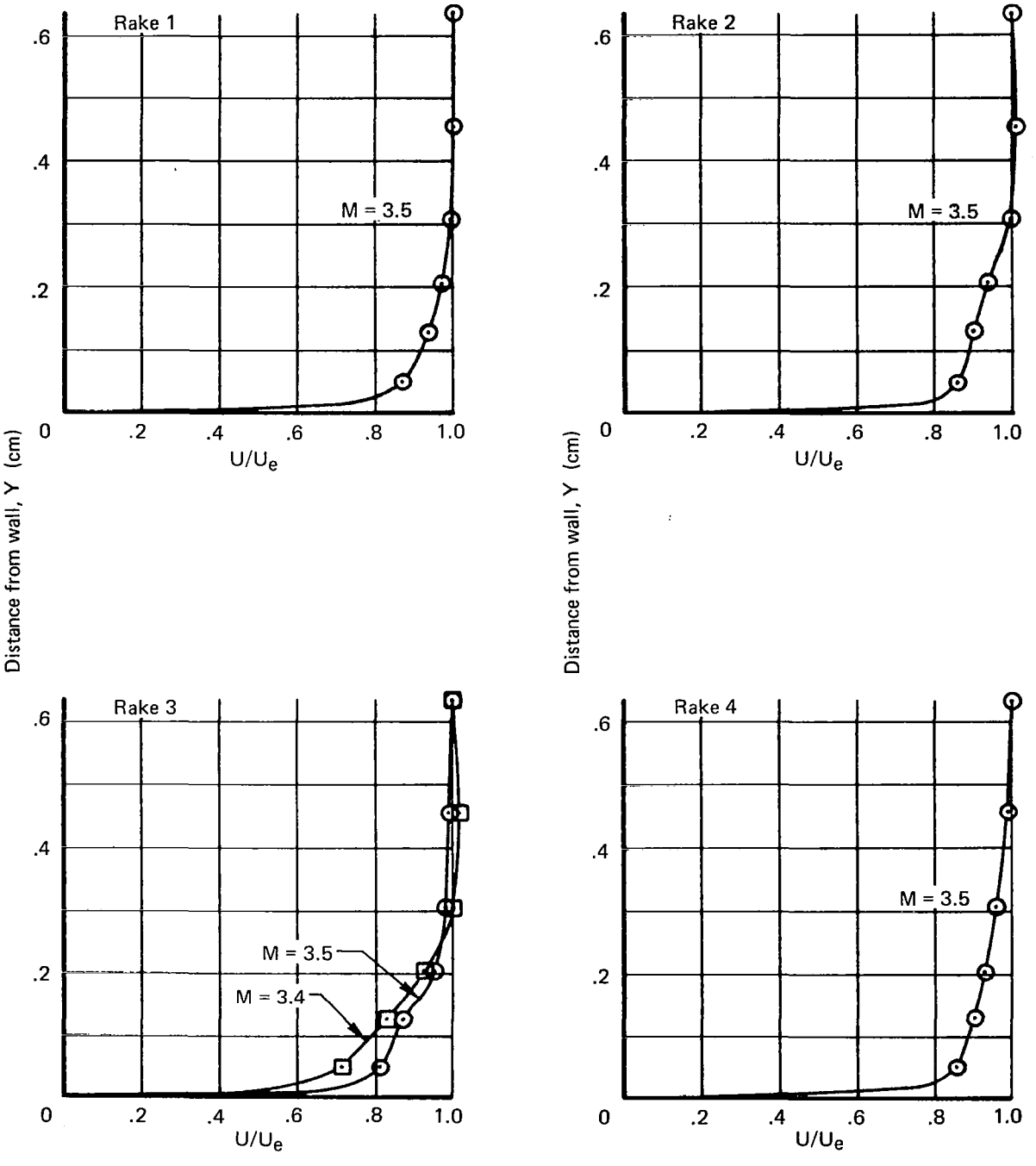

Figure 21.—Typical Cowl Boundary-Layer Profiles, Configuration 1

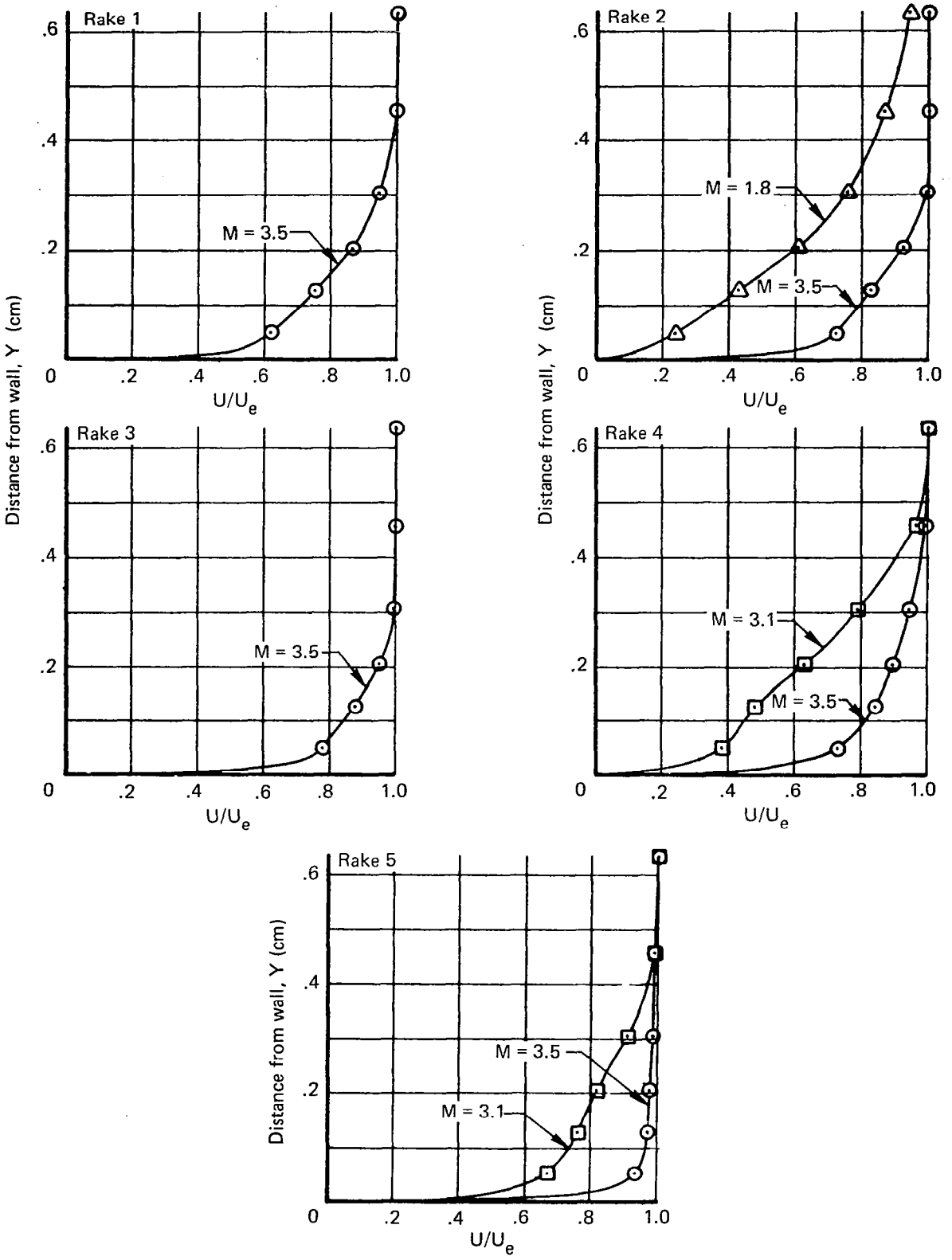

Figure 22.—Typical Centerbody Boundary-Layer Profiles, Configuration 1

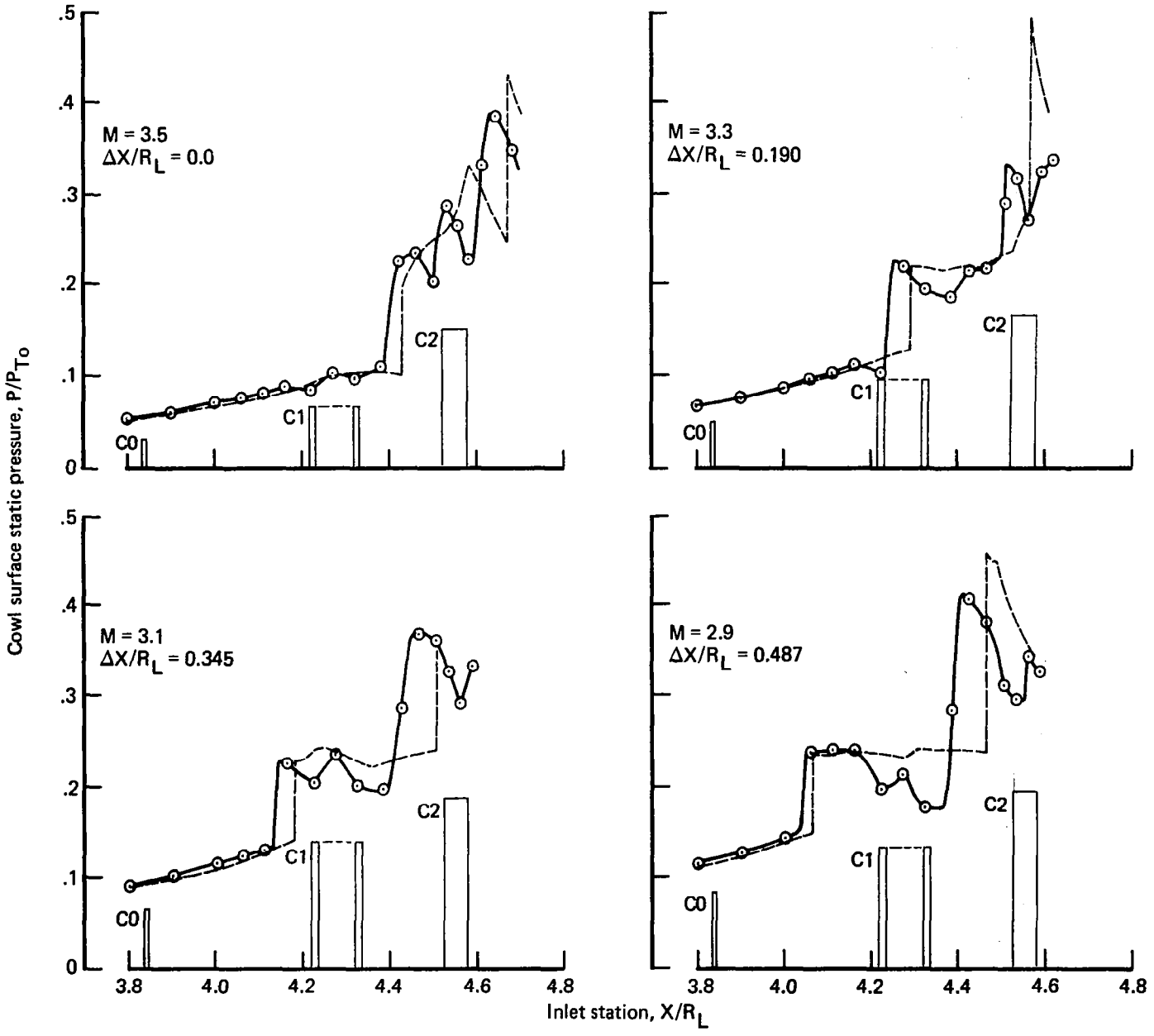

Figure 23.—Cowl Surface Static-Pressure Profiles Over Forward Bleed Regions

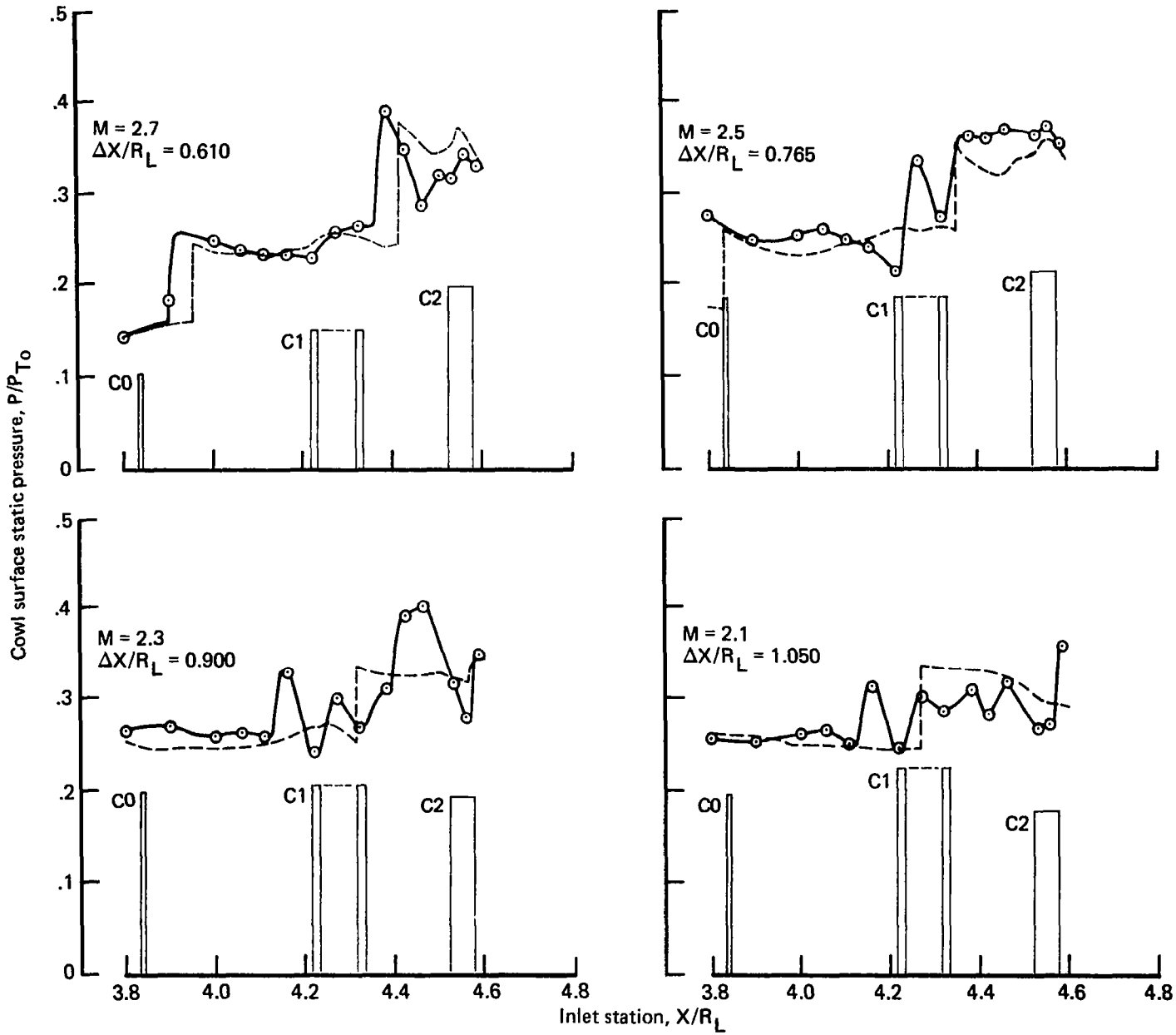

Figure 23.—(Continued)

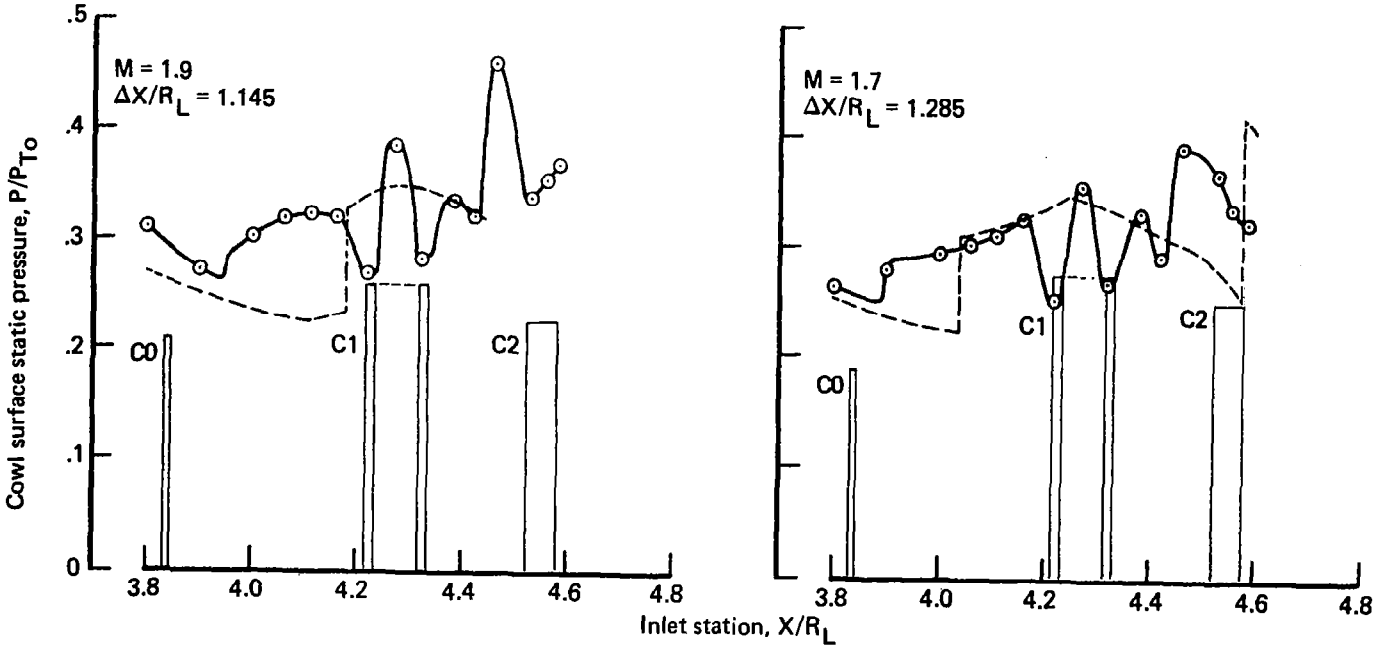

Figure 23.—(Concluded)

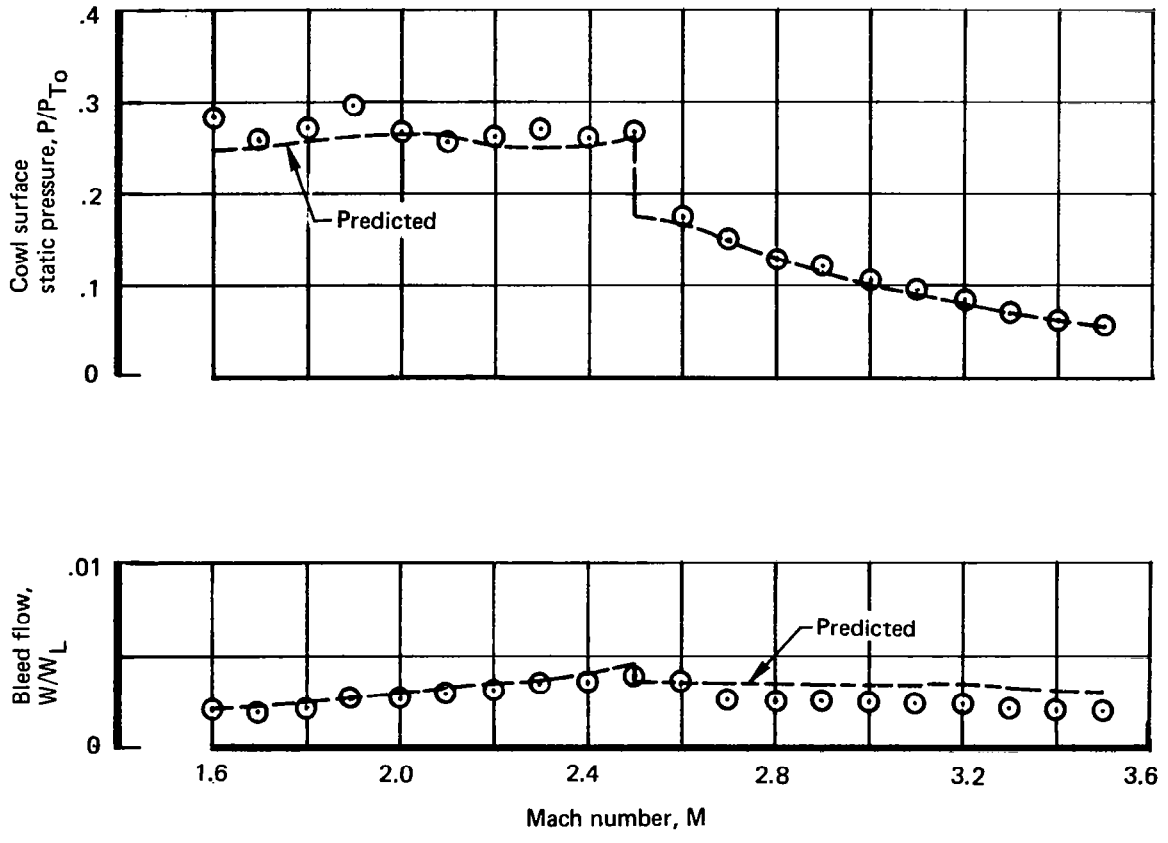

Figure 24.—Bleed Rates and Surface Static Pressures, Cowl Plenum 0

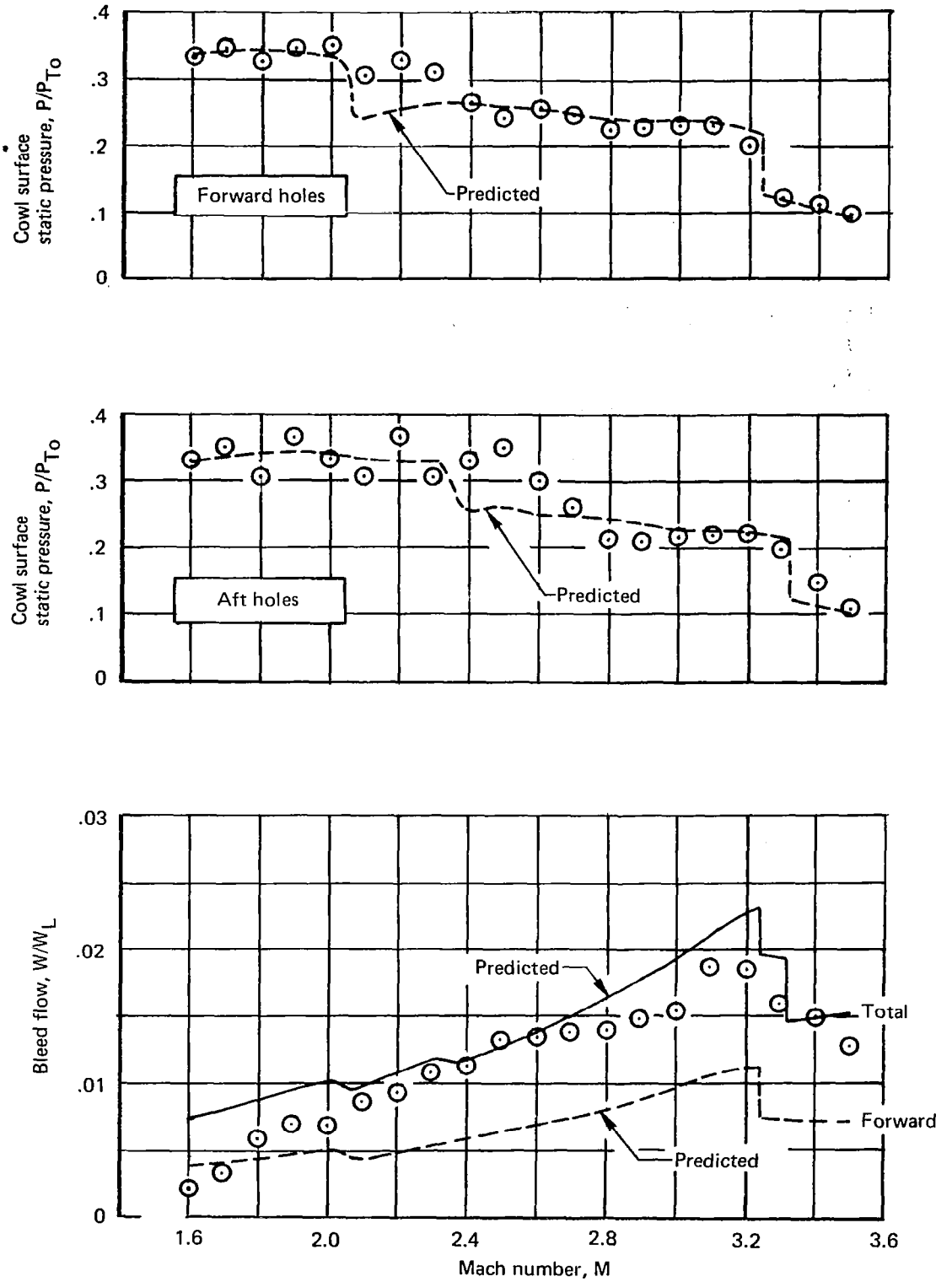

Figure 25.—Bleed Rates and Surface Static Pressures, Cowl Plenum 1

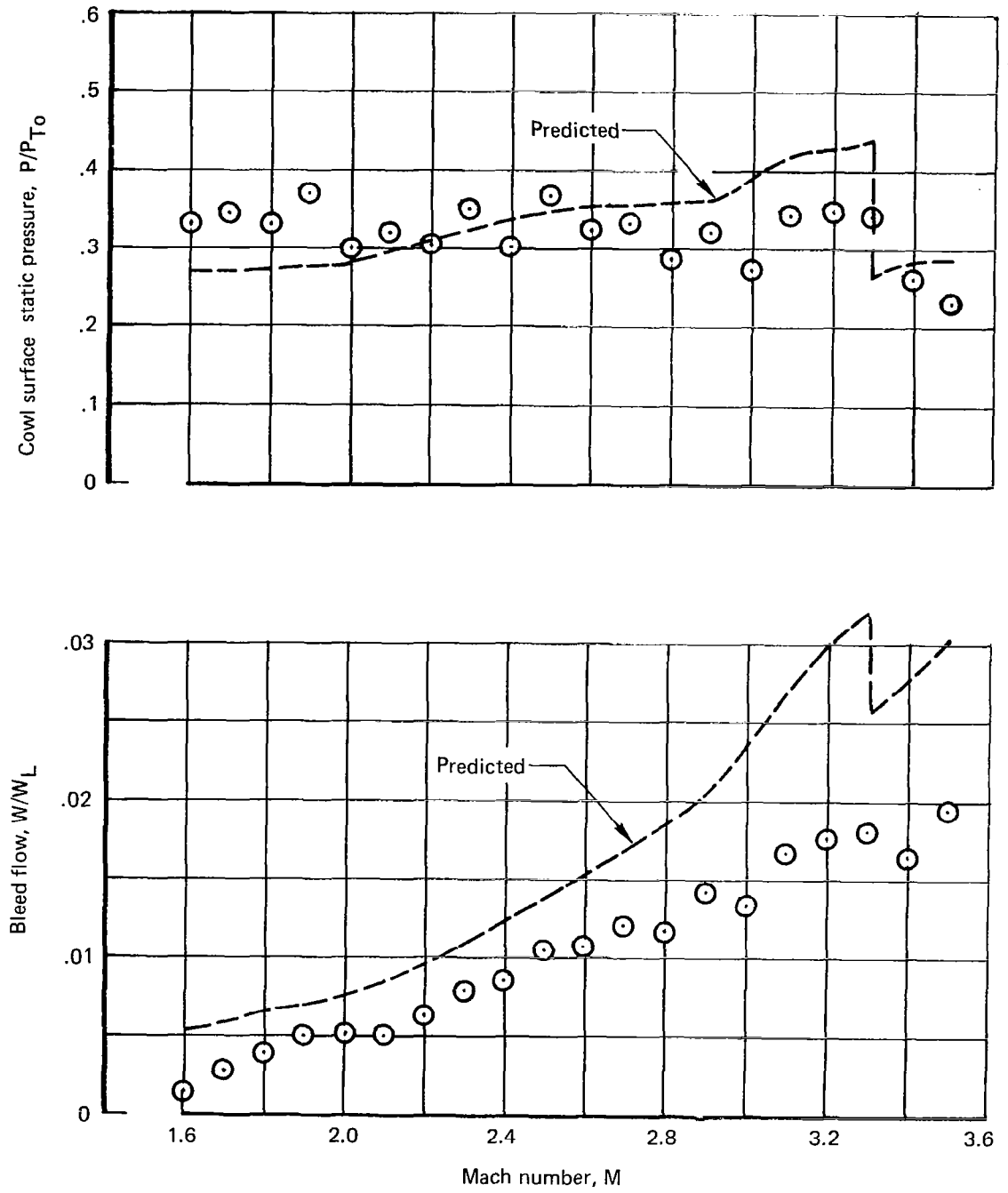

Figure 26.—Bleed Rates and Surface Static Pressures, Cowl Plenum 2

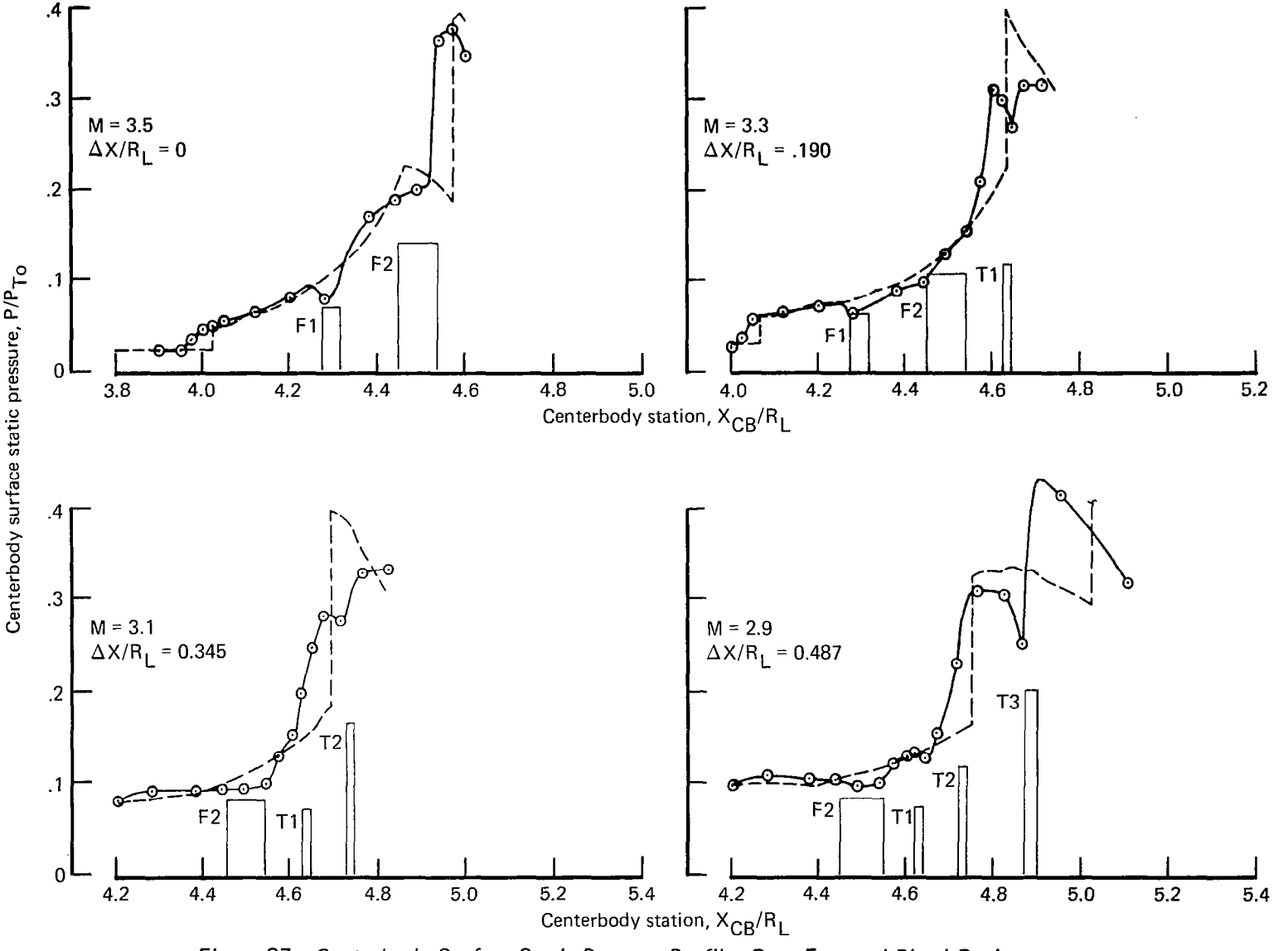

Figure 27.—Centerbody Surface Static-Pressure Profiles Over Forward Bleed Regions

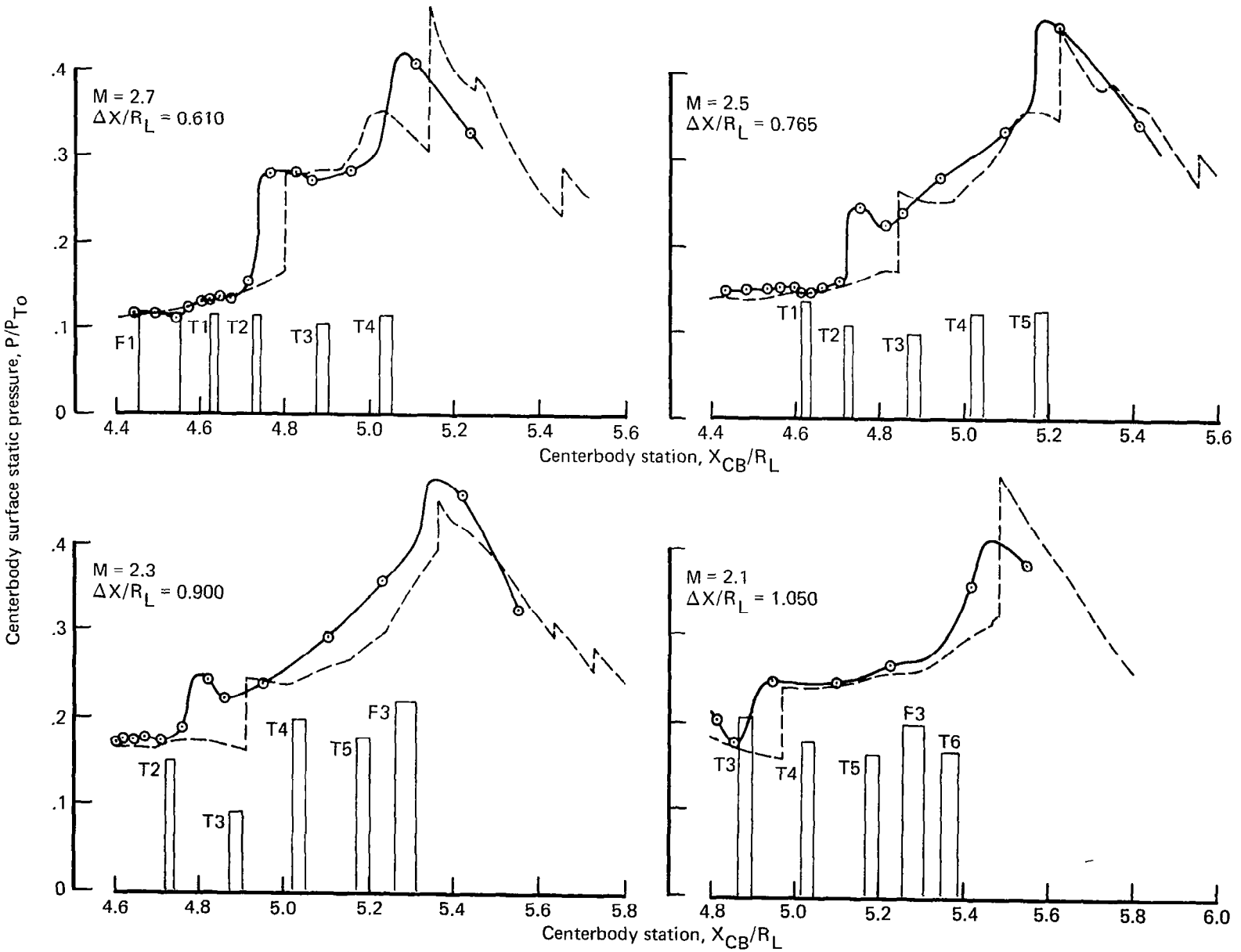

Figure 27.—(Continued)

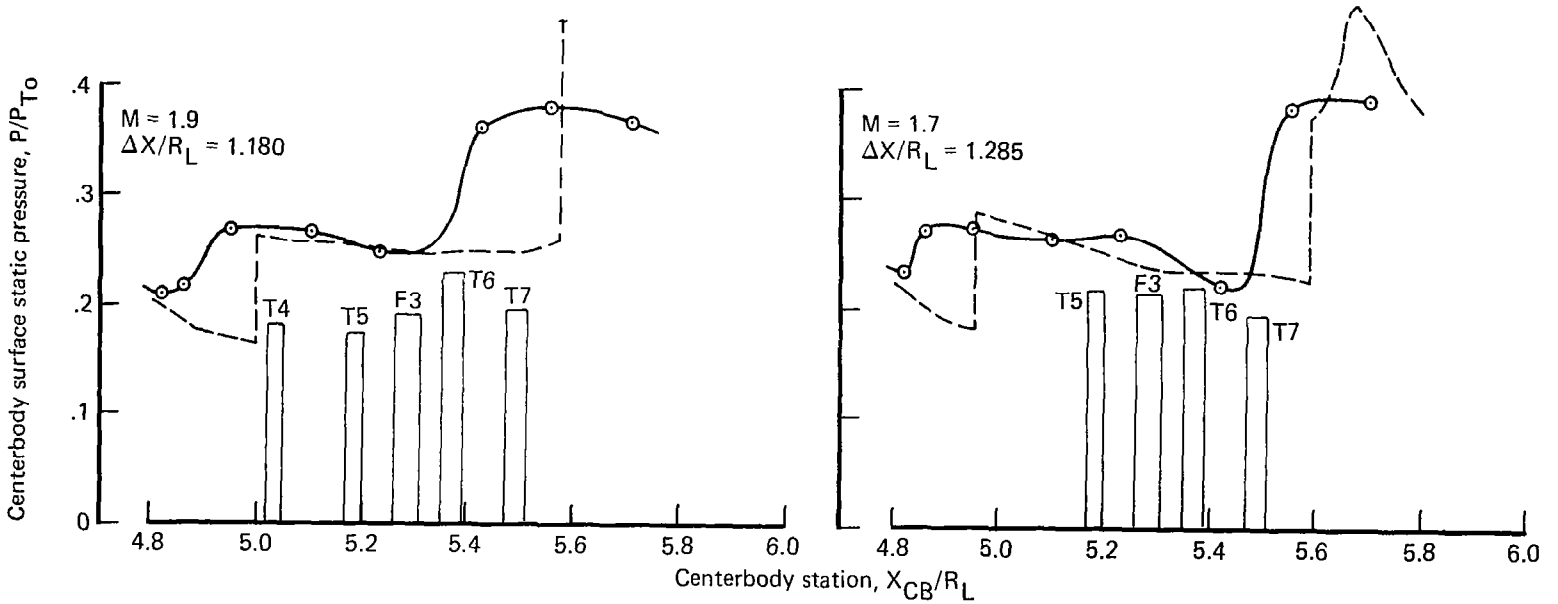

Figure 27.—(Concluded)

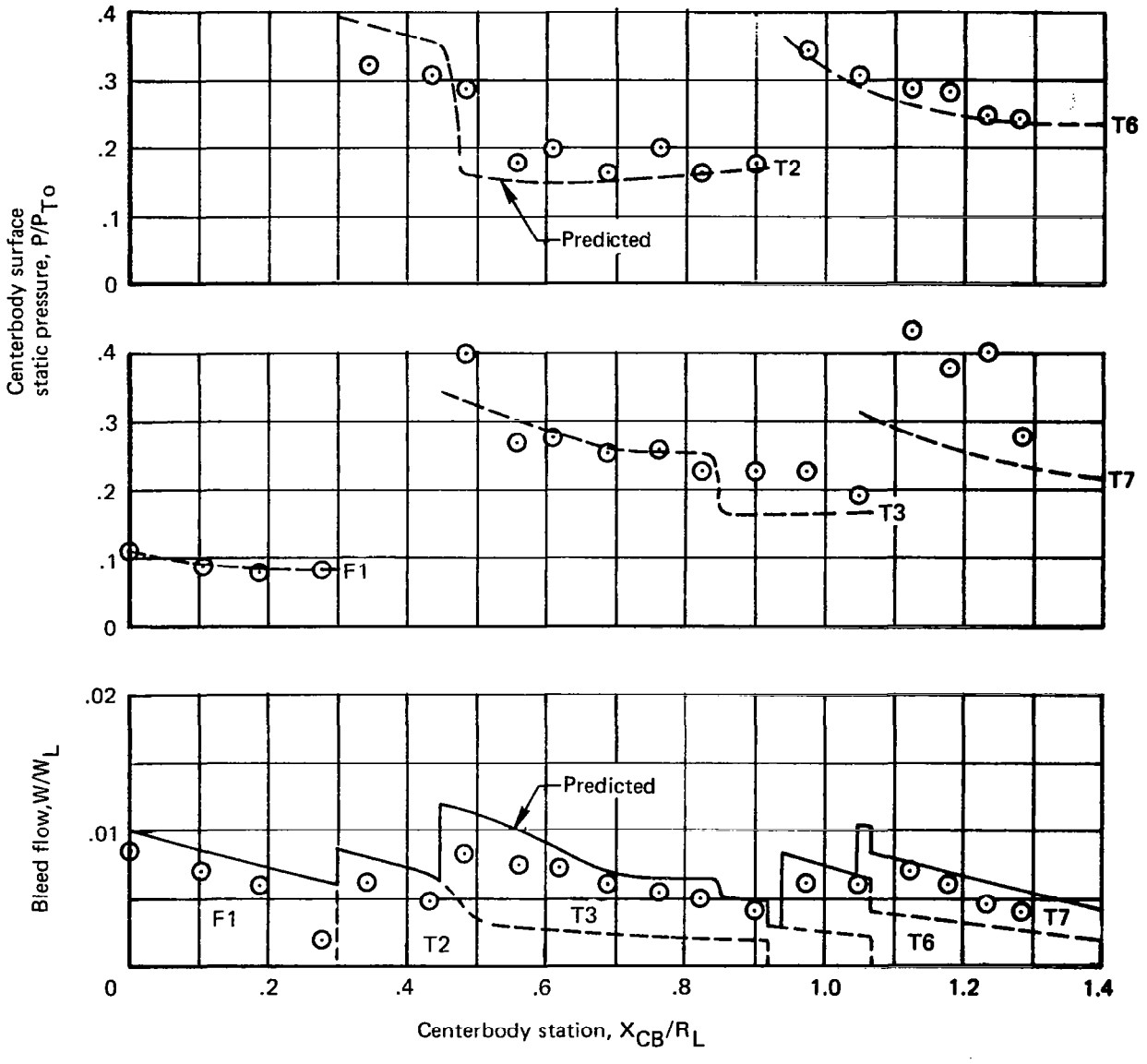

Figure 28.—Bleed Rates and Surface Static Pressures, ***Support-Tube Duct D1***

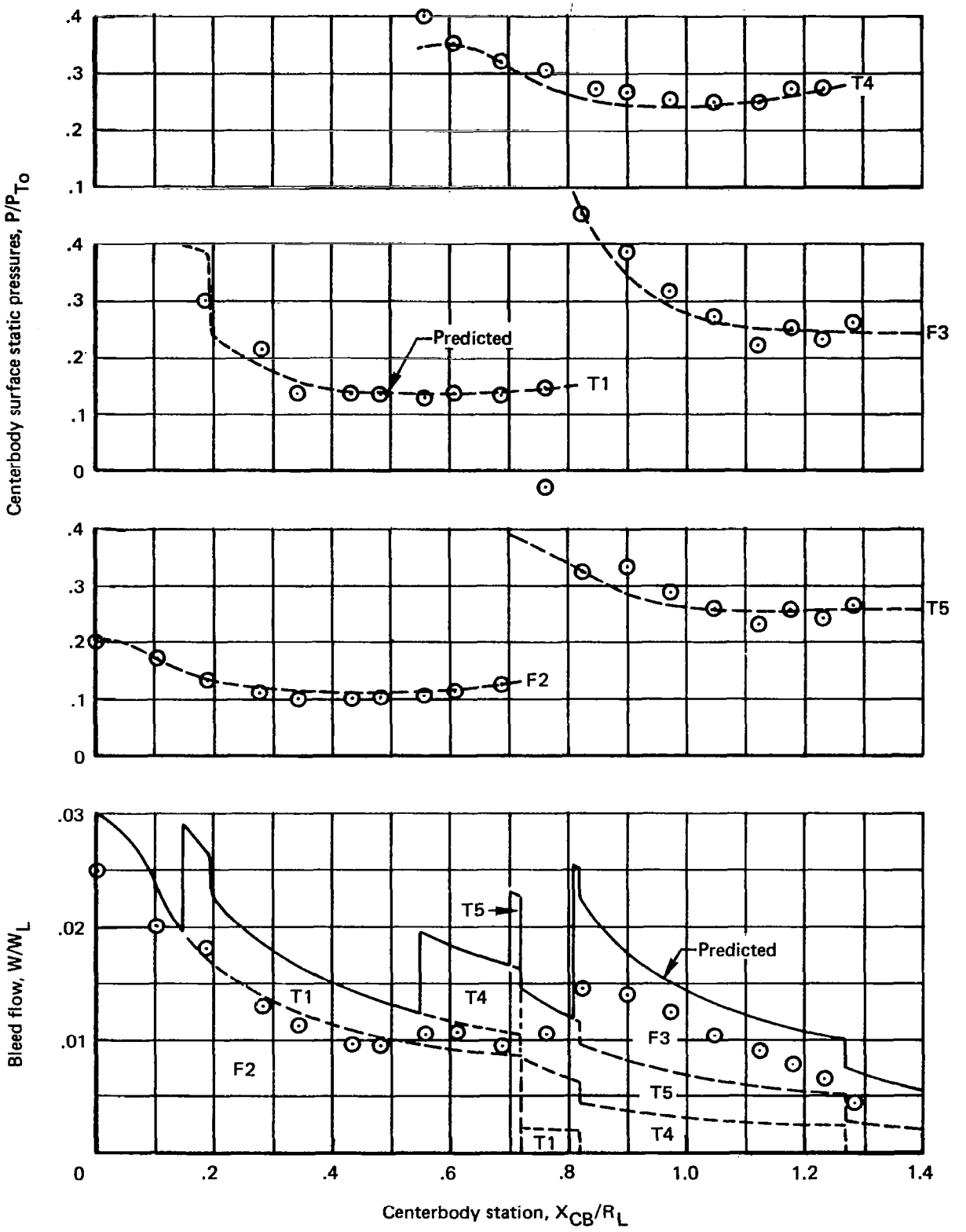

Figure 29.—Bleed Rates and Surface Static Pressures, Support-Tube Duct D2

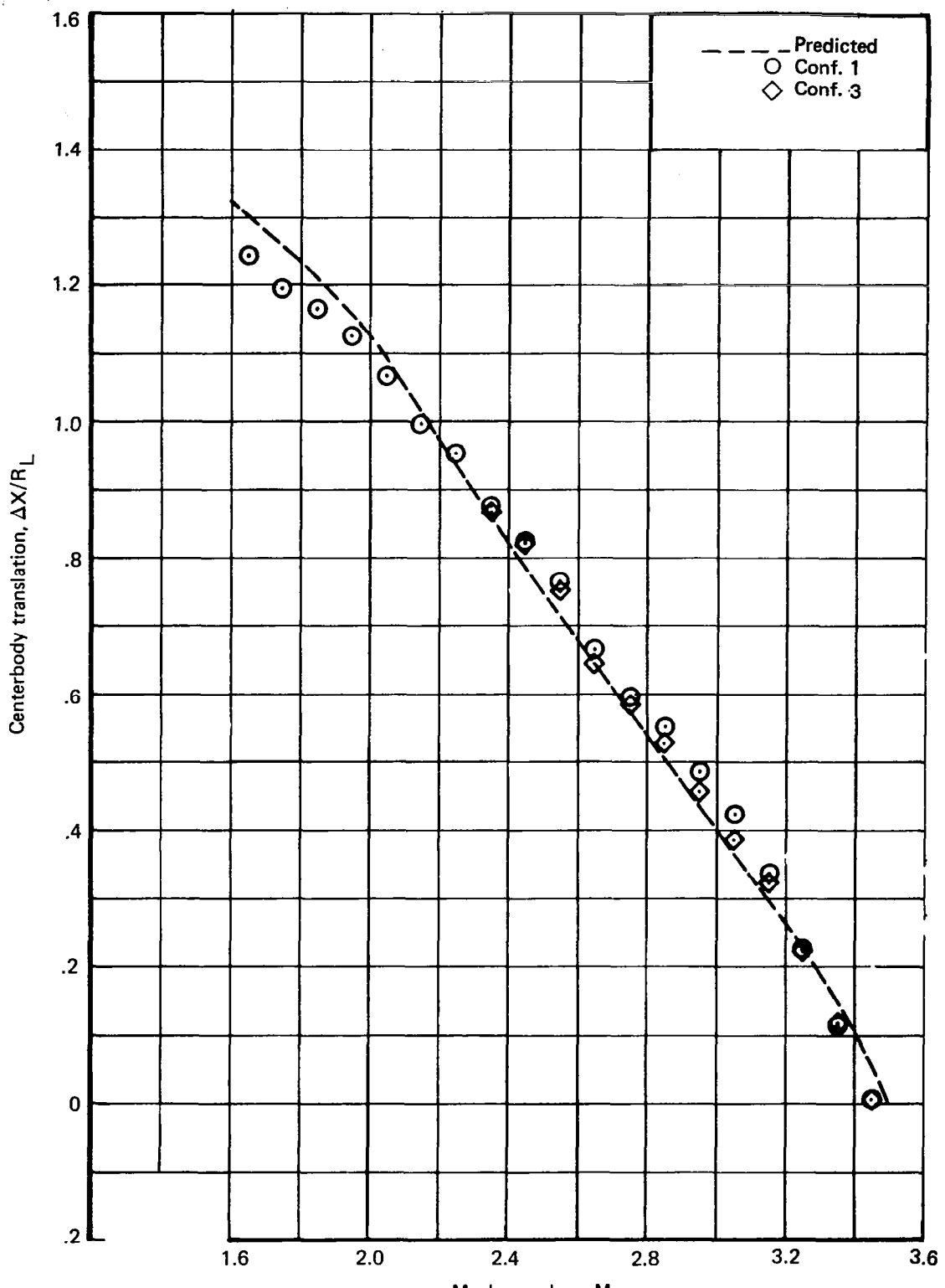

Figure 30.—Centerbody Translation Schedule

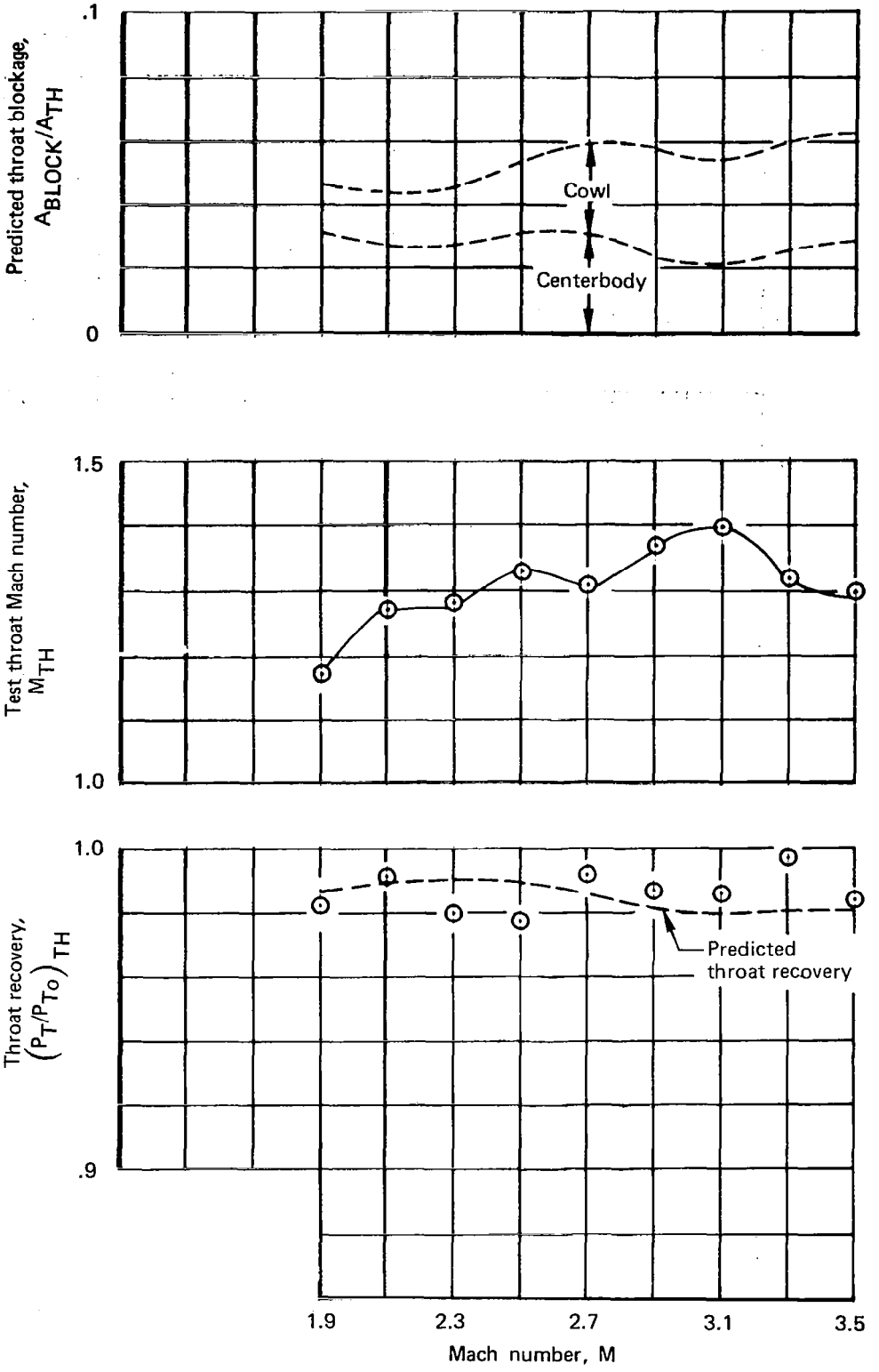

Figure 31.—Supersonic Diffuser Efficiency

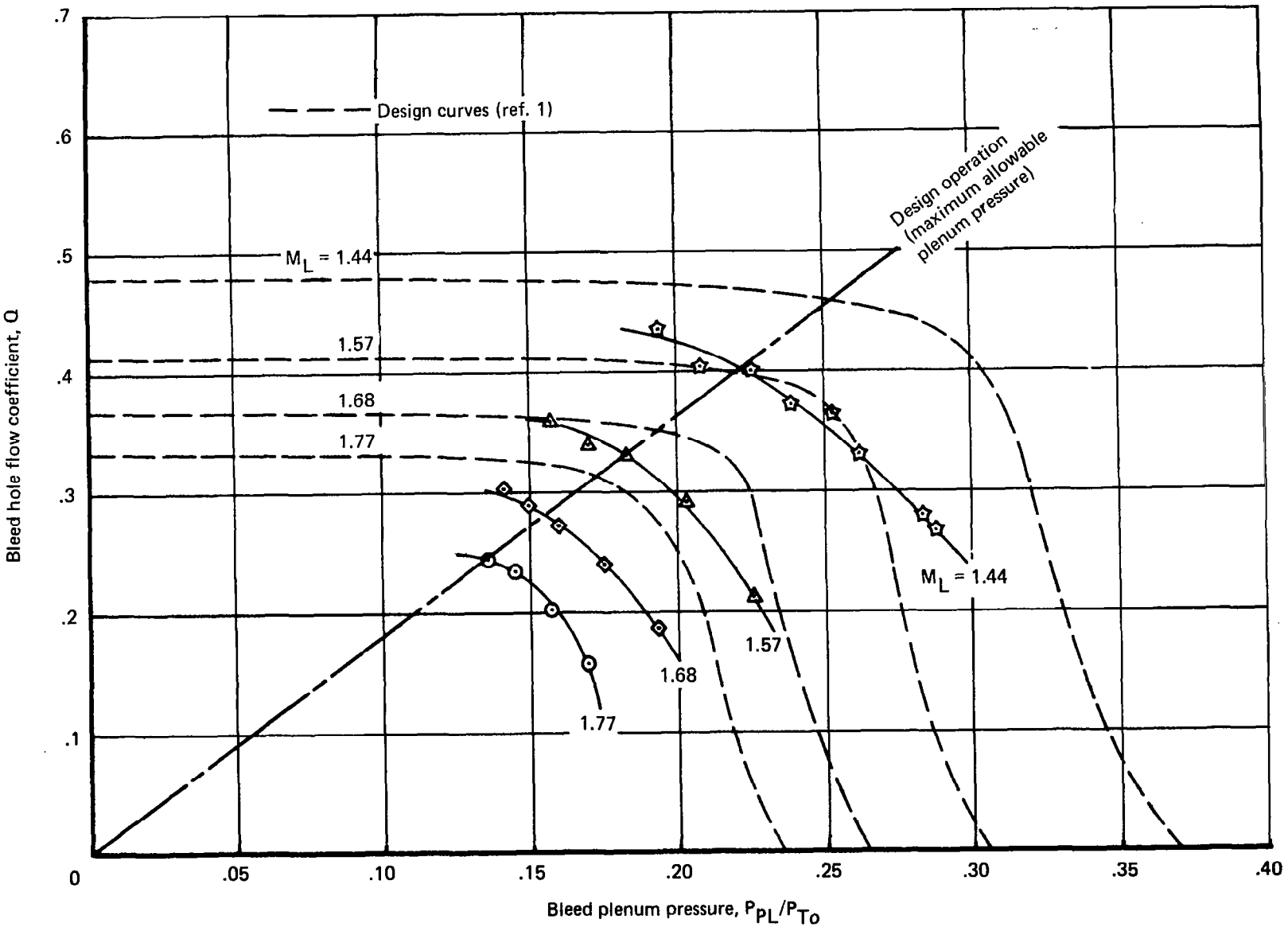

Figure 32.—Bleed Hole Flow Coefficients

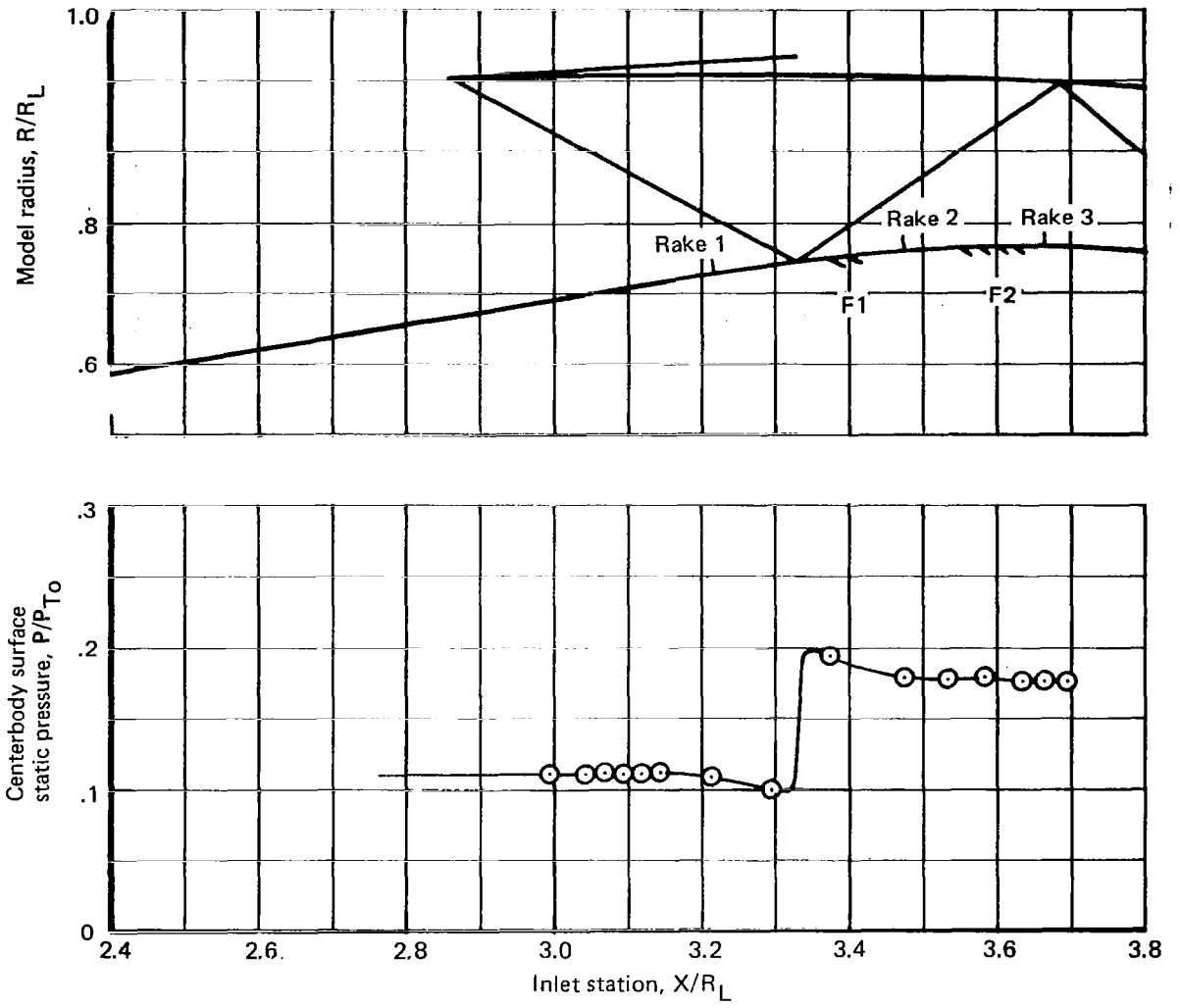

	Rake 1		Rake 2		Rake 3	
	H_i	δ^*(mm)	H_i	δ^*(mm)	H_i	δ^*(mm)
Rough holes	—	—	1.47	1.98	1.43	1.98
Smooth surface	1.28	1.35	1.44	2.00	1.38	1.98
Predicted	1.32	1.93	1.44	2.05	1.38	2.10

Figure 33.—Bleed Hole Roughness Effects, M = 2.3

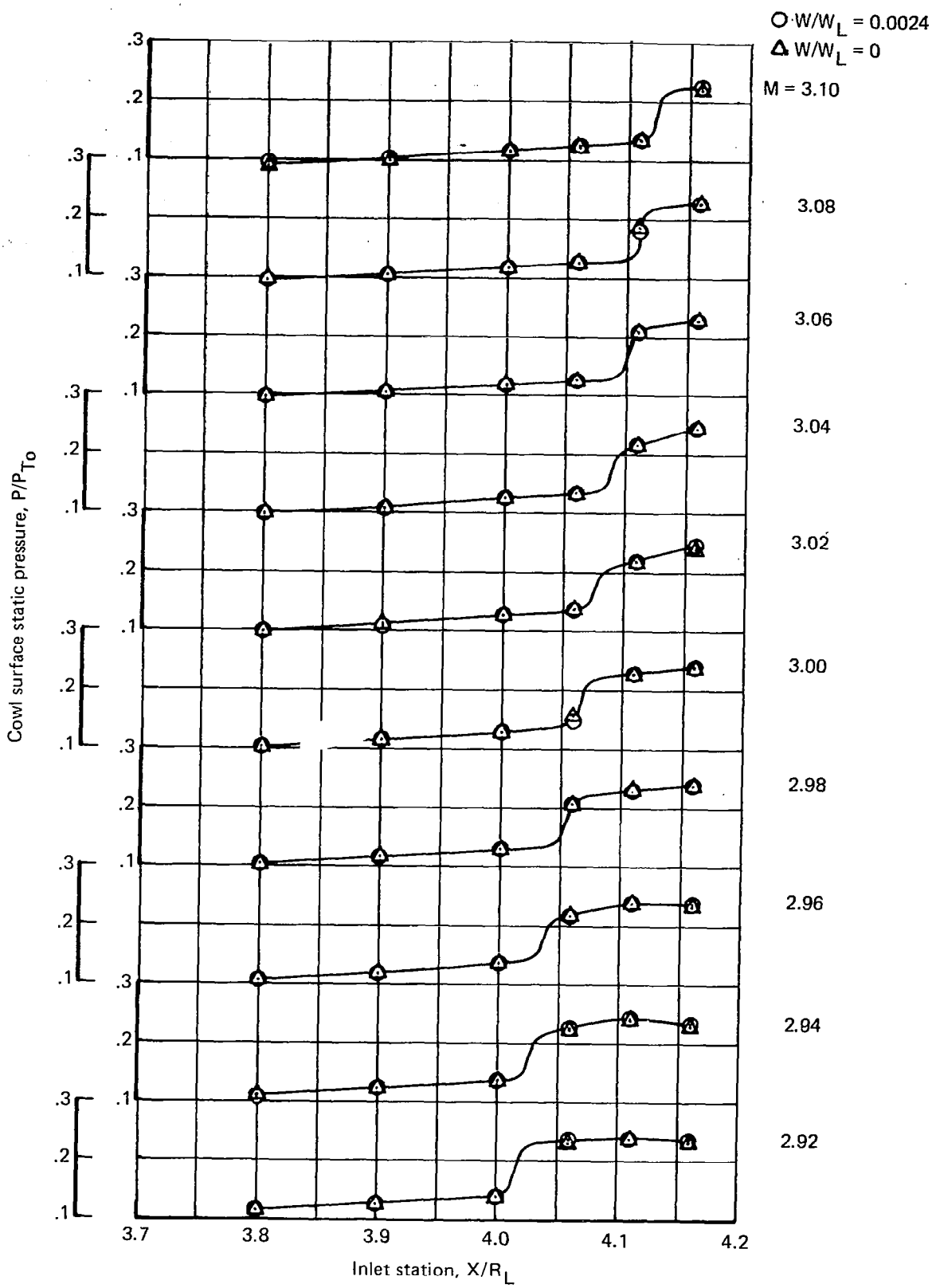

Figure 34.—Effects of Cowl Plenum 0 on Local Surface Static Pressure

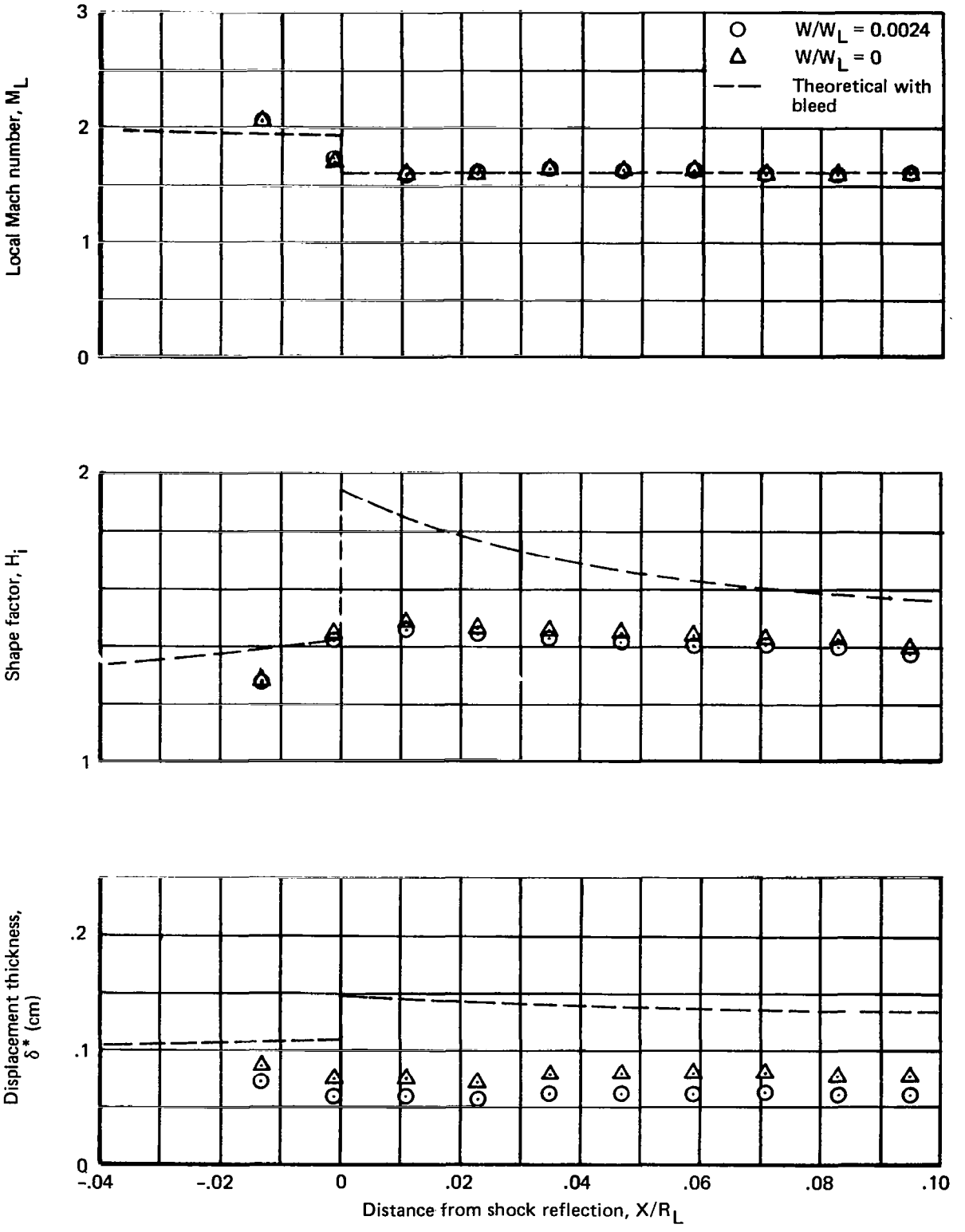

Figure 35.—Effects of Cowl Plenum 0 on Local Boundary-Layer Development

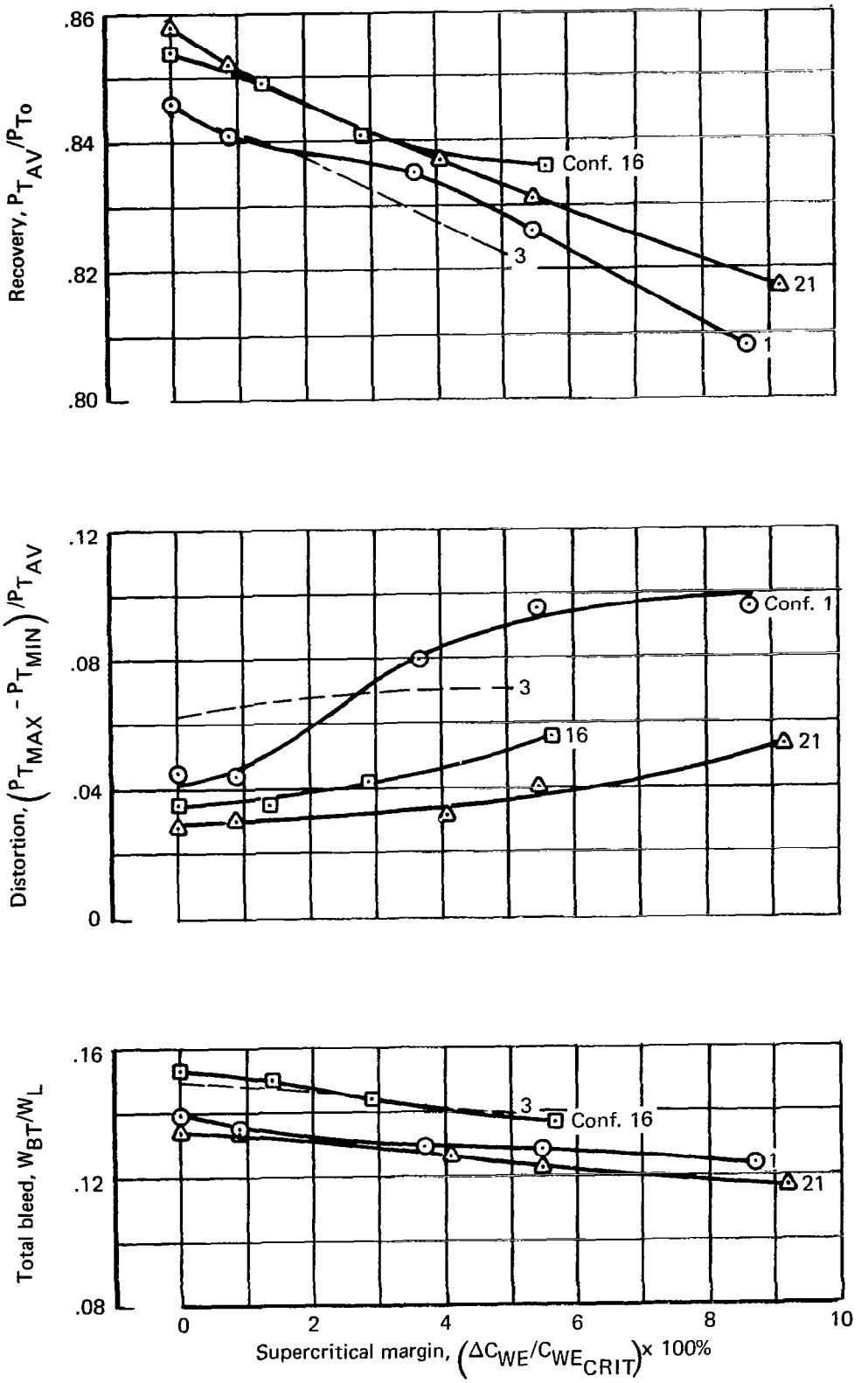

Figure 36.—Inlet Performance, M = 3.5

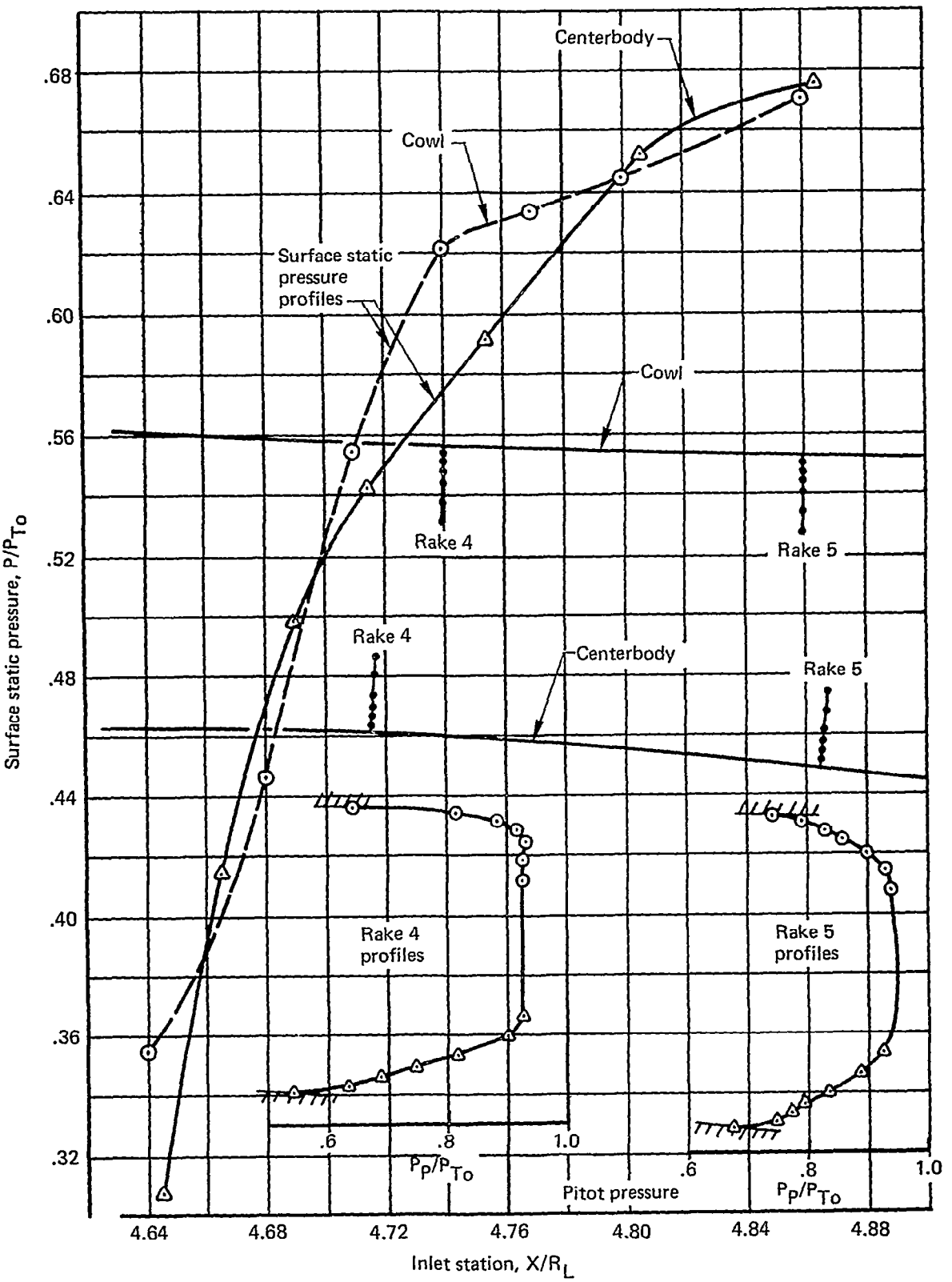

Figure 37.—Inlet Throat Profiles, Configuration 21, M = 3.5

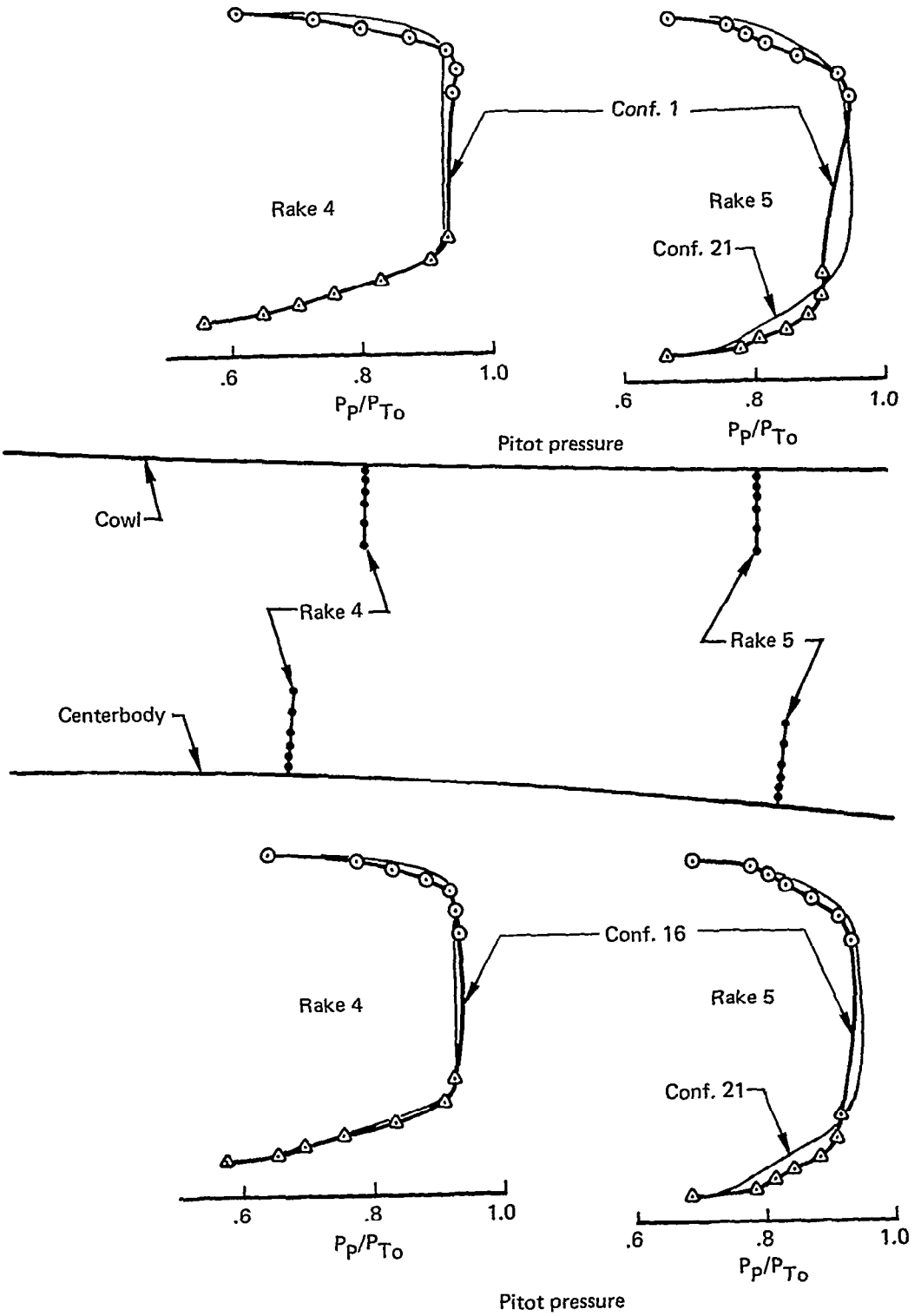

Figure 38.—Throat Pitot Profiles, M = 3.5

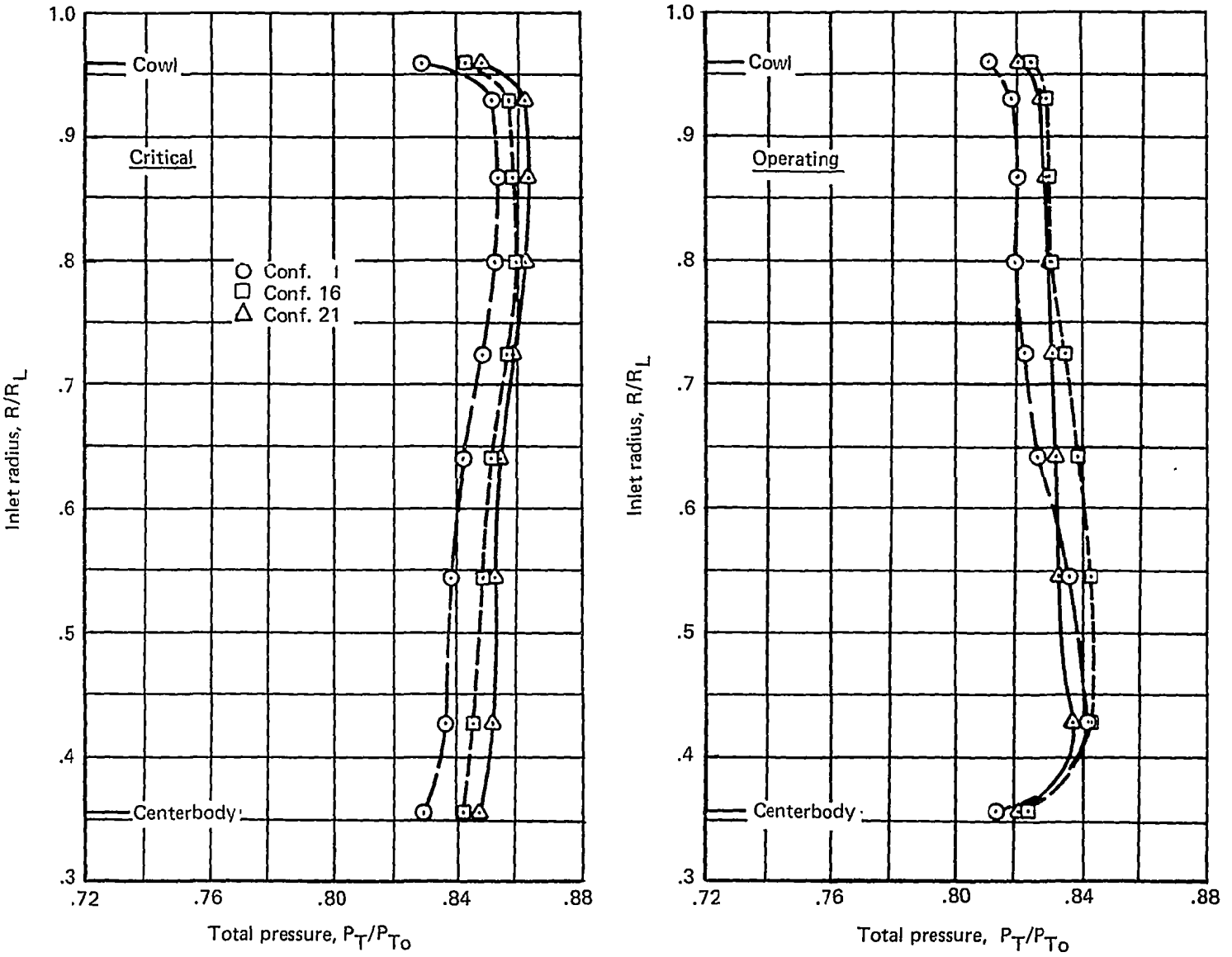

Figure 39.—Compressor Face Total-Pressure Profiles, M = 3.5

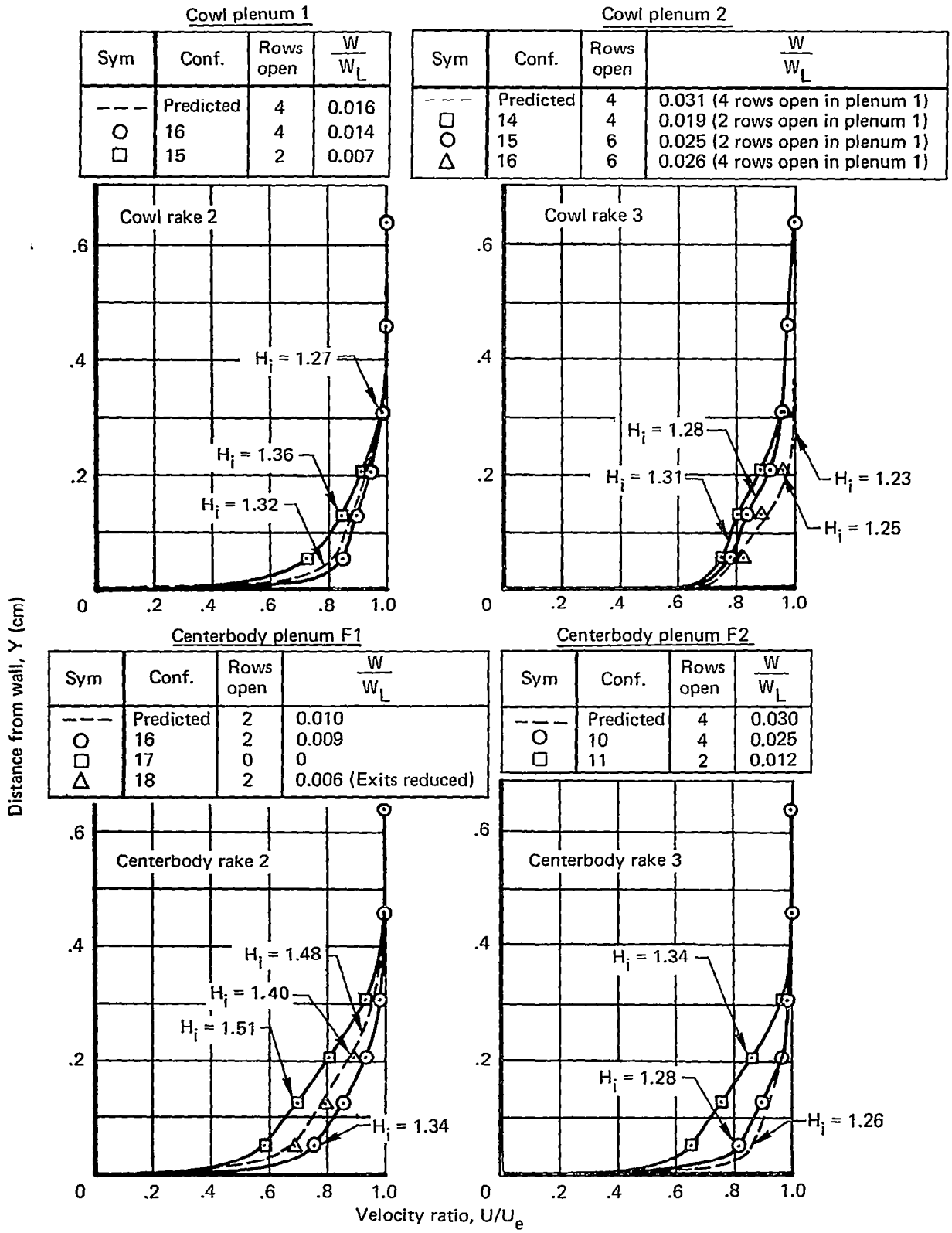

Figure 40.—Effects of Bleed Changes on Boundary-Layer Velocity Profiles, M = 3.5

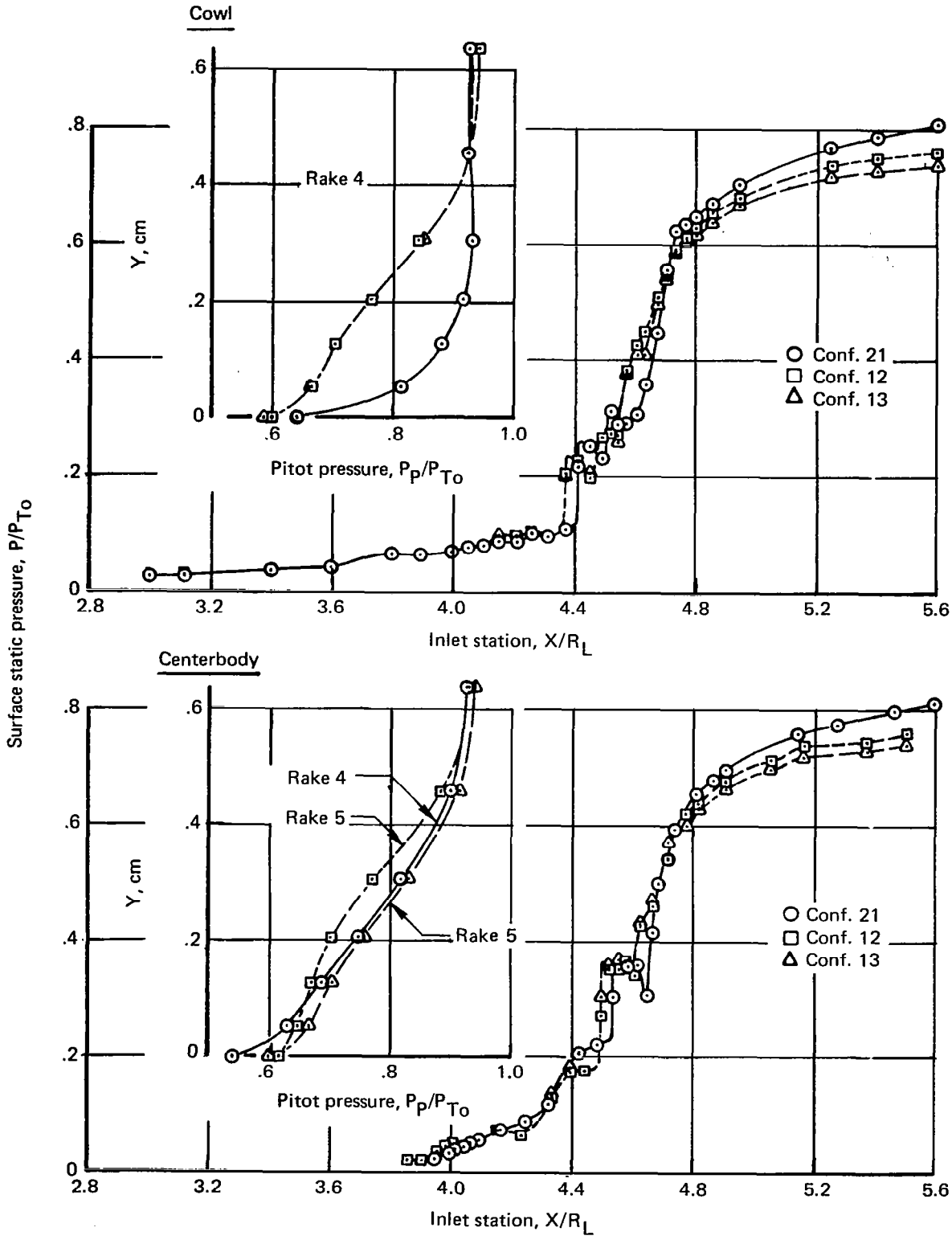

Figure 41.—Inlet Static-Pressure Profiles, M = 3.5

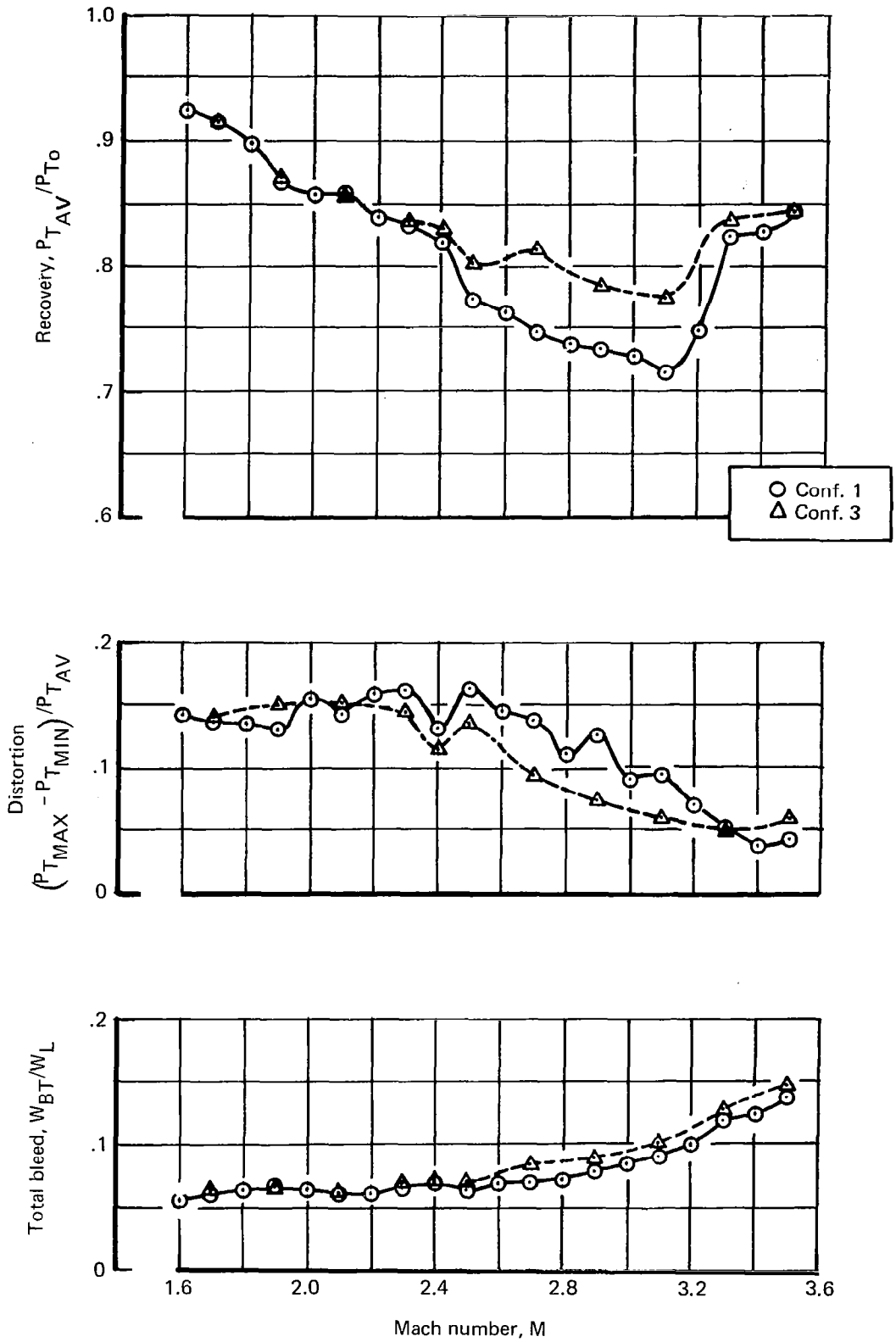

Figure 42.—Off-Design Engine-Face Performance

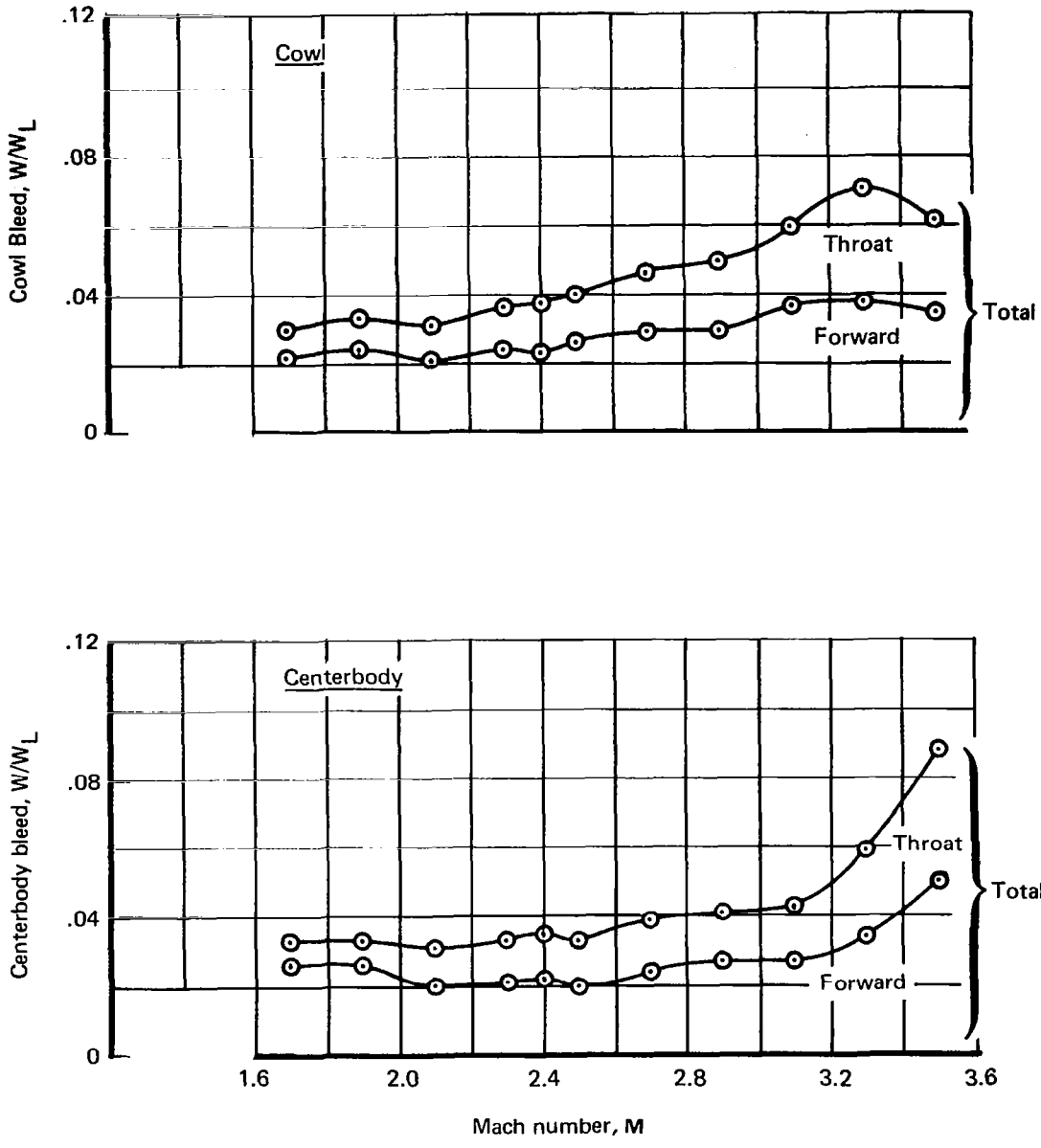

Figure 43.—Off-Design Bleed Rates, Configuration 3, $\alpha = 0°$

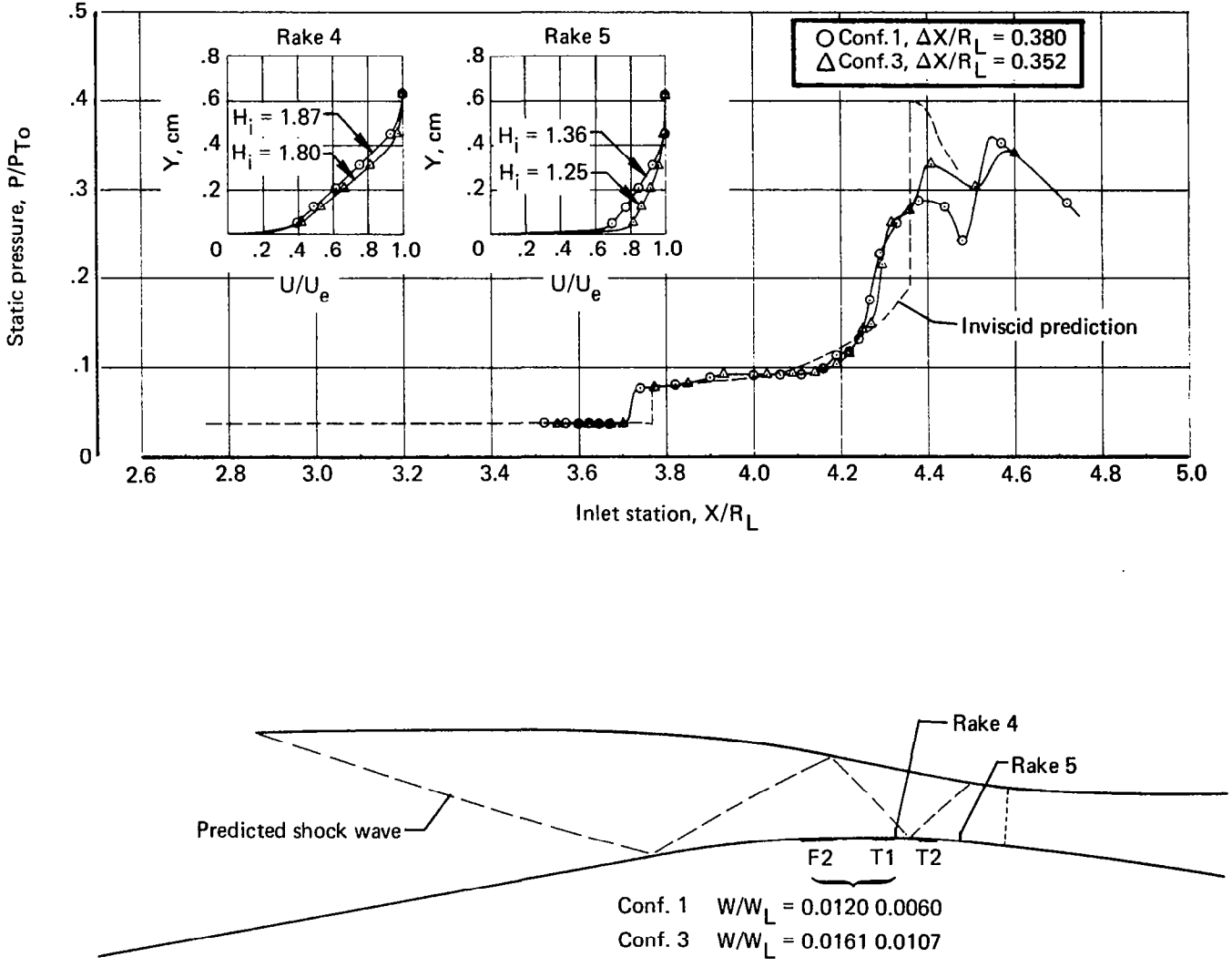

Figure 44.—Centerbody Static-Pressure Distributions and Boundary-Layer Profiles, M = 3.1, Configurations 1 and 3

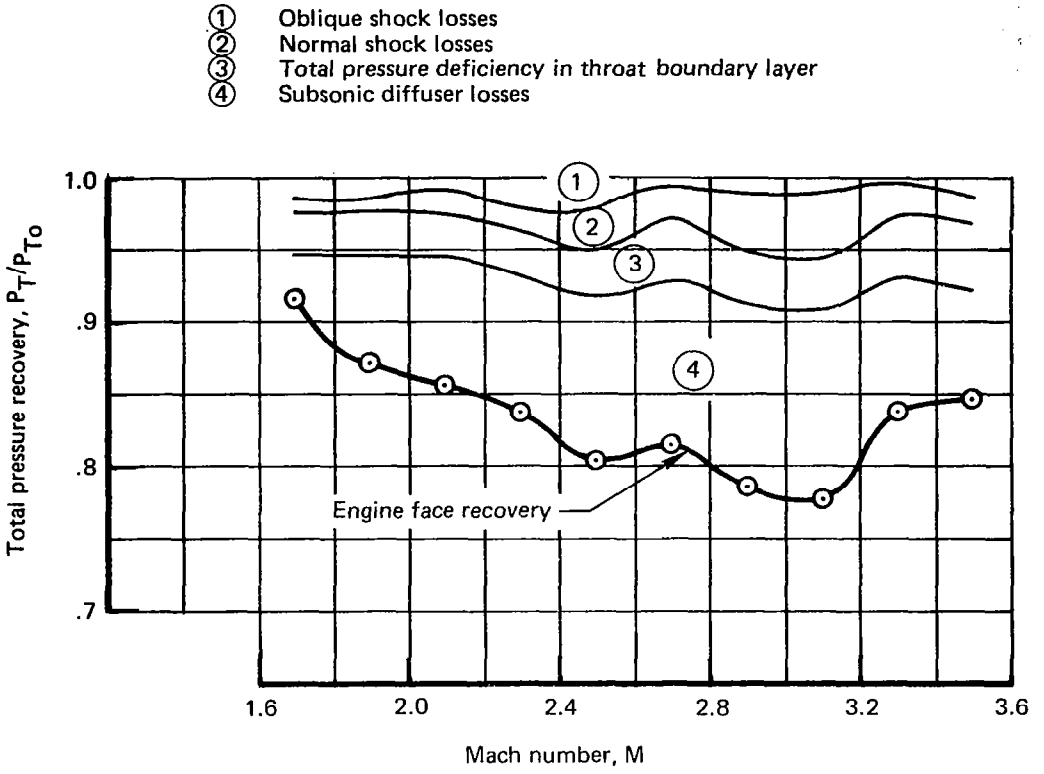

Figure 45.—Inlet Total-Pressure Losses

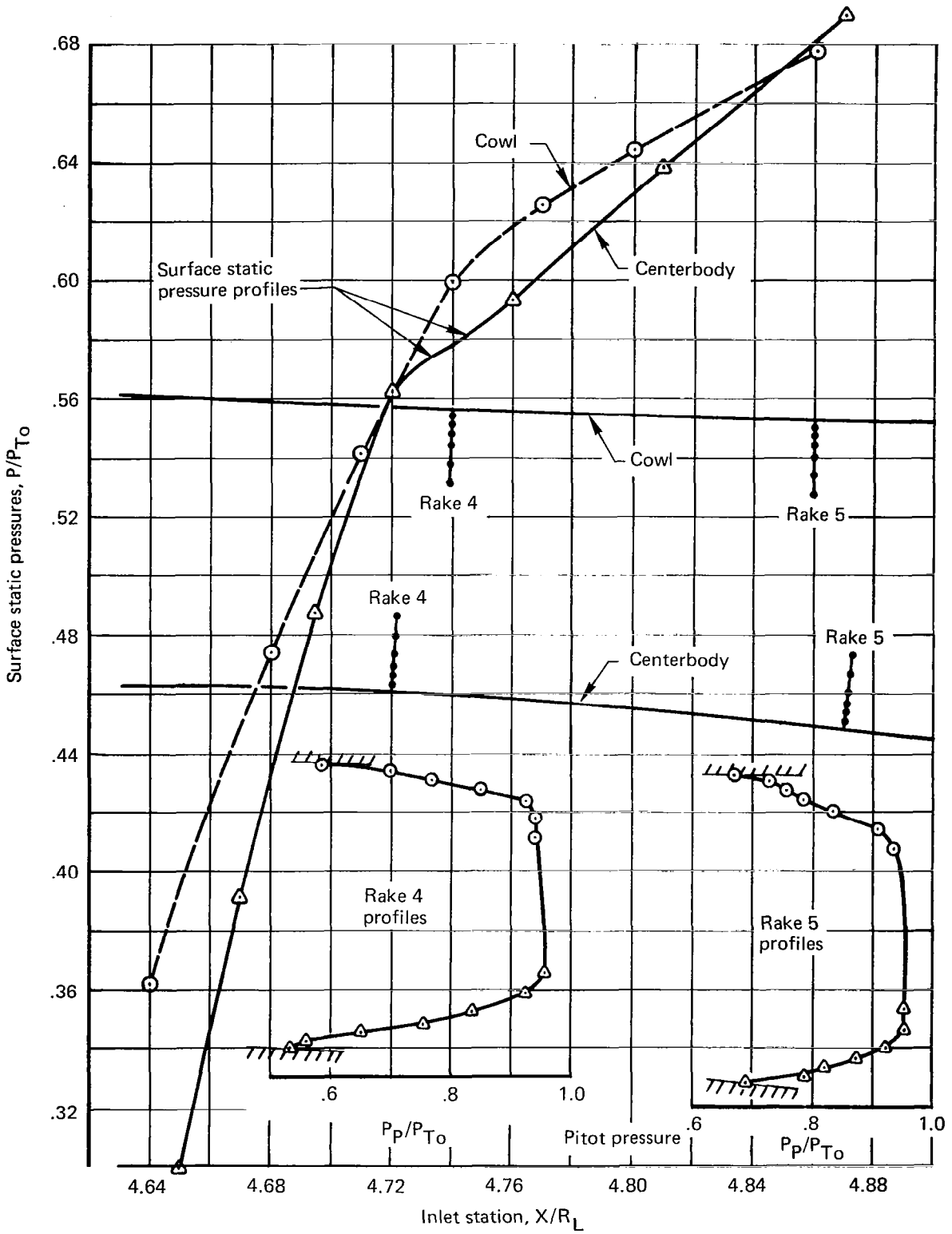

Figure 46.—Inlet Throat Profiles, Configuration 3, M = 3.5

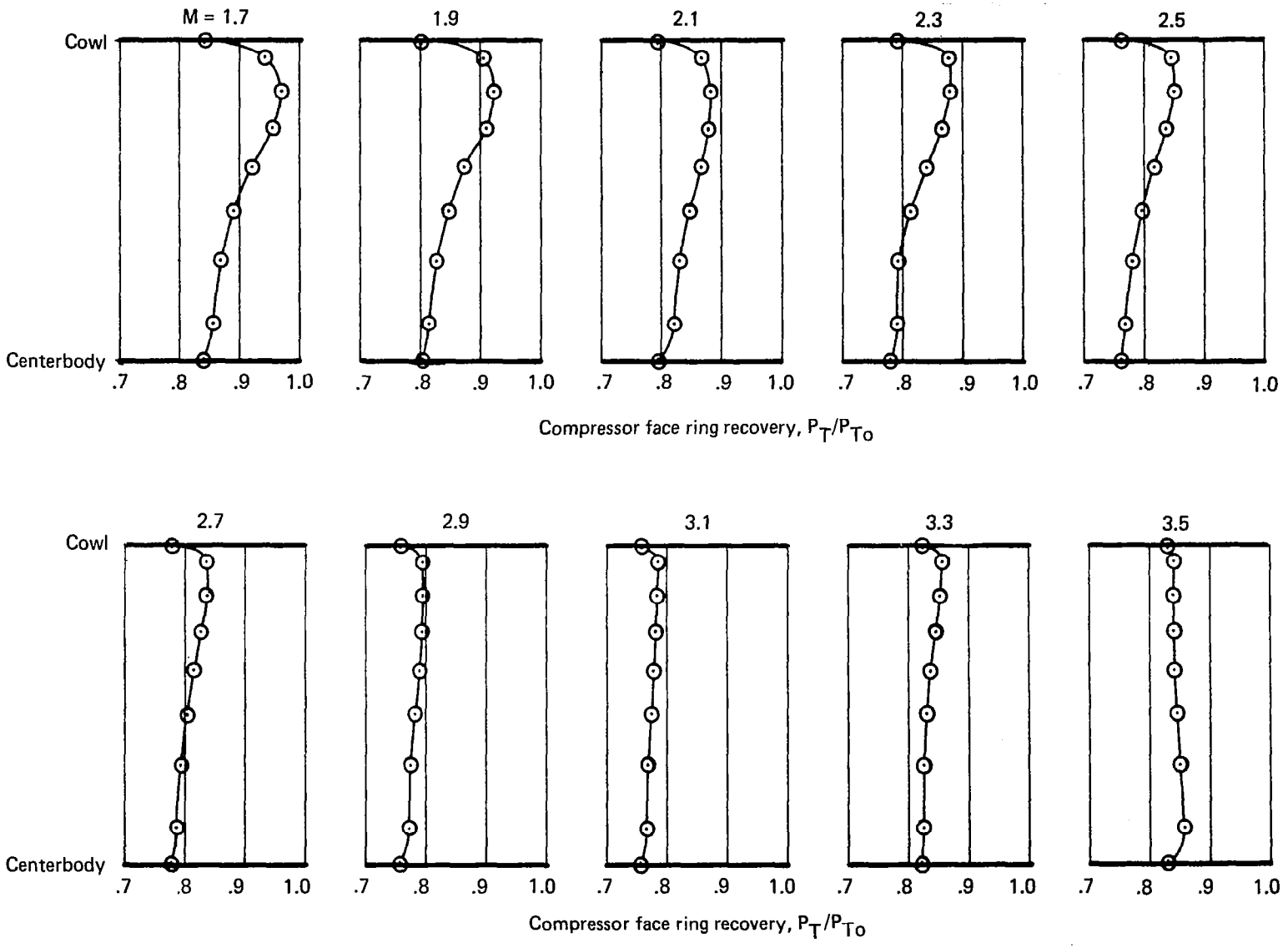

Figure 47.—Off-Design Engine-Face Total-Pressure Profiles, Configuration 3

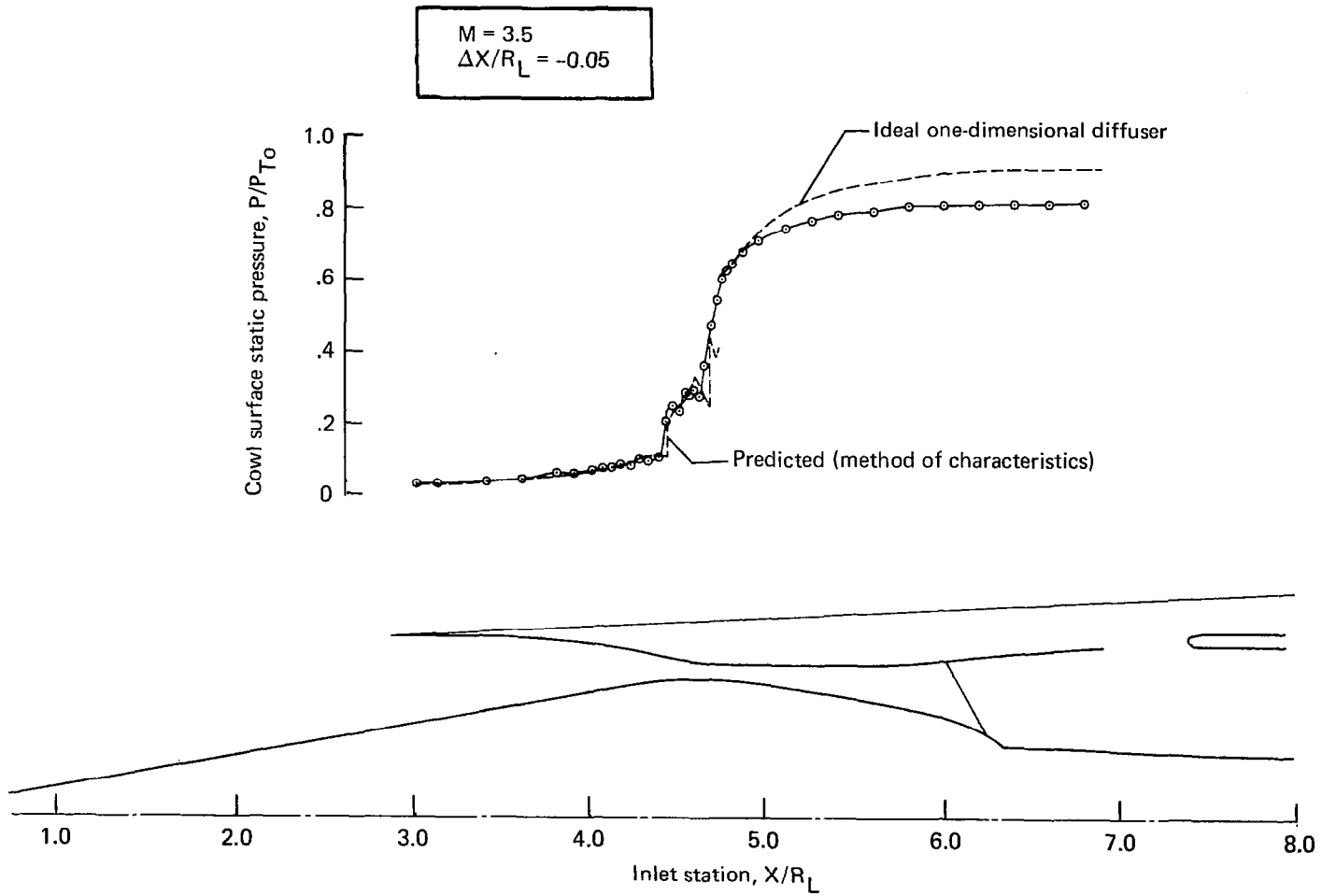

Figure 48.—Cowl Static-Pressure Distributions, M = 3.5, Configuration 3

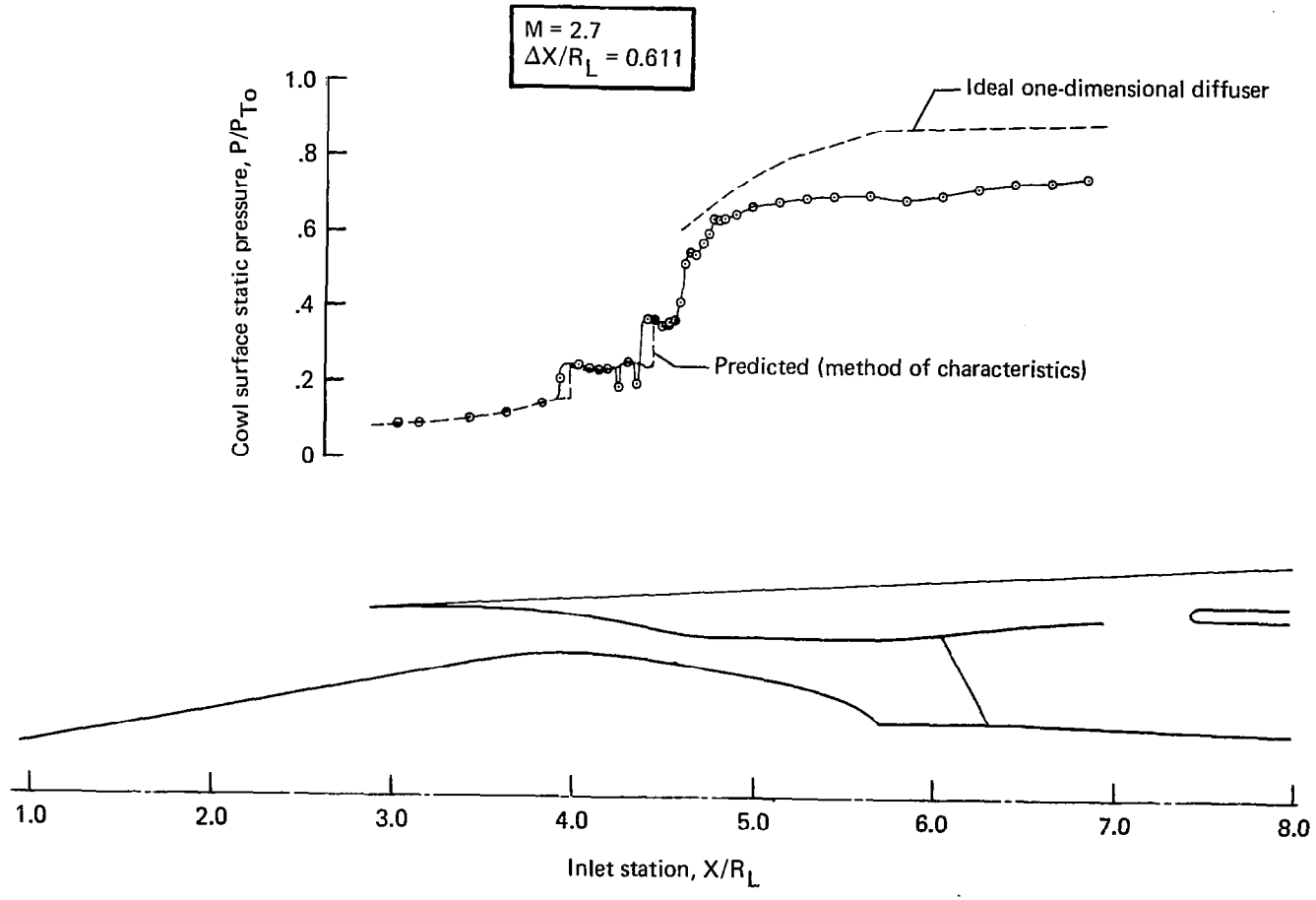

Figure 49.—Cowl Static-Pressure Distributions, M = 2.7, Configuration 3

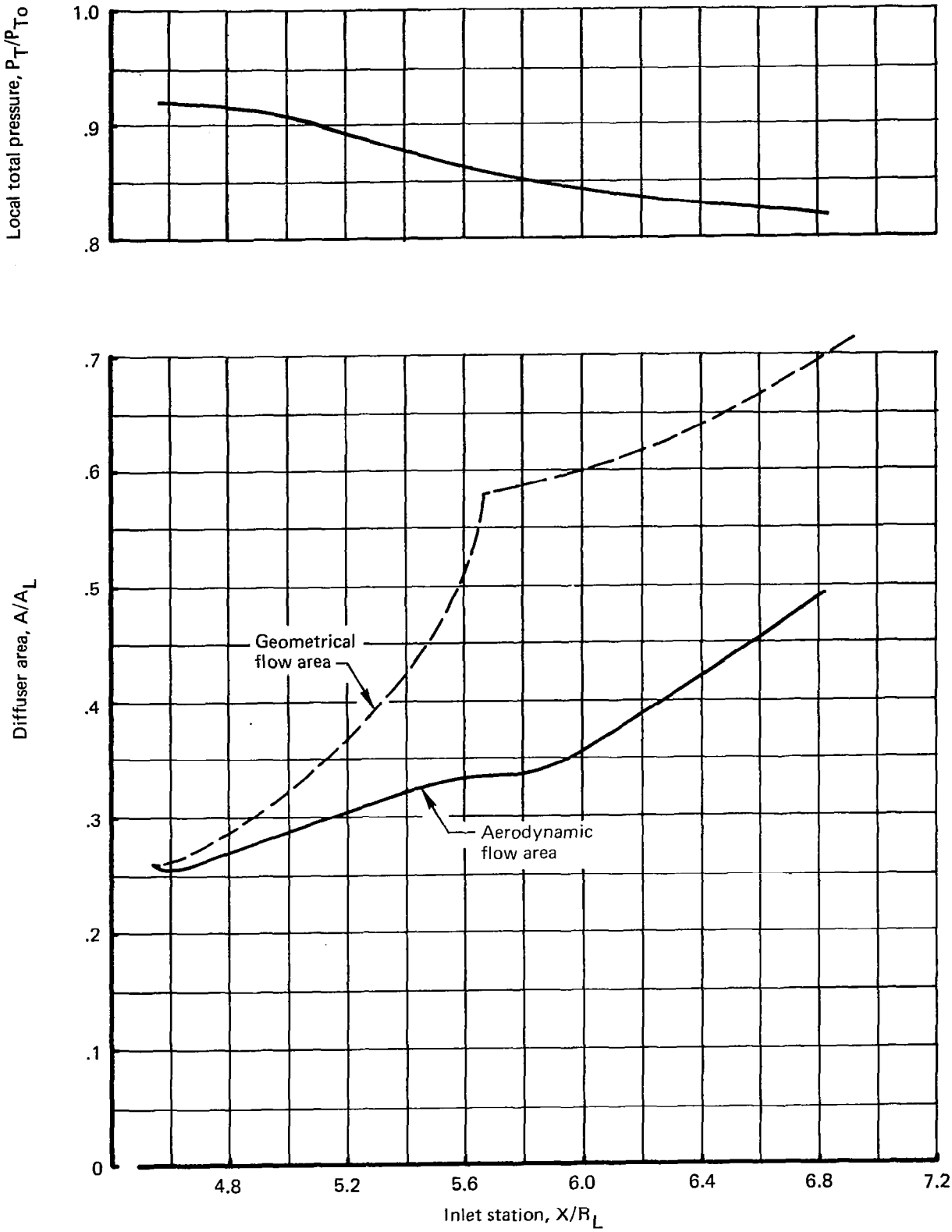

Figure 50.—Subsonic Diffuser Performance, M = 2.7, $\Delta X/R_L$ = 0.611, Configuration 3

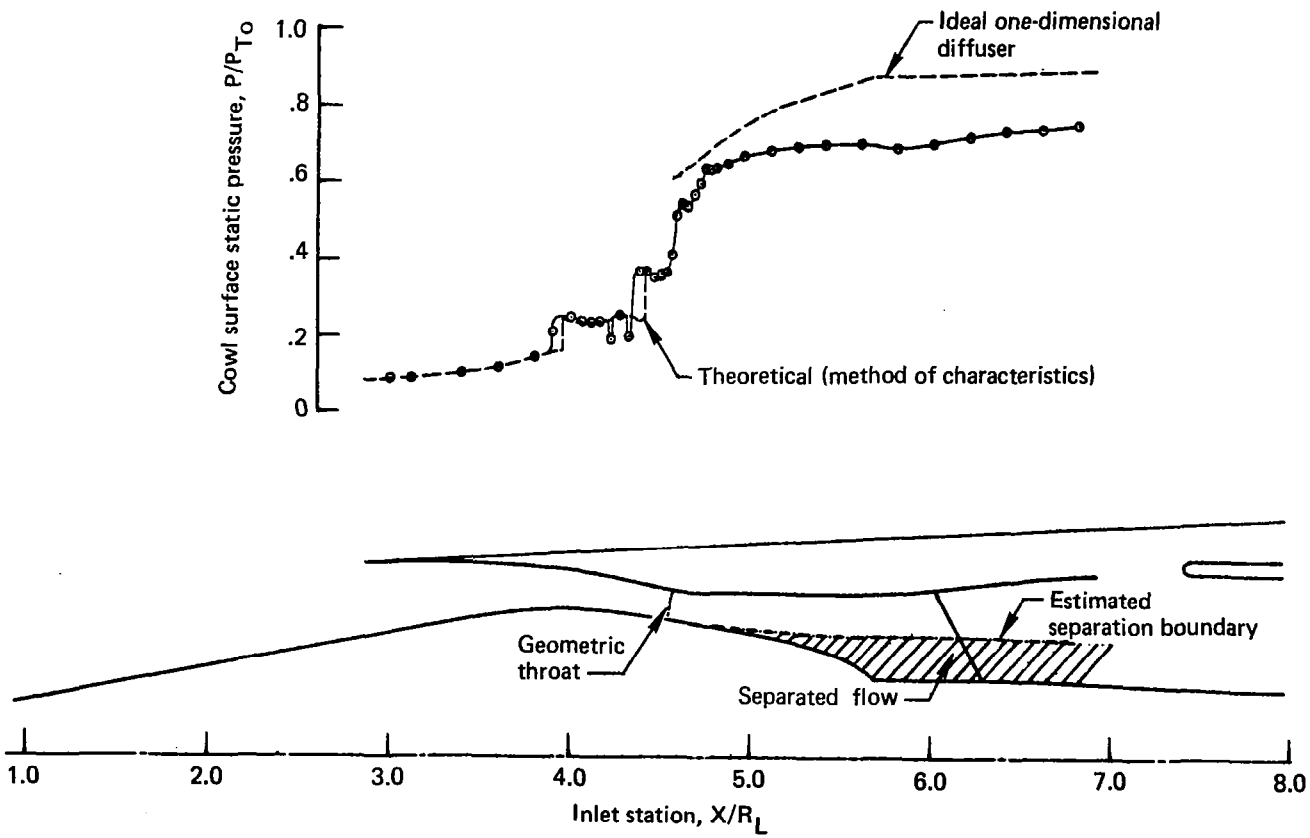

Figure 51.—Estimated Separation Boundary in Subsonic Diffuser, M = 2.7, $\Delta X/R_L$ = 0.611, Configuration 3

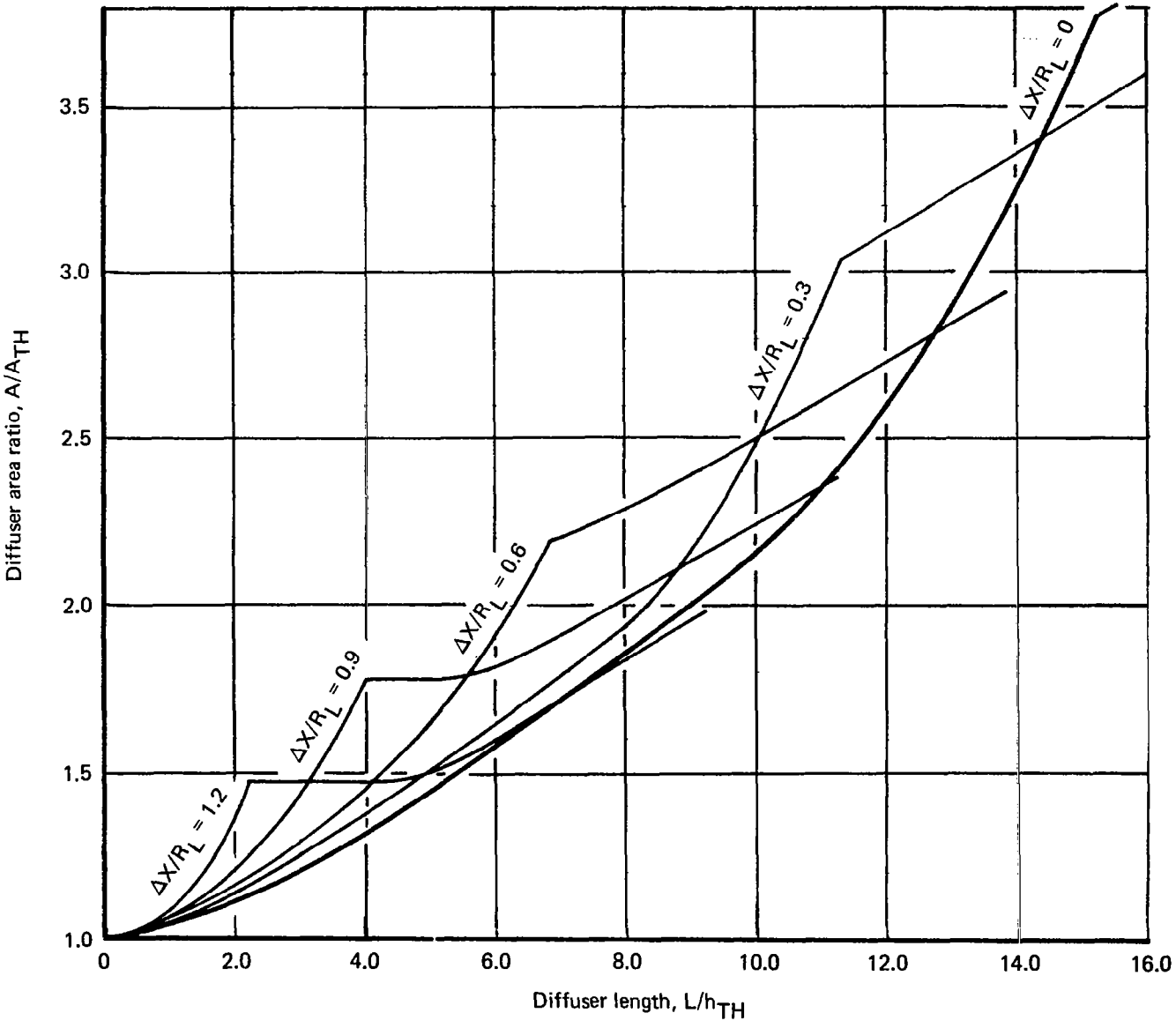

Figure 52.—Initial Area Distribution in Subsonic Diffuser

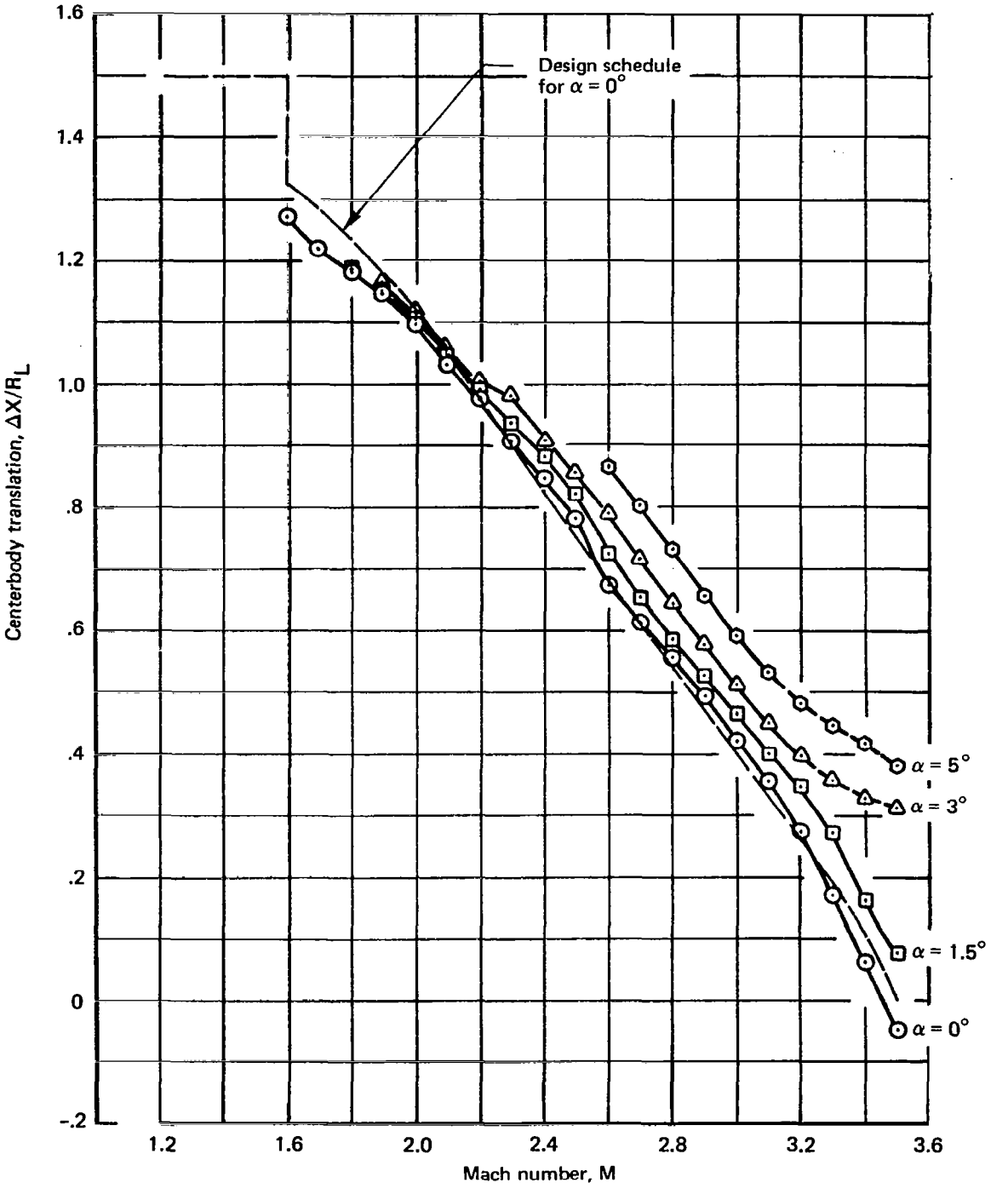

Figure 53.—Operating Centerbody Positions, (ΔM = 0.05), Configuration 3

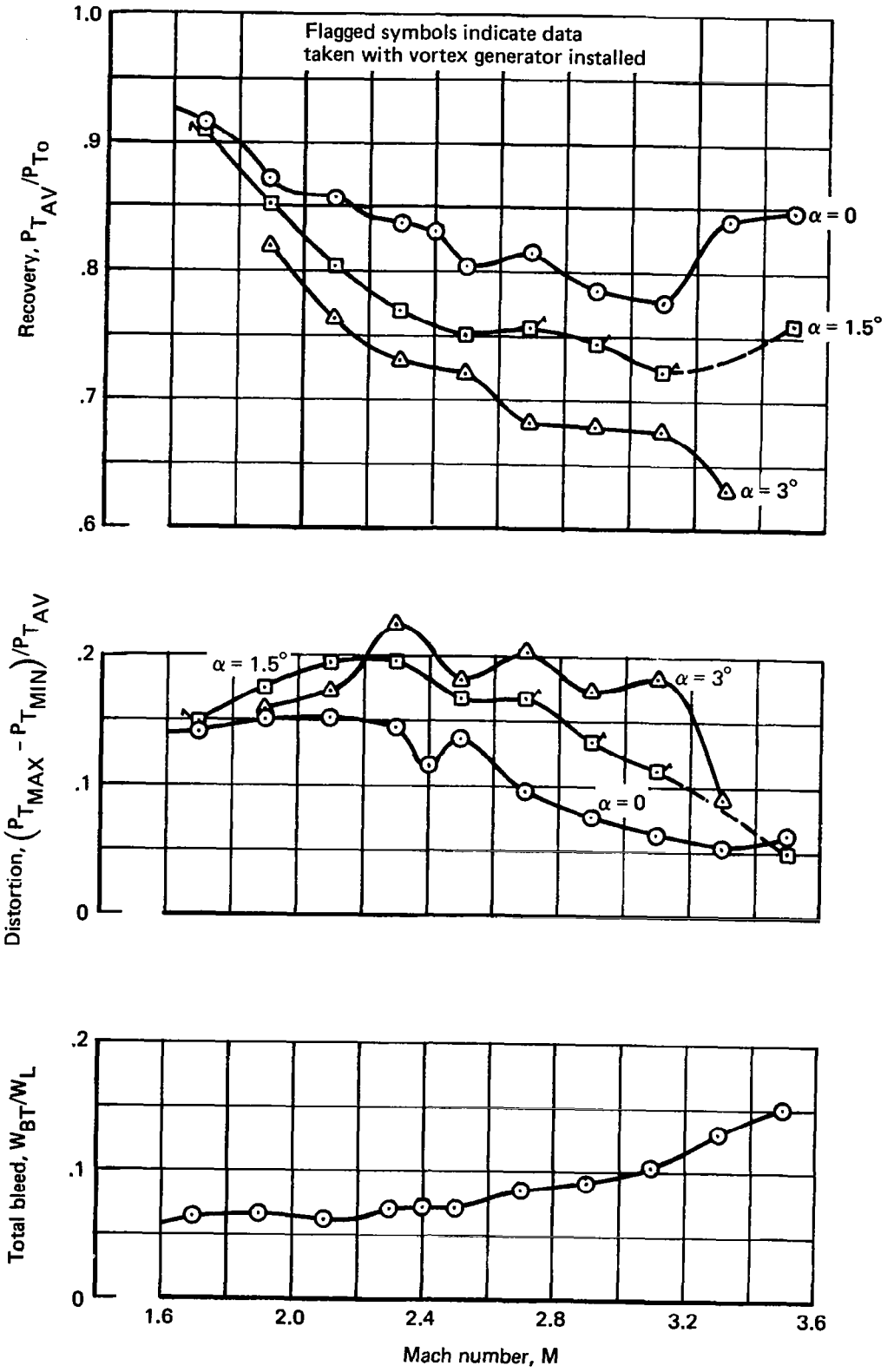

Figure 54.—Inlet Performance at Angle of Attack, Configuration 3

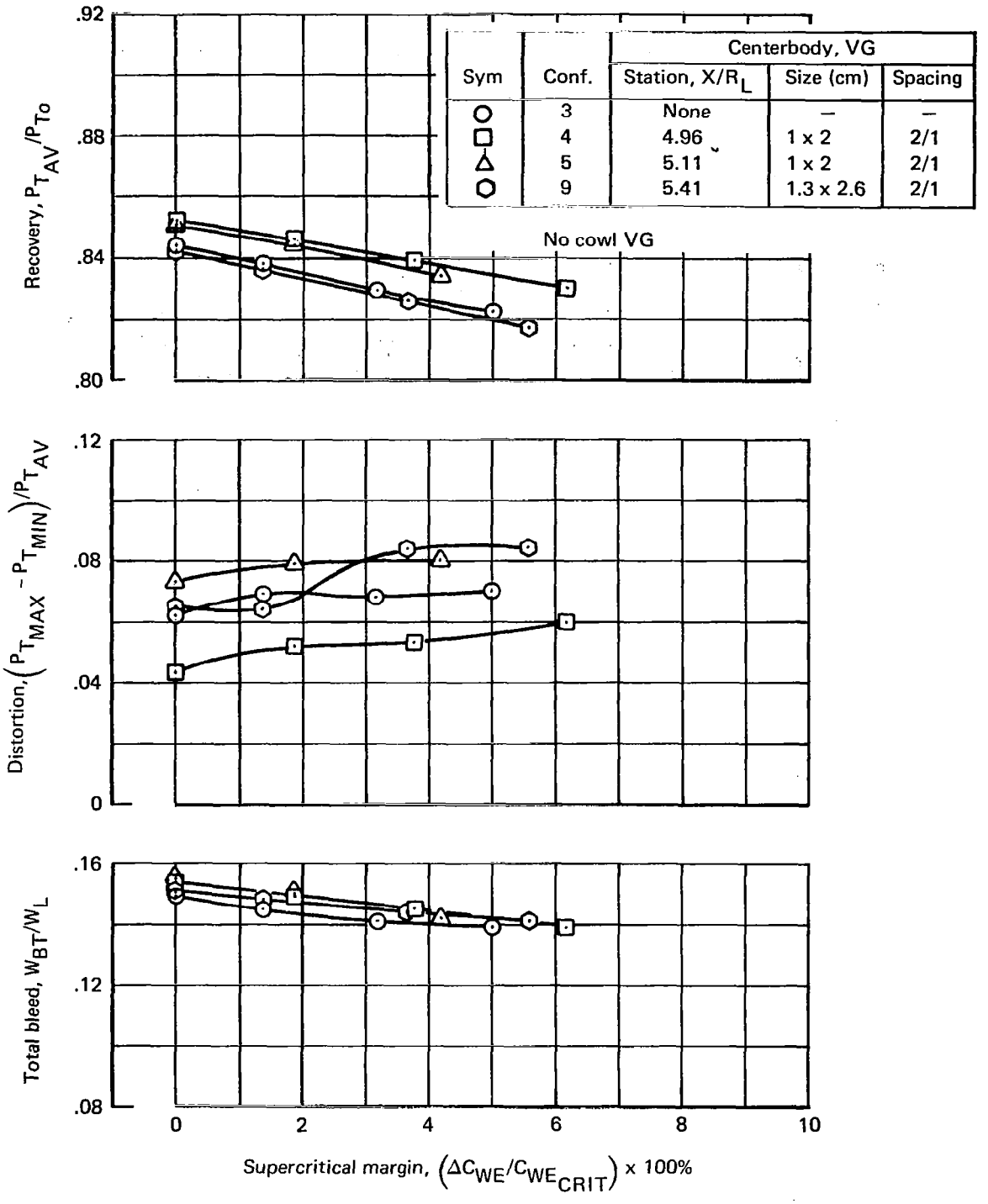

Figure 55.—Centerbody Vortex Generator Evaluation, M = 3.5, Configurations 3, 4, 5, and 9

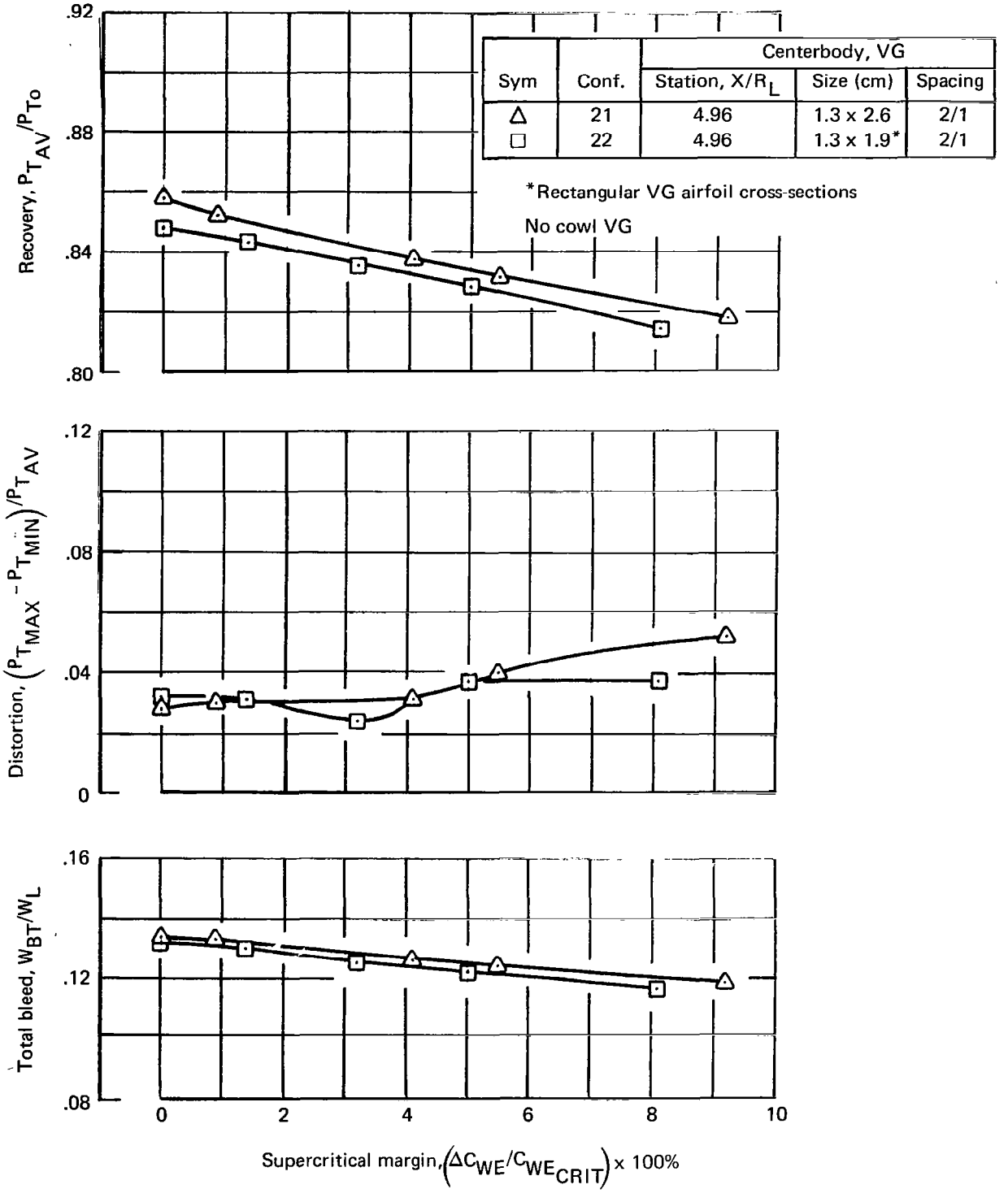

Figure 56.—Centerbody Vortex Generator Evaluation, M = 3.5, Configurations 21 and 22

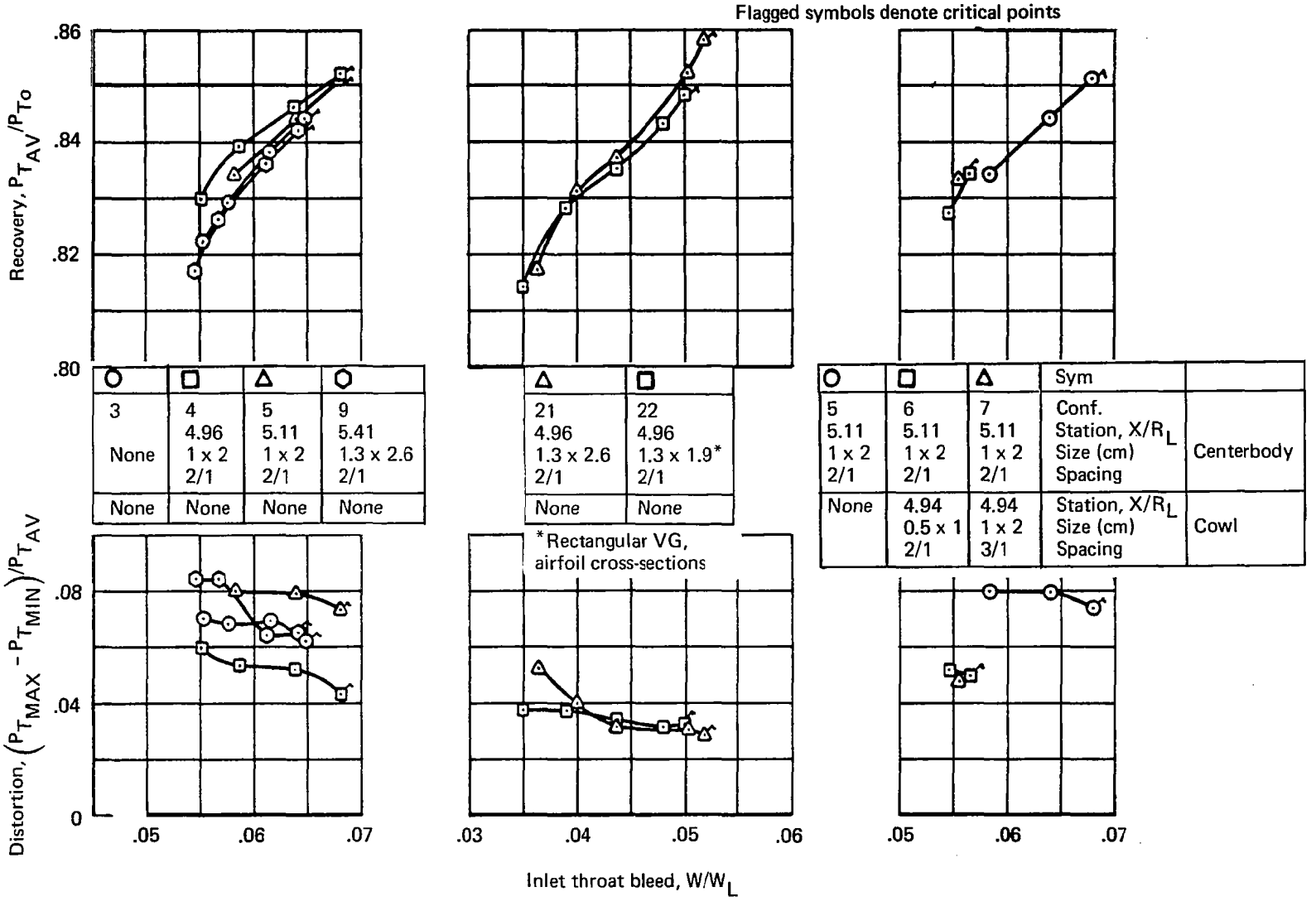

○	□	△	⬡	Sym	
3	4	5	9	Conf.	
	4.96	5.11	5.41	Station, X/R_L	
None	1 x 2	1 x 2	1.3 x 2.6	Size (cm)	Centerbody
	2/1	2/1	2/1	Spacing	
None	None	None	None	Station, X/R_L	

△	□	Sym	
21	22	Conf.	
4.96	4.96	Station, X/R_L	
1.3 x 2.6	1.3 x 1.9*	Size (cm)	Centerbody
2/1	2/1	Spacing	
None	None	Station, X/R_L	

○	□	△	Sym	
5	6	7	Conf.	
5.11	5.11	5.11	Station, X/R_L	
1 x 2	1 x 2	1 x 2	Size (cm)	Centerbody
2/1	2/1	2/1	Spacing	
None	4.94	4.94	Station, X/R_L	
	0.5 x 1	1 x 2	Size (cm)	Cowl
	2/1	3/1	Spacing	

Figure 57.—Effects of Vortex Generators on Inlet Performance, M = 3.5

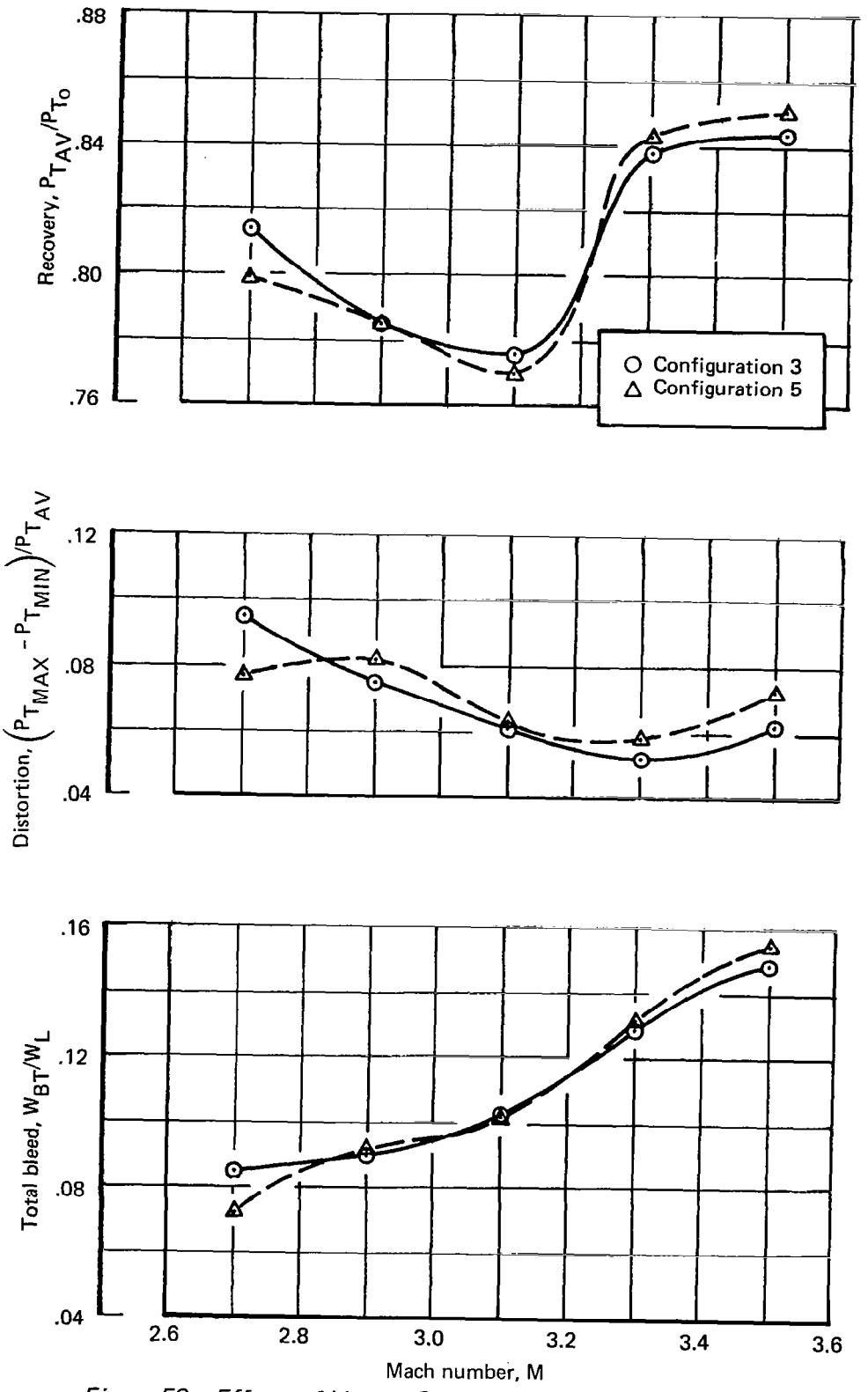

Figure 58.—Effects of Vortex Generators on Off-Design Performance

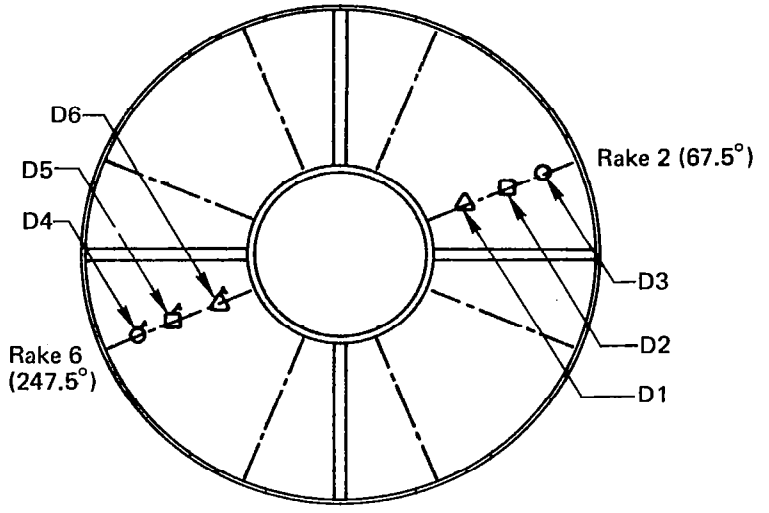

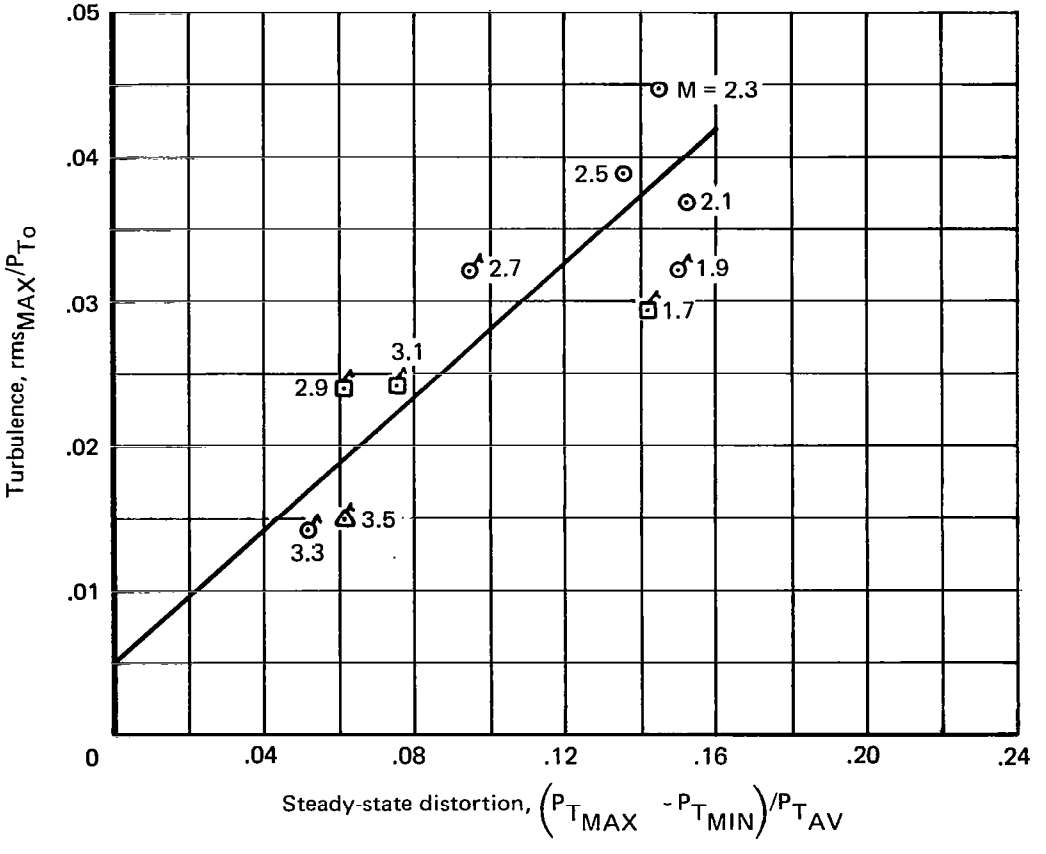

Figure 59.—Maximum Measured rms, Configuration 3, Critical Data

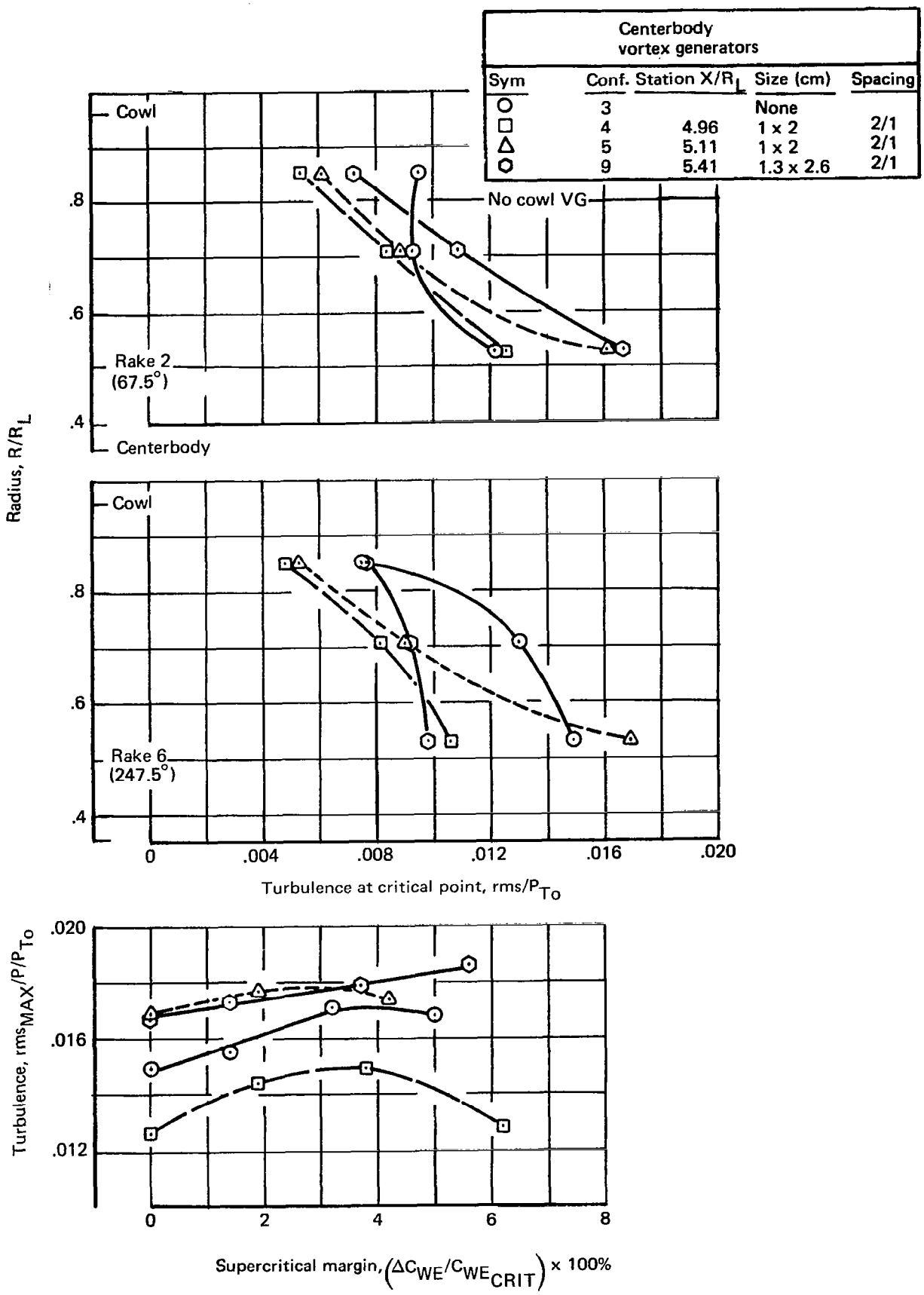

Figure 60.—Effects of Centerbody Vortex Generators on Engine-Face Turbulence, M = 3.5

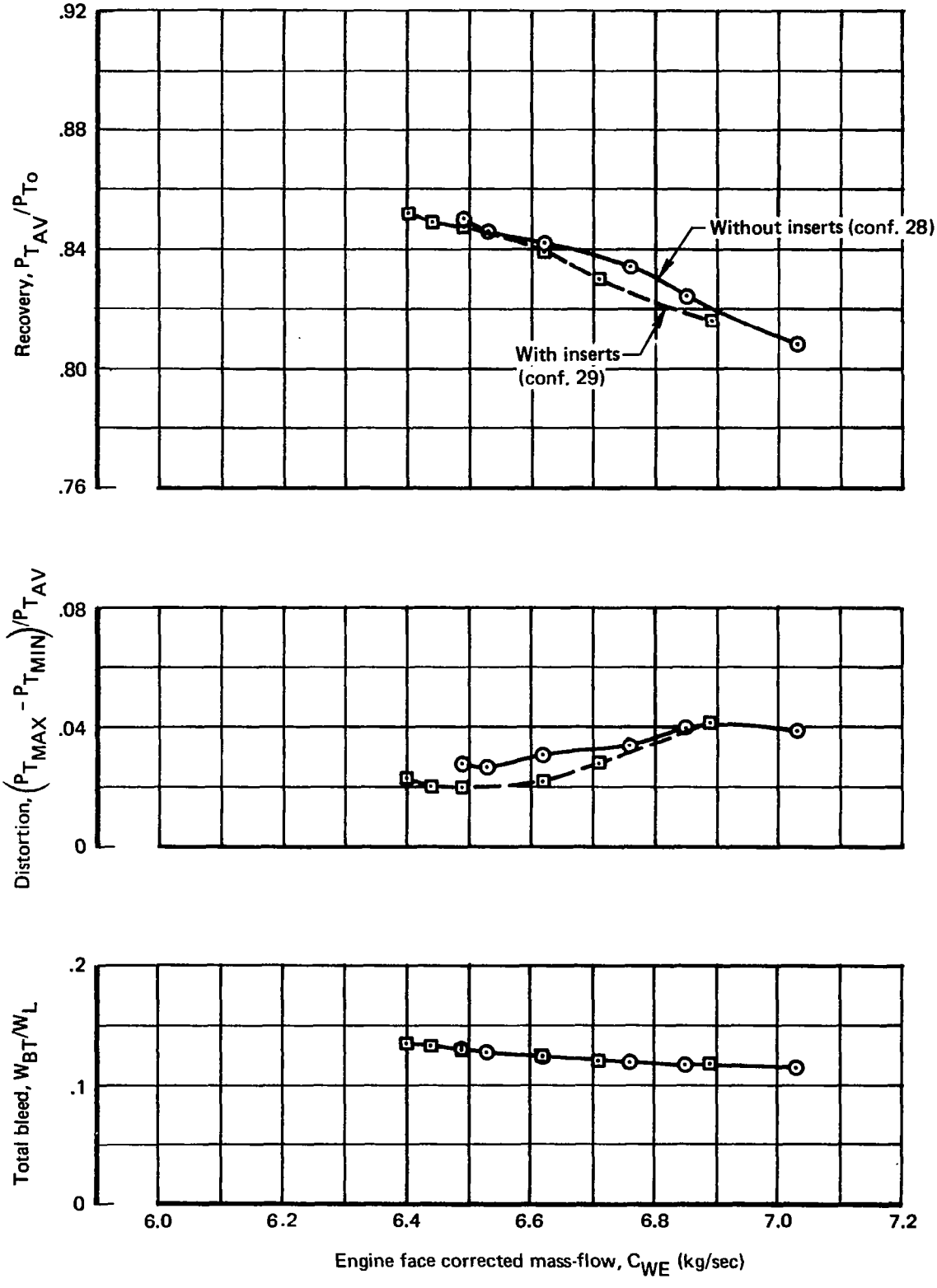

Figure 61.—Ramjet Insert Evaluation, M = 3.5, Configurations 28 and 29

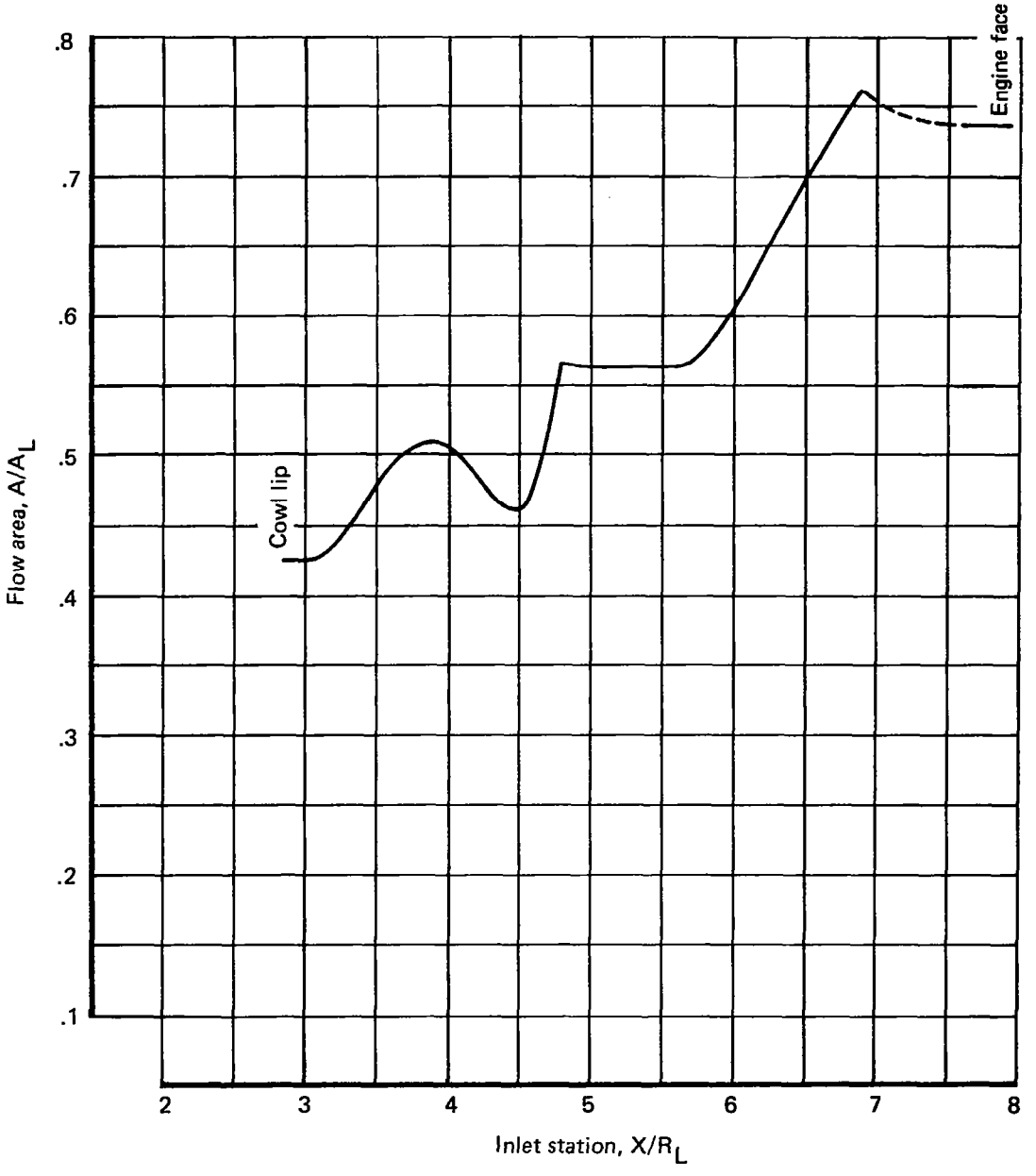

Figure 62.—Inlet Area Distribution, $\Delta X/R_L = 1.5$

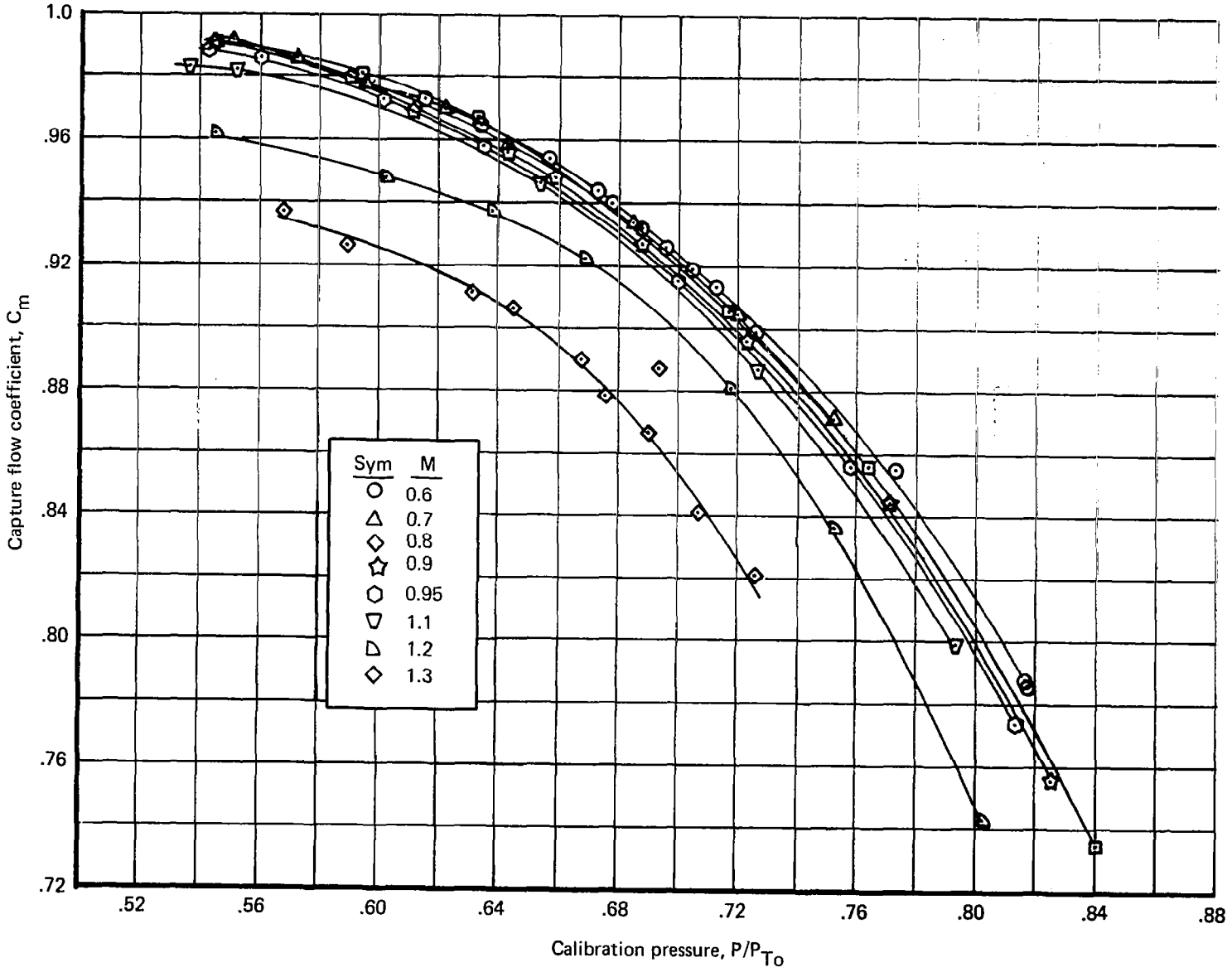

Figure 63.—Inlet Capture Flow Coefficient, Configuration 1

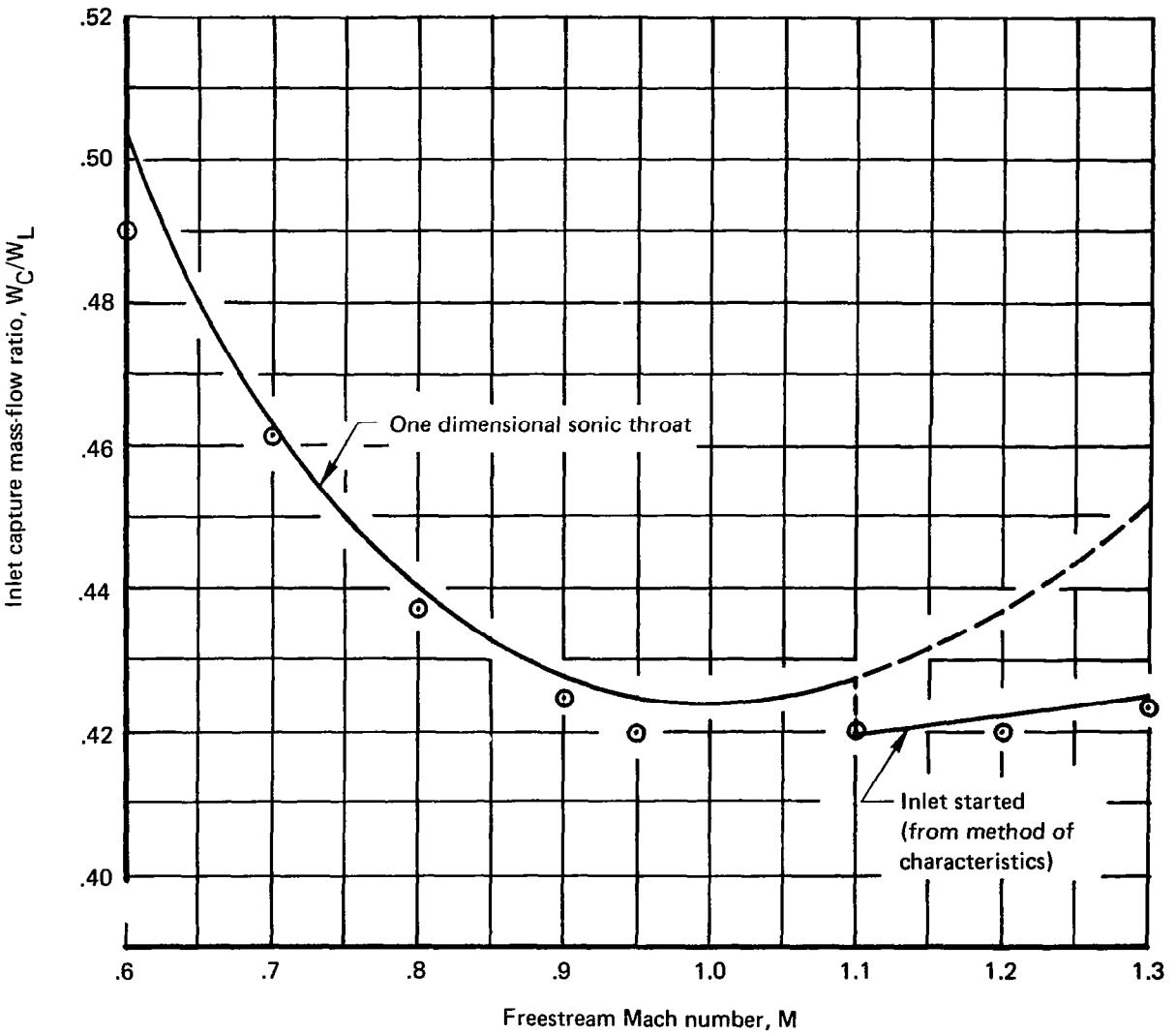

Figure 64.—Maximum Transonic Capture Flow, Configuration 1

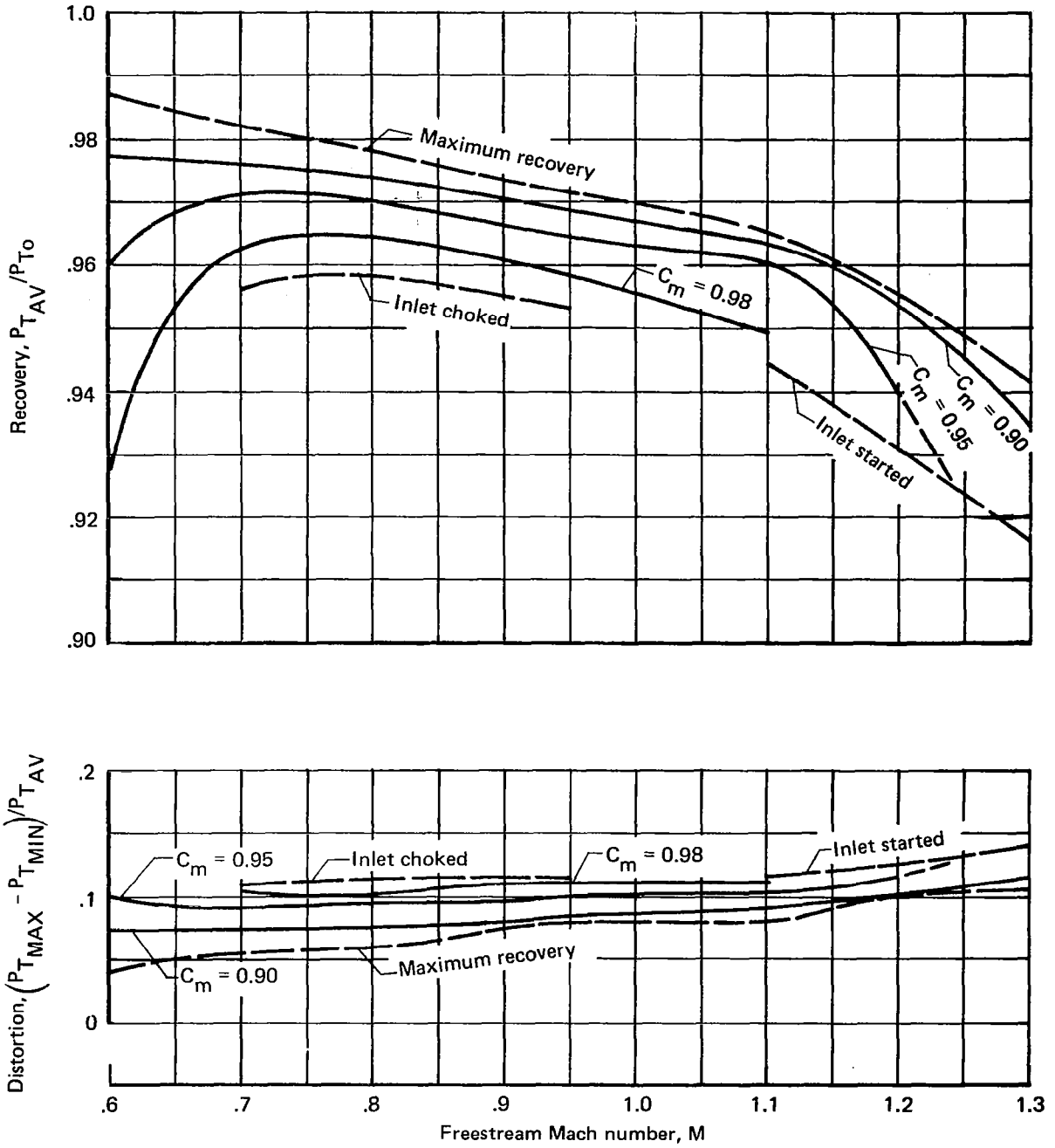

Figure 65.—Transonic Inlet Performance Summary, Configuration 1

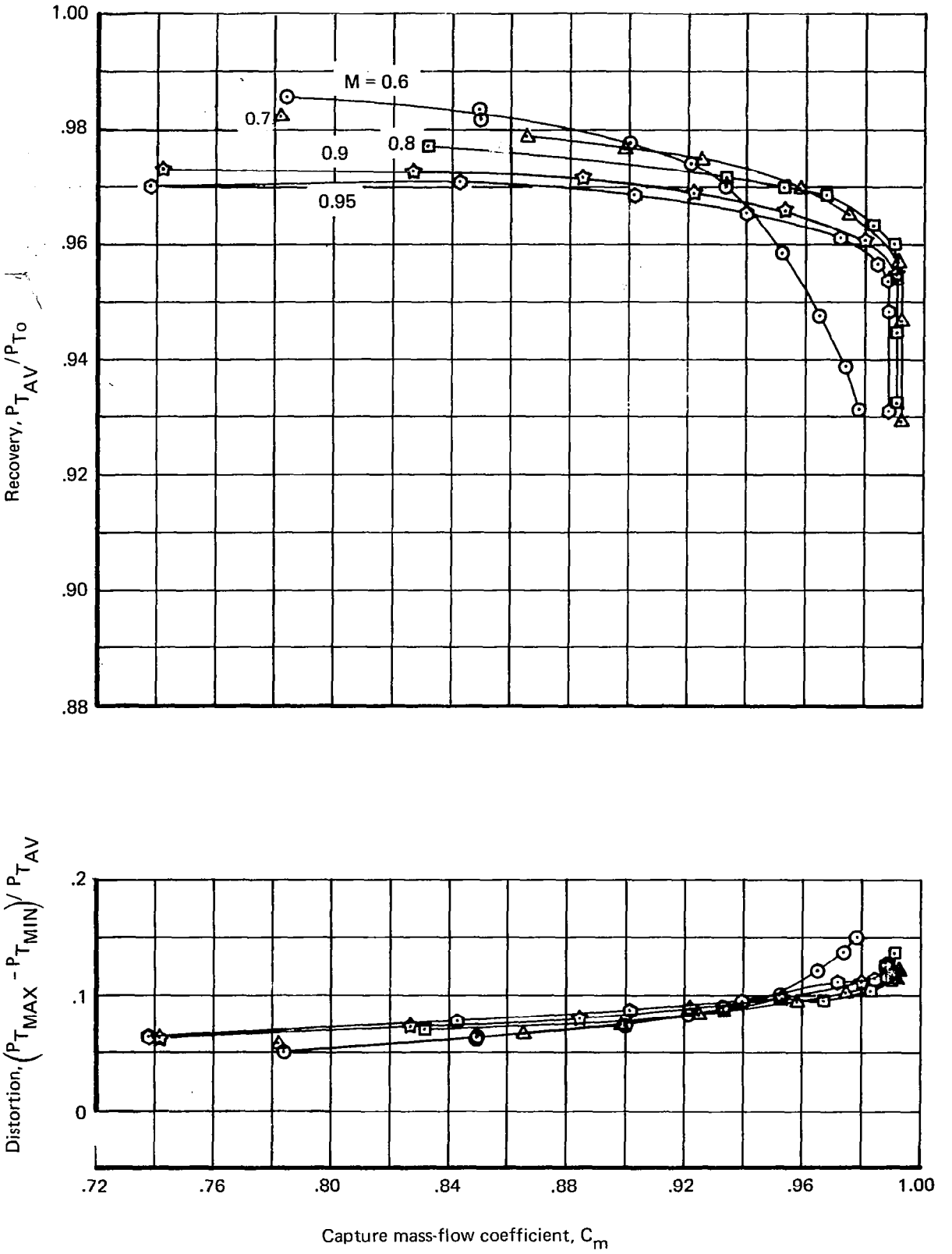

Figure 66.—Transonic Performance, $M < 1$

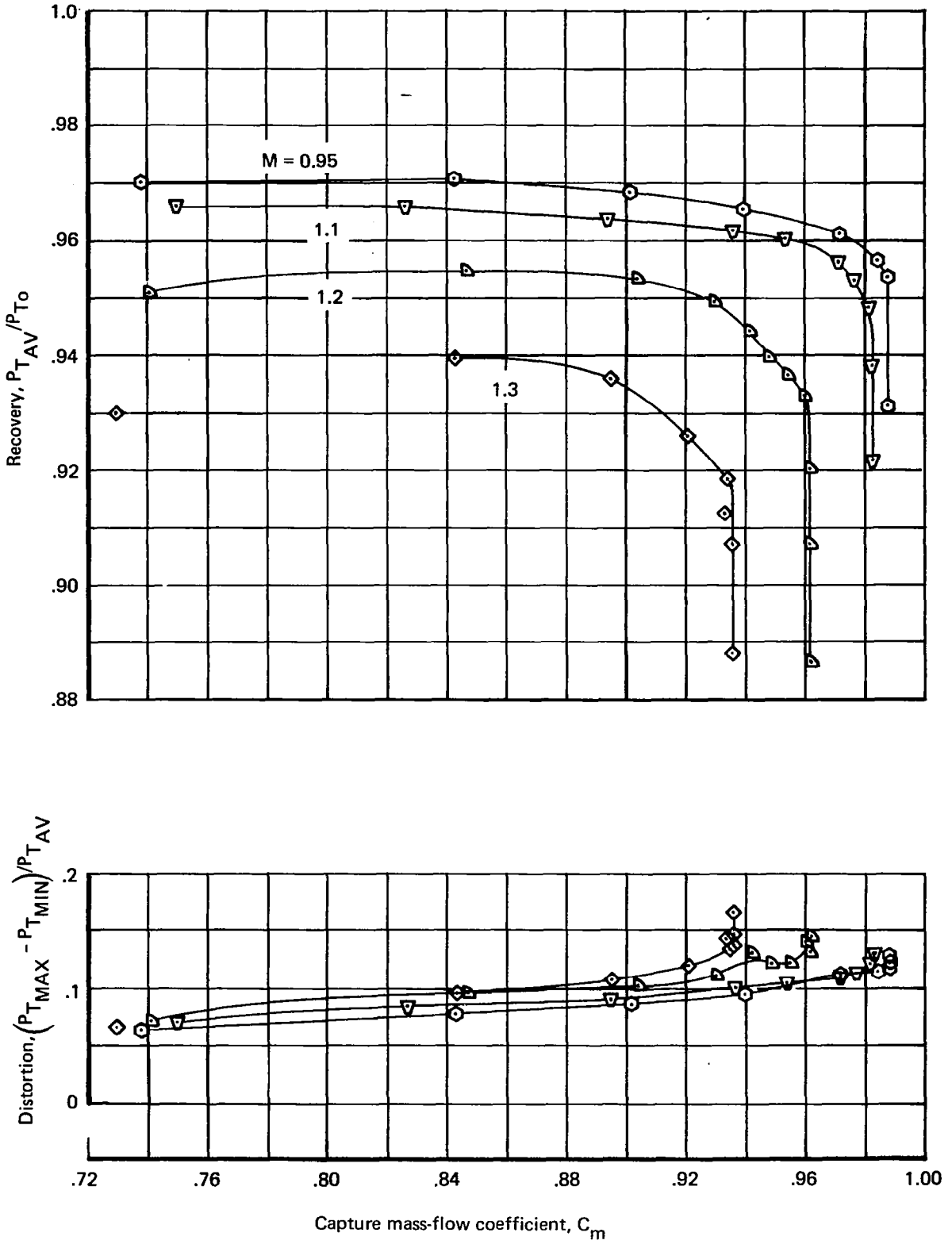

Figure 67.—Transonic Performance, M > 1

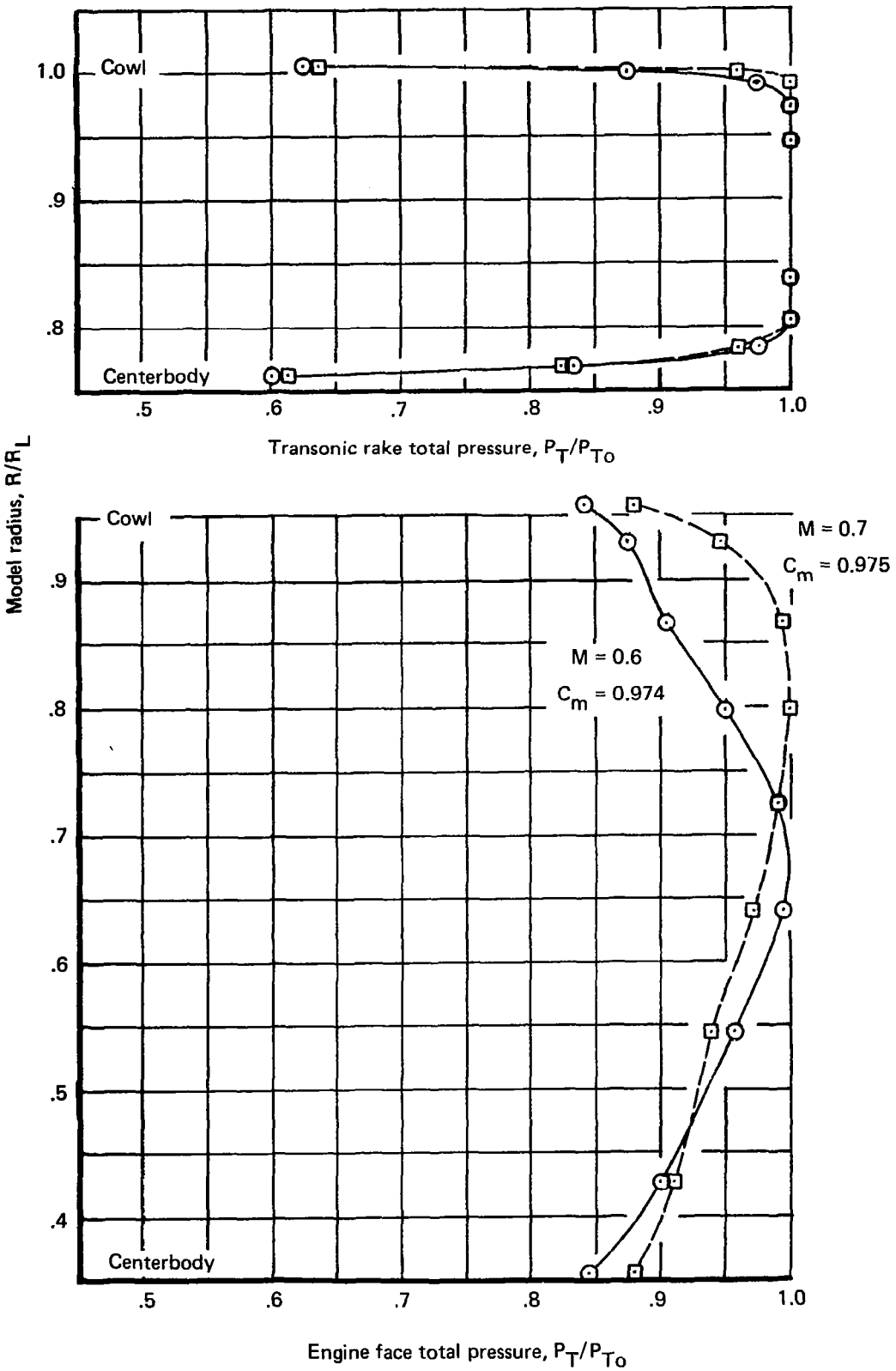

Figure 68.—Total-Pressure Profile Comparisons, M = 0.6 and 0.7

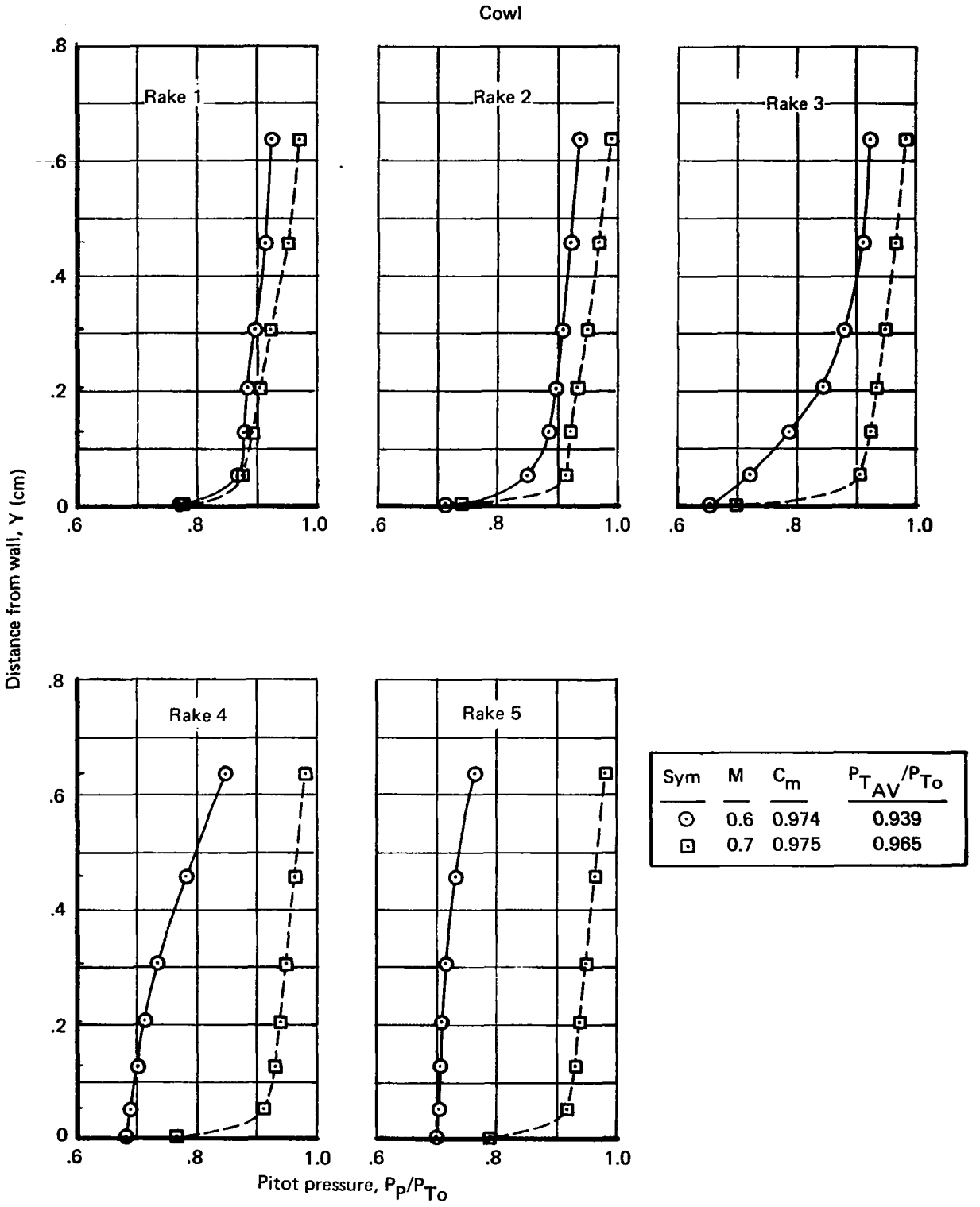

Figure 69.—Boundary-Layer Profile Comparisons, M = 0.6 and 0.7, Configuration 1

Sym	M	C_m	W_{BT}/W_L at 0°
⊙	0.6	0.90	0.024
△	0.95	0.98	0.026
⊡	1.3	0.90	0.035

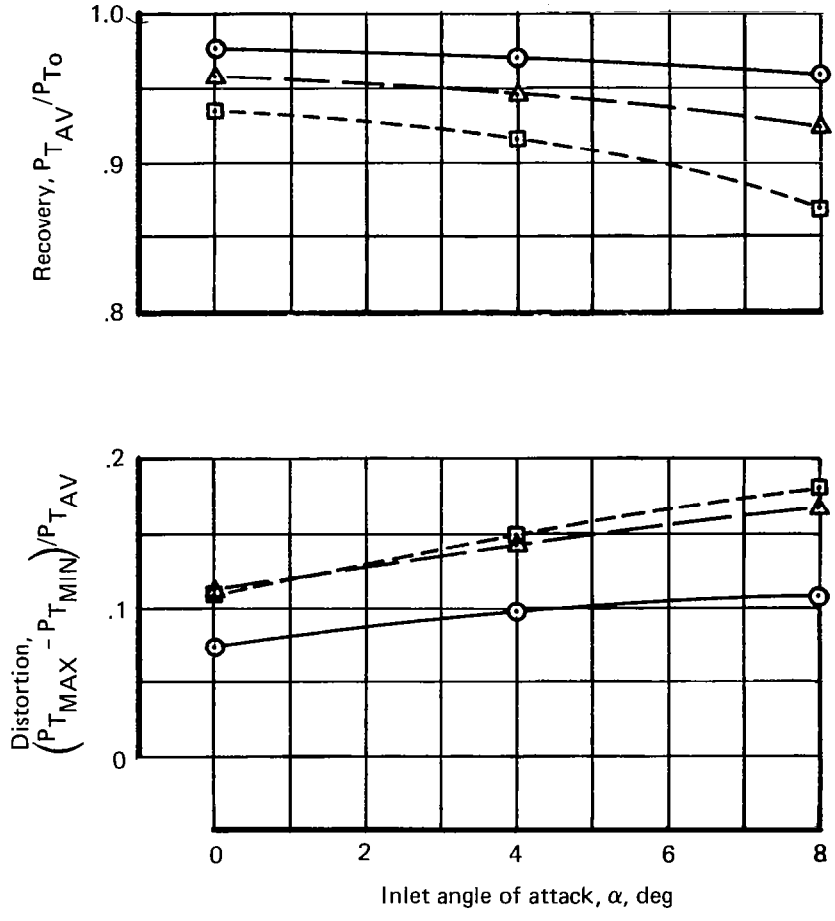

Figure 70.—Transonic Performance at Angle of Attack

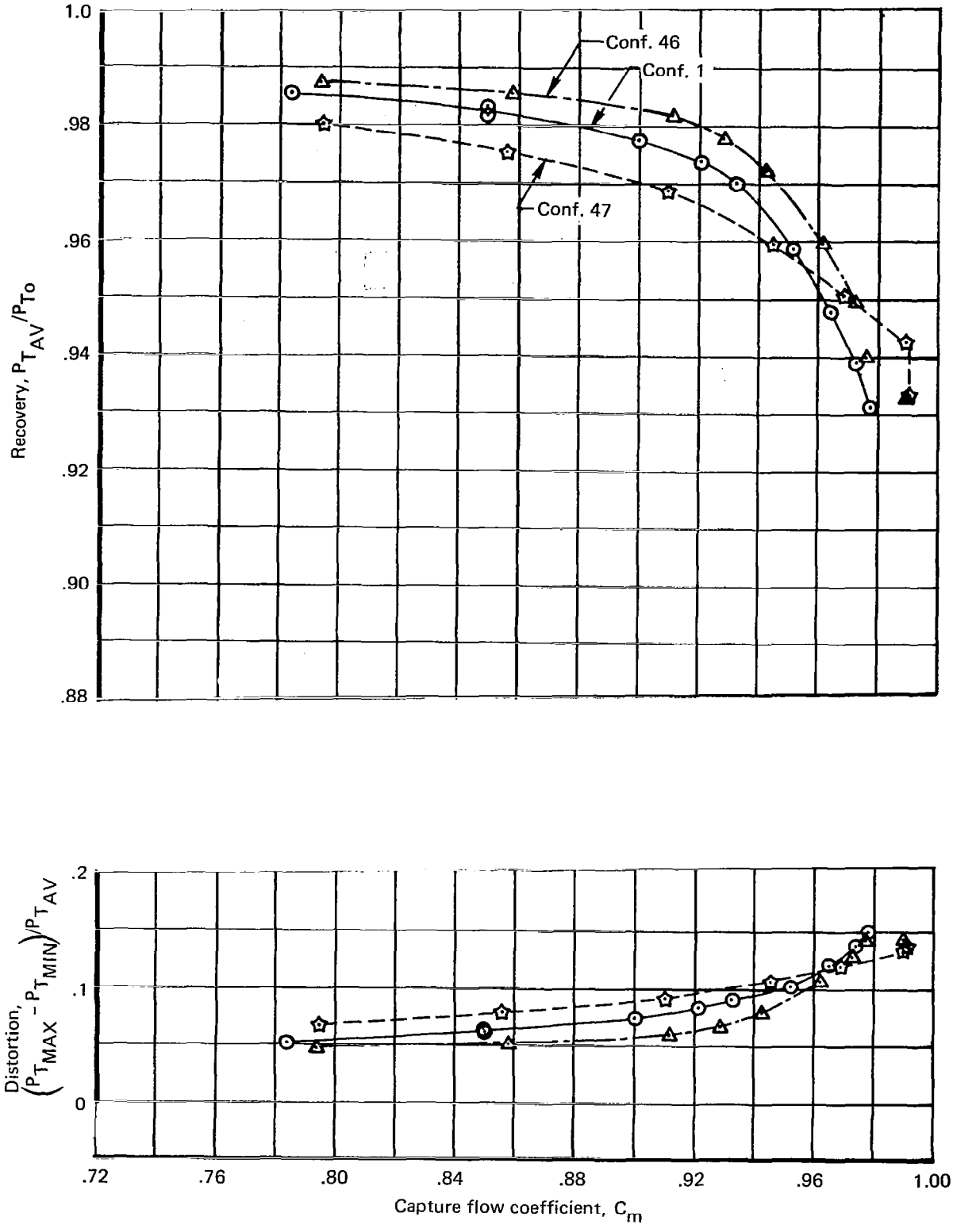

Figure 71.—Effects of Bleed System on Transonic Performance, M = 0.6

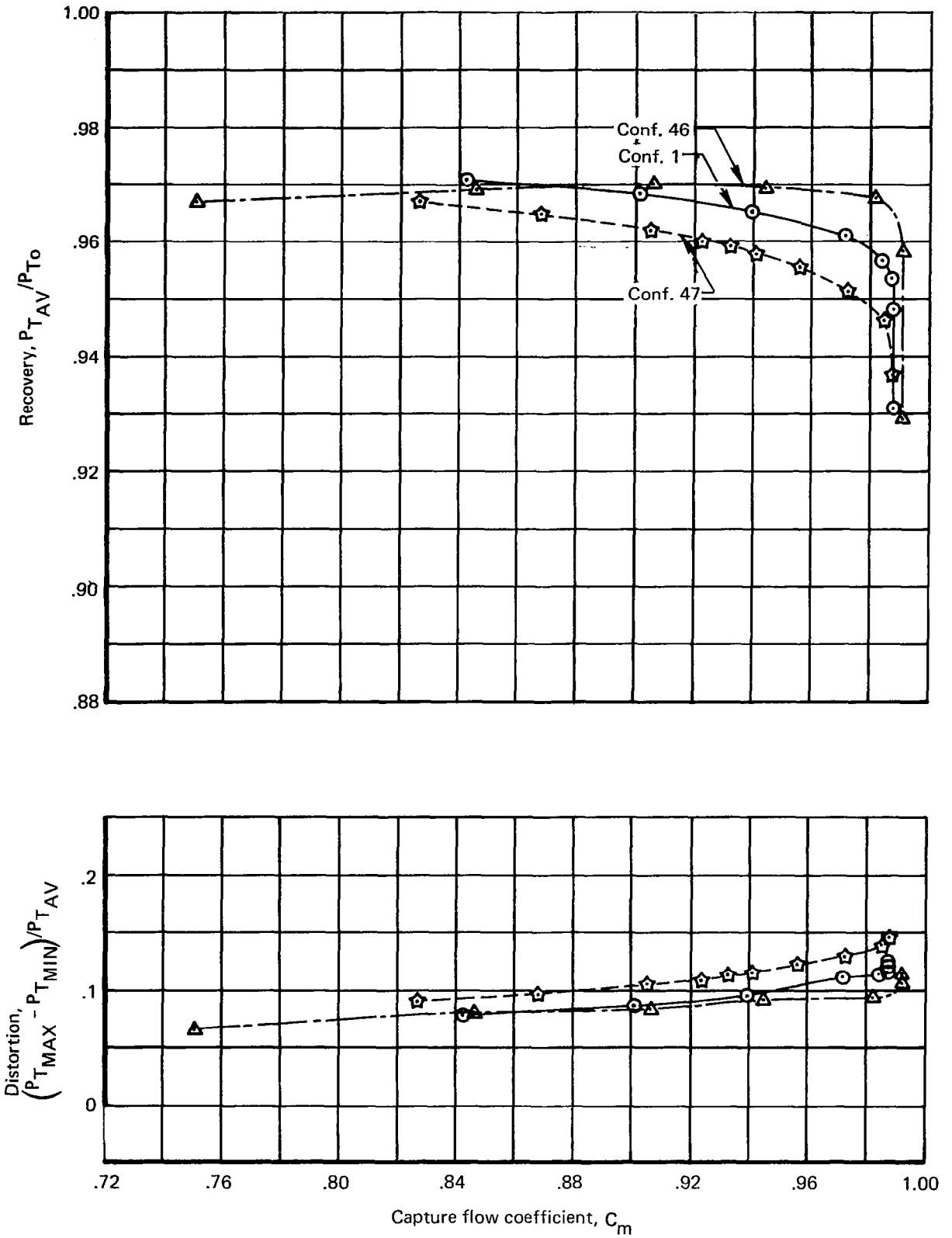

Figure 72.—Effects of Bleed System on Transonic Performance, M = 0.95

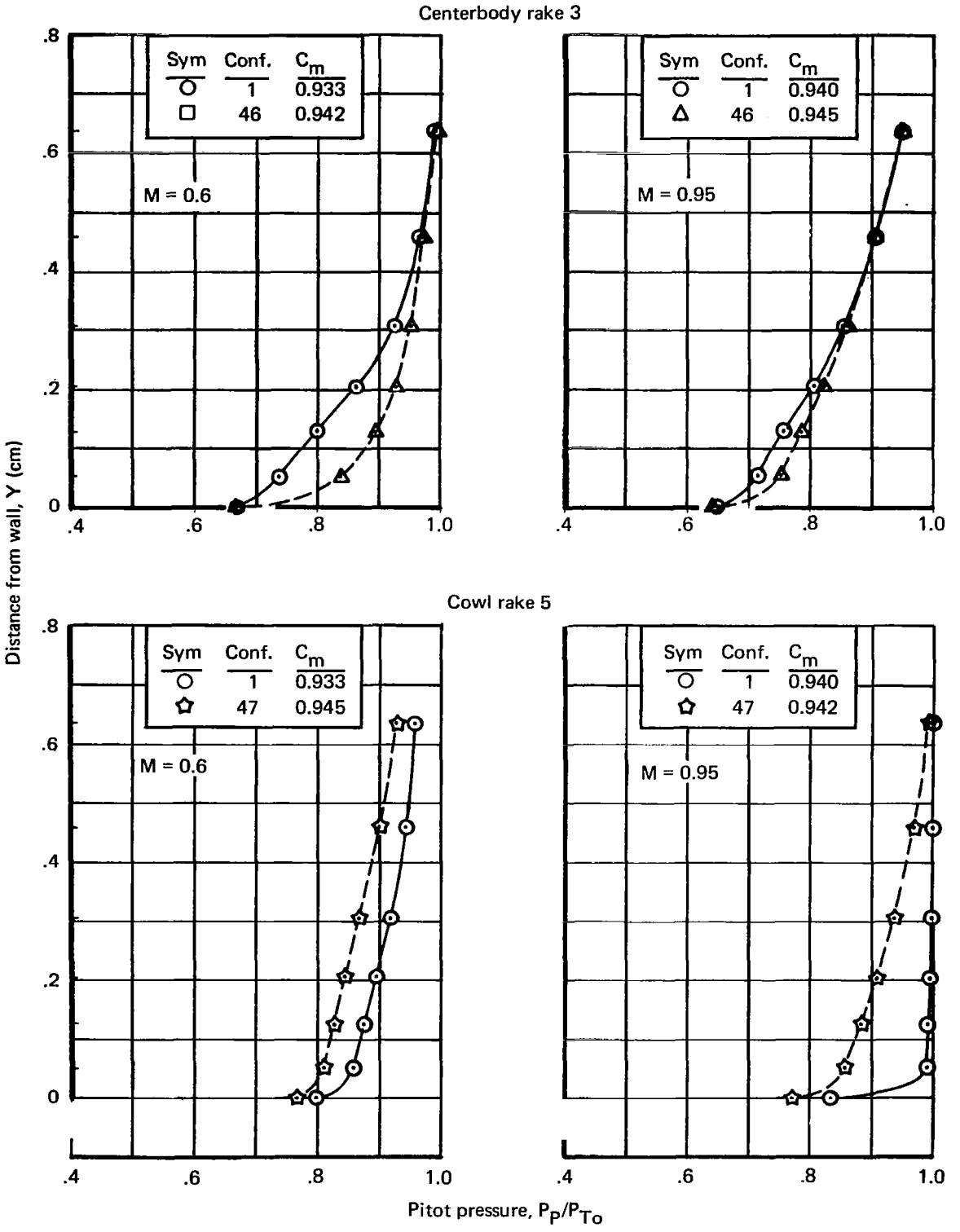

Figure 73.—Effects of Bleed System on Boundary Layer, M = 0.6 and 0.95

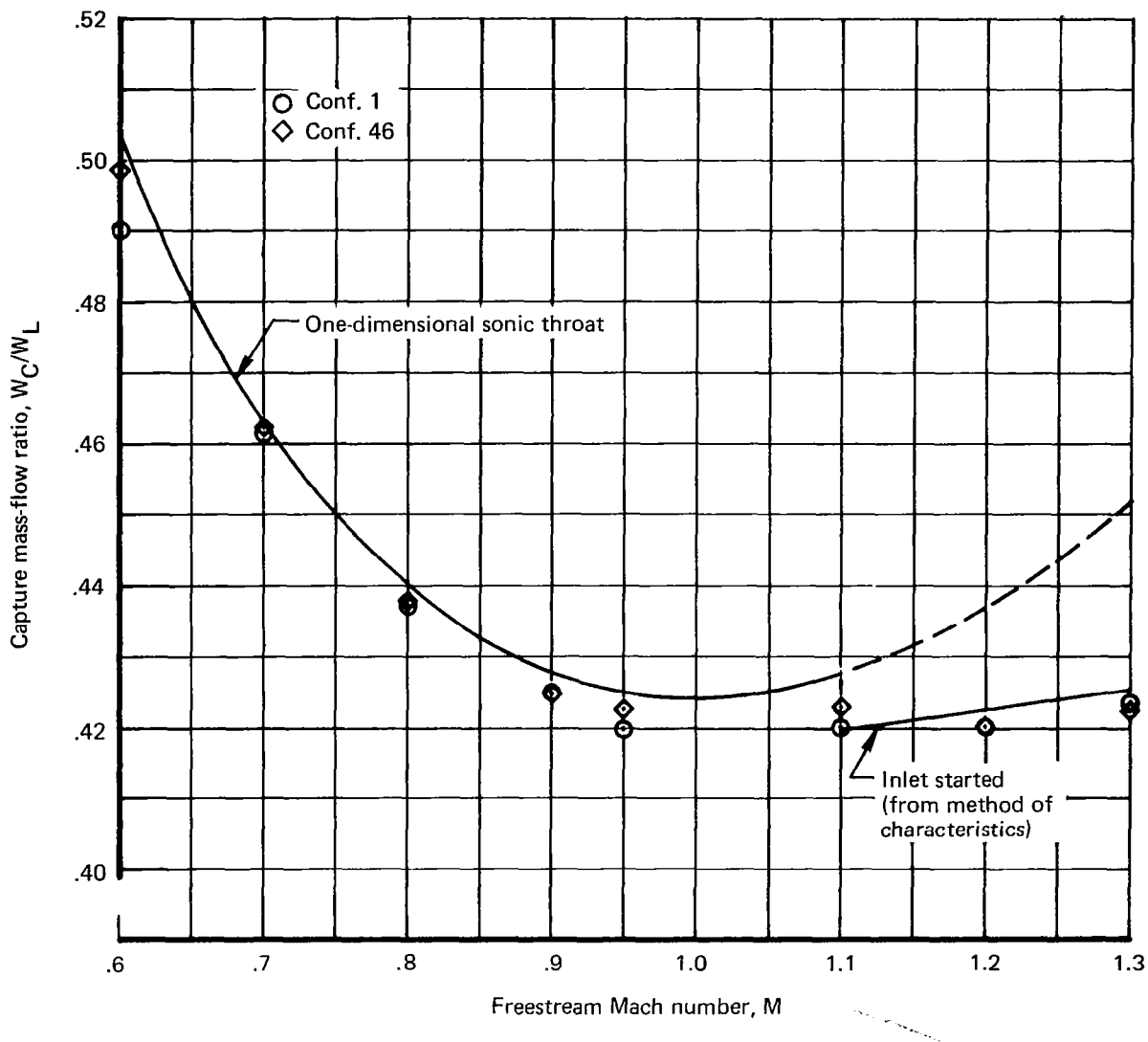

Figure 74.–Maximum Transonic Capture Flow, Configurations 1 and 46

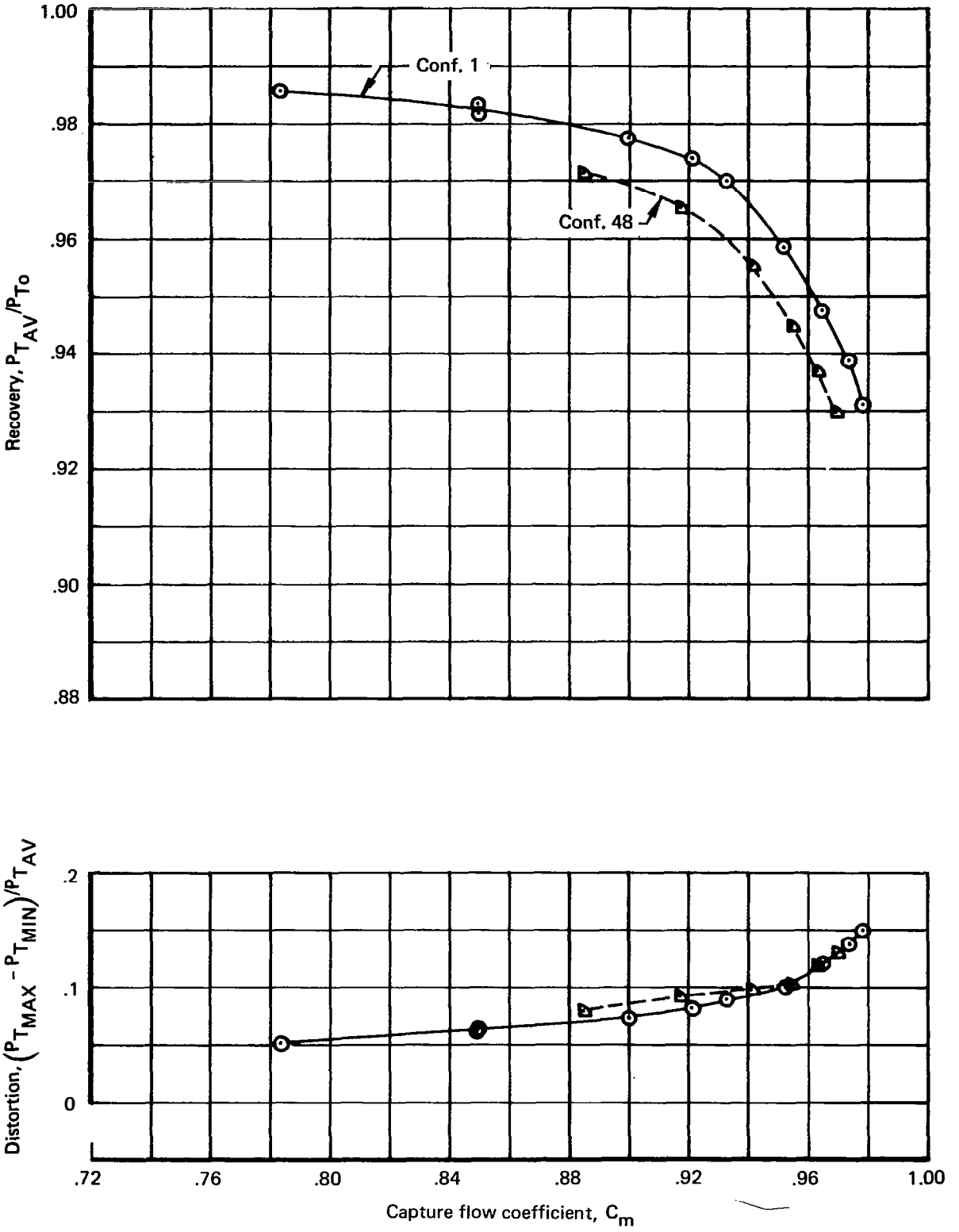

Figure 75.—Effects of Centerbody Vortex Generators on Transonic Performance, M = 0.6

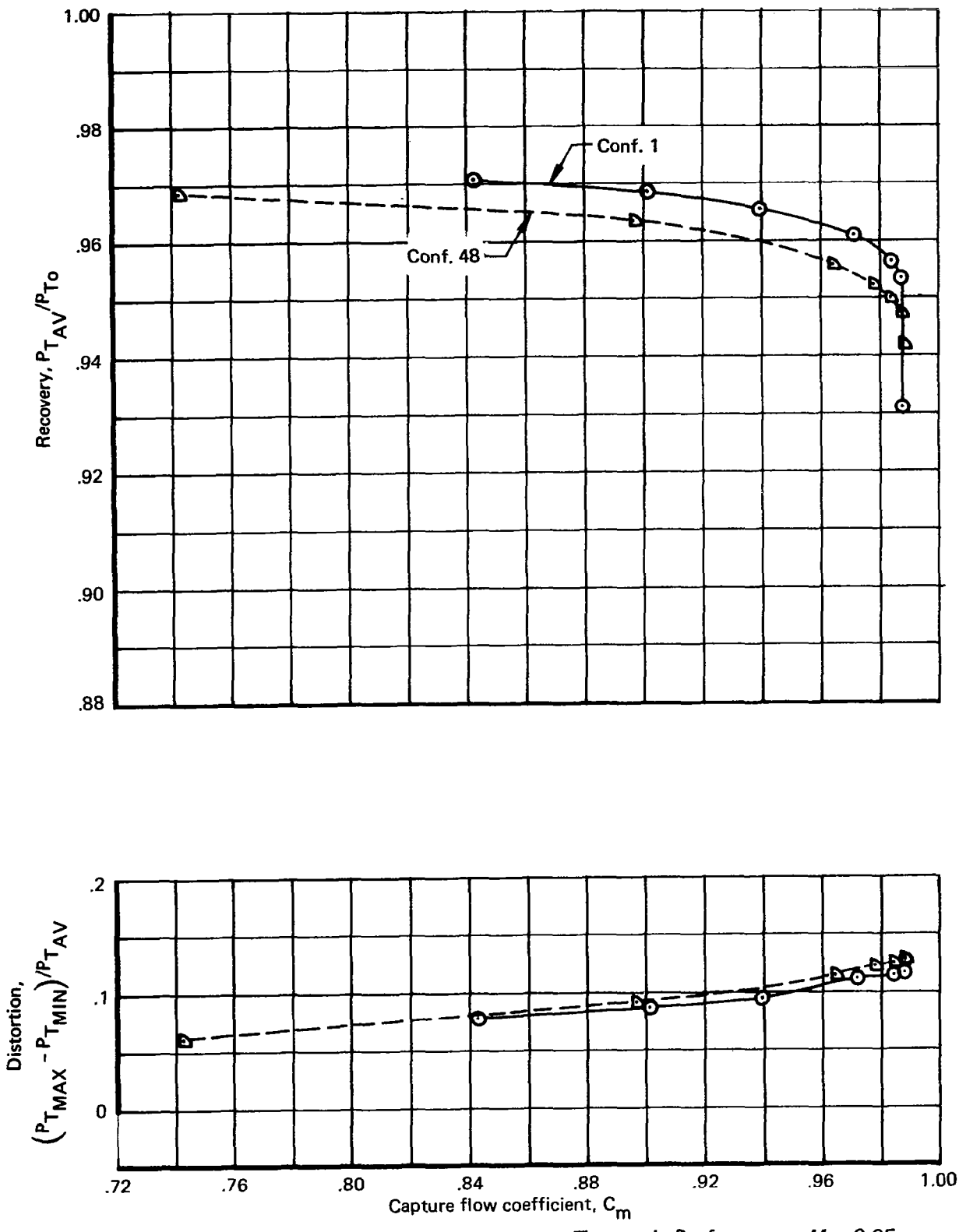

Figure 76.—Effects of Centerbody Vortex Generators on Transonic Performance, M = 0.95

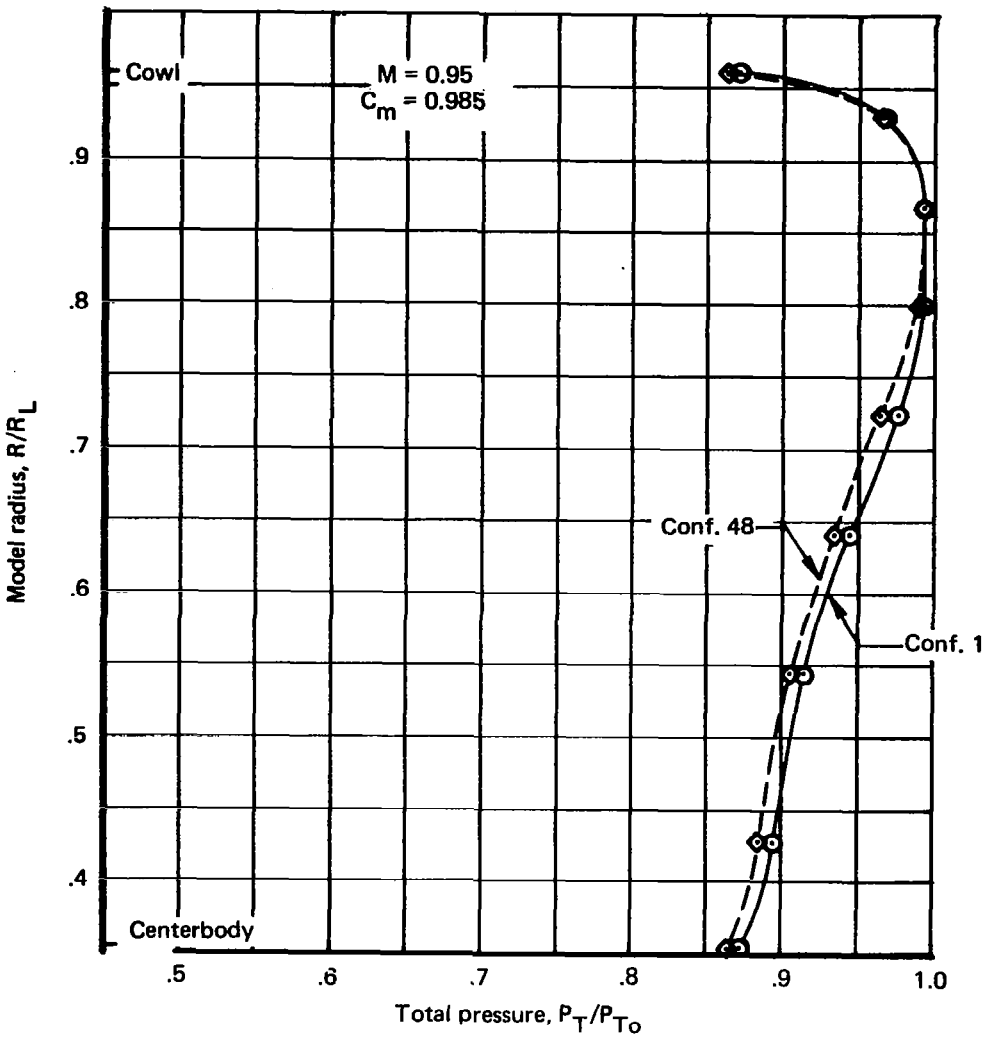

Figure 77.—Effects of Centerbody Vortex Generators on Engine-Face Total-Pressure Profile, M = 0.95

Table 1.—Inlet Contours

X/R_L	R/R_L	Slope
Centerbody		
0.0	0.0	0.17633
4.0	0.70532	0.17633
4.1	0.7228	
4.2	0.7387	0.144
4.3	0.7512	
4.4	0.759	0.052
4.5	0.7625	
4.55	0.763	0.0
4.6	0.7625	
4.65	0.7611	
4.7	0.7585	-0.0646
4.8	0.7504	
4.9	0.7391	-0.1295
5.1	0.7120	
5.3	0.6829	
5.5	0.6525	-0.153
5.6	0.6362	
5.7	0.618	
5.8	0.5973	
5.9	0.5744	
6.0	0.5467	
6.1	0.5093	
6.2	0.4564	
6.28	0.4	-0.794
Cowl		
2.86	1.0	0.01745
3.1	1.004188	0.01745
3.2	1.0054	
3.4	1.0051	-0.011
3.6	0.99996	
3.8	0.9882	
4.0	0.9681	-0.124
4.1	0.954	
4.2	0.9364	-0.1942
4.25	0.9261	
4.3	0.9154	-0.213
4.4	0.8949	
4.5	0.8768	-0.163
4.55	0.8695	
4.6	0.864	-0.093
4.65	0.86	
4.7	0.8572	-0.0485
4.8	0.8533	
4.9	0.8511	

Table 1.—(Concluded)

X/R_L	R/R_L	Slope
Cowl		
5.0	0.8502	
5.1	0.85	0.0
5.6	0.85	0.0
5.8	0.8574	
5.9	0.8646	
6.0	0.8735	
6.1	0.8839	0.107
6.2	0.8946	
6.3	0.9050	
6.4	0.9145	
6.5	0.9227	0.0729
6.6	0.9299	
6.7	0.9368	
6.8	0.9435	
6.9	0.95	0.065

Table 2.—Bleed Holes

Plenum	Row number	Row station	Number of holes/row	Hole diameter cm	Hole angle deg
Centerbody					
F1	1*	4.200	360	0.159	20
	2*	4.224			
	3	4.280			
	4	4.304			
	5*	4.328			
	6*	4.352			
F2	7	4.455	480	0.127	20
	8	4.480			
	9	4.505			
	10	4.530			
	11*	4.555			
T1	12	4.625	880	0.066	20
	13	4.635			
	14*	4.655			
	15*	4.665			
T2	16	4.725	880	0.066	20
	17	4.735			
	18*	4.780			
	19*	4.790			
T3	20	4.875	600	0.091	20
	21	4.890			
T4	22	5.025	600	0.091	20
	23	5.040			
T5	24	5.177	520	0.102	20
	25	5.193			
F3	26	5.264	520	0.102	20
	27	5.276			
	28	5.288			
	29	5.300			
T6	30	5.360	400	0.127	20
	31	5.380			
T7	32	5.480	400	0.127	20
	33	5.500			
T8	34	5.620	280	0.159	20
	35	5.645			
T9	36	5.770	280	0.159	20
	37	5.795			

*Alternate bleed rows

Table 2.—Concluded

Plenum	Row number	Row station	Number of holes/row	Hole diameter, cm	Hole angle, deg
Cowl					
0	1	3.835	1160	0.066	20
	2	3.845			
1	3*	4.167	680	0.102	20
	4*	4.183			
	5	4.217			
	6	4.233			
	7*	4.267			
	8*	4.283			
	9	4.317			
	10	4.333			
	11*	4.349			
	12*	4.365			
2	13*	4.505	720	0.091	20
	14	4.523			
	15	4.541			
	16	4.559			
	17	4.577			
	18*	4.595			
3	19	4.665	880	0.076	90
	20	4.670			
	21	4.695			
	22	4.700			
	23	4.725			
	24	4.730			
	25*	4.755			
	26*	4.760			

*Alternate bleed rows

Table 3.—Total-Pressure Rake Locations

Compressor Face Rakes at X/R_L Station 7.95

Rake number	1	2	3	4	5	6	7	8
Angular position, deg	22.5	67.5	112.5	157.5	202.5	247.5	292.5	337.5

Probe number	1	2	3	4	5	6	7
Radius, cm	23.096	21.524	19.830	17.976	15.908	13.526	10.622

Dynamic pressure Probe number (rakes 1 and 5 only)	1	2	3
Radius, cm	21.118	17.569	13.119

Sting Rakes at X/R_L Station 10.753

Rake number	1	2	3	4
Angular position, deg	45	135	225	315

Probe number	1	2	3
Radius, cm	24.216	19.764	13.957

Cowl Boundary Layer Rakes

Rake number	1	2	3	4	5
X/R_L station	4.11	4.38	4.582	4.74	4.86
Angular position, deg	36	108	180	252	324

Probe number	1	2	3	4	5	6
Distance from wall, cm	0.051	0.127	0.203	0.305	0.457	0.635

Centerbody Boundary Layer Rakes

Rake number	1	2	3	4	5
X/R_L station	4.12	4.38	4.57	4.67	4.82
Angular position, deg	0	72	144	216	288

Probe number	1	2	3	4	5	6
Distance from wall, cm	0.051	0.127	0.203	0.305	0.457	0.635

Transonic Lip Rakes

Rake number	1	2
X/R_L station	3.12	3.12
Angular position, deg	95	275

Probe number	1	2	3	4	Prandtl static	5	6	7	8
Radius, cm	24.867	24.600	24.166	23.470	22.167	20.777	19.967	19.428	19.086

Table 4.—Configuration Log for Bleed Study at M = 3.5

	Conf.	Open bleed rows[a]				Bleed exit area, A/A_L			VG[b] station, X/R_L
		F1	F2	T1	T2	D1	D2	D3	
Centerbody	1	3, 4	7, 8, 9, 10	12, 13	16, 17	0.0341	0.0490	0.0177	No
	3		7, 8, 9, 10	12, 13, 14, 15	16, 17, 18, 19		0.0600	0.0221	No
	10		7, 8, 9, 10						5.41
	11		8, 9						
	12		8, 9	12, 13, 14, 15	16, 17, 18, 19			0.0221	
	13		8, 9	12, 13	16, 17			0.0177	
	14		7, 8, 9, 10						
	15								
	16	3, 4					0.0600		
	17					0.0341	0.0490	0.0177	
	18	3, 4				0.0135	0.0300	0.0121	5.41
	21	3, 4	7, 8, 9, 10	12, 13	16, 17	0.0135	0.0300	0.0121	4.96
		C0	C1	C2	C3	C0	C1	C2	C3	
Cowl	1	1, 2	5, 6, 9, 10	14, 15, 16, 17	19, 20, 21, 22, 23, 24	0.0098	0.0280	0.0186	0.0192	No
	3	1, 2				0.0098				
	10					0				
	11		5, 6, 9, 10			0				
	12		9, 10			0				
	13					0				
	14			14, 15, 16, 17		0		0.0186		
	15		9, 10	13, 14, 15, 16, 17, 18		0		0.0279		
	16		5, 6, 9, 10			0				
	17					0	0.0280	0.0279		
	18					0	0.0224	0.0186		
	21	1, 2	5, 6, 9, 10	13, 14, 15, 16, 17, 18	19, 20, 21, 22, 23, 24	0.0098	0.0224	0.0186	0.0192	No

[a]All bleed rows were left open in centerbody plenums T3, T4, T5, F3, T6, T7, T8, and T9

[b]All VG patterns listed used 24 pairs of 1.3- by 2.6-cm triangular generators

Table 5.—Forward Bleed Flow Rates at M = 3.5

Configuration	Cowl 0	Cowl 1	Cowl 2	Centerbody F1	Centerbody F2
Predicted	0.003	0.016	0.031	0.010	0.030
1	0.002	0.013	0.020	0.010	0.029
16	0	0.014	0.026	0.011	0.029
21	0.002	0.012	0.027	0.007	0.026

Table 6.—Bleed Flow Rates and Plenum Pressures, Mach 3.5, Configurations 1 and 21

	Conf. 1 M = 3.5		Conf. 21 M = 3.5	
	$\alpha = 0$	$\alpha = 0^a$	$\alpha = 0$	$\alpha = 0^a$
W_{C0}/W_L	0.002	0.002	0.002	0.002
P_{C0}/P_{To}	0.038	0.039	0.035	0.035
W_{C1}/W_L	0.013	0.013	0.013	0.012
P_{C1}/P_{To}	0.066	0.067	0.079	0.078
W_{C2}/W_L	0.020	0.020	0.028	0.028
P_{C2}/P_{To}	0.154	0.155	0.219	0.218
W_{C3}/W_L	0.034	0.023	0.030	0.020
P_{C3}/P_{To}	0.255	0.169	0.228	0.153
W_{D1}/W_L	0.010	0.010	0.007	0.007
P_{D1}/P_{To}	0.080	0.082	0.121	0.120
W_{D2}/W_L	0.029	0.029	0.026	0.026
P_{D2}/P_{To}	0.155	0.156	0.202	0.201
W_{D3}/W_L	0.025	0.024	0.021	0.020
P_{D3}/P_{To}	0.276	0.255	0.315	0.286
$(W_C\text{-}W_{BT})/W_L$	0.861	0.873	0.866	0.878
A_{BT}/A_L	0.166		0.126	

[a]Operating point, 5.5% supercritical margin

Table 7.—Off-Design Forward Centerbody Bleed Rates, W/W_L

Configuration	Mach number					
	2.3	2.5	2.7	2.9	3.1	3.3
1	0.018	0.016	0.017	0.017	0.016	0.025
3	0.021	0.020	0.023	0.025	0.025	0.030
Predicted	0.023	0.020	0.027	0.025	0.024	0.033

Table 8.—Bleed Flow Rates and Plenum Pressures, Configuration 3

Conf. 3	M = 3.5		M = 3.3		M = 3.1			M = 2.9			M = 2.7		
	$\alpha = 0$	$\alpha = 1.5$	$\alpha = 0$	$\alpha = 3$	$\alpha = 0$	$\alpha = 1.5$	$\alpha = 3$	$\alpha = 0$	$\alpha = 1.5$	$\alpha = 3$	$\alpha = 0$	$\alpha = 1.5$	$\alpha = 3$
W_{C0}/W_L	0.002	0.002	0.002	0.002	0.002	0.002	0.002	0.002	0.002	0.003	0.003	0.003	0.003
P_{C0}/P_{To}	0.037	0.037	0.048	0.050	0.063	0.064	0.065	0.081	0.081	0.082	0.103	0.104	0.109
W_{C1}/W_L	0.013	0.013	0.016	0.018	0.019	0.018	0.016	0.015	0.015	0.014	0.014	0.013	0.012
P_{C1}/P_{To}	0.064	0.066	0.098	0.110	0.136	0.133	0.118	0.134	0.134	0.126	0.150	0.148	0.133
W_{C2}/W_L	0.019	0.017	0.019	0.013	0.015	0.017	0.014	0.012	0.015	0.011	0.012	0.012	0.009
P_{C2}/P_{To}	0.150	0.133	0.176	0.121	0.170	0.195	0.156	0.157	0.206	0.147	0.193	0.203	0.152
W_{C3}/W_L	0.027	0.027	0.033	0.020	0.023	0.019	0.015	0.020	0.017	0.010	0.017	0.013	0.009
P_{C3}/P_{To}	0.205	0.203	0.298	0.179	0.252	0.209	0.157	0.263	0.225	0.137	0.277	0.205	0.138
W_{D1}/W_L	0.011	0.006	0.006	0.009	0.011	0.011	0.009	0.014	0.012	0.009	0.010	0.008	0.007
P_{D1}/P_{To}	0.087	0.055	0.057	0.080	0.101	0.111	0.094	0.165	0.142	0.106	0.153	0.117	0.095
W_{D2}/W_L	0.033	0.021	0.024	0.011	0.014	0.012	0.011	0.011	0.010	0.011	0.013	0.012	0.011
P_{D2}/P_{To}	0.147	0.101	0.119	0.066	0.092	0.079	0.071	0.089	0.083	0.083	0.110	0.108	0.096
W_{D3}/W_L	0.038	0.030	0.025	0.014	0.016	0.018	0.016	0.014	0.010	0.013	0.015	0.011	0.011
P_{D3}/P_{To}	0.342	0.307	0.287	0.165	0.230	0.259	0.228	0.237	0.153	0.214	0.296	0.217	0.230
$(W_C - W_{BT})/W_L$	0.851	0.859	0.813	0.809	0.776	0.766	0.771	0.732	0.730	0.729	0.686	0.688	0.682
A_{BT}/A_L	0.192												

Table 8.—(Concluded)

Conf. 3	M = 2.5			M = 2.3			M = 2.1			M = 1.9			M = 1.7
	$\alpha = 0$	$\alpha = 1.5$	$\alpha = 3$	$\alpha = 0$	$\alpha = 1.5$	$\alpha = 3$	$\alpha = 0$	$\alpha = 1.5$	$\alpha = 3$	$\alpha = 0$	$\alpha = 1.5$	$\alpha = 3$	$\alpha = 0$
W_{C0}/W_L	0.004	0.004	0.003	0.003	0.003	0.004	0.003	0.003	0.003	0.004	0.005	0.005	0.004
P_{C0}/P_{To}	0.176	0.168	0.158	0.191	0.182	0.241	0.191	0.191	0.191	0.352	0.378	0.395	0.423
W_{C1}/W_L	0.012	0.011	0.011	0.011	0.010	0.012	0.009	0.009	0.010	0.013	0.013	0.013	0.012
P_{C1}/P_{To}	0.172	0.162	0.157	0.203	0.196	0.218	0.230	0.223	0.242	0.352	0.346	0.343	0.406
W_{C2}/W_L	0.010	0.009	0.008	0.010	0.008	0.009	0.009	0.008	0.008	0.007	0.007	0.006	0.006
P_{C2}/P_{To}	0.190	0.183	0.156	0.239	0.195	0.221	0.249	0.223	0.222	0.265	0.261	0.246	0.309
W_{C3}/W_L	0.014	0.010	0.009	0.012	0.008	0.006	0.010	0.006	0.004	0.009	0.008	0.005	0.008
P_{C3}/P_{To}	0.264	0.189	0.171	0.274	0.172	0.146	0.279	0.175	0.151	0.287	0.257	0.198	0.323
W_{D1}/W_L	0.007	0.006	0.006	0.004	0.003	0.007	0.007	0.007	0.007	0.010	0.011	0.012	0.010
P_{D1}/P_{To}	0.124	0.106	0.091	0.093	0.075	0.136	0.184	0.158	0.159	0.307	0.307	0.328	0.364
W_{D2}/W_L	0.013	0.013	0.015	0.017	0.015	0.015	0.013	0.011	0.011	0.015	0.014	0.017	0.016
P_{D2}/P_{To}	0.127	0.119	0.143	0.204	0.179	0.187	0.187	0.182	0.182	0.249	0.280	0.308	0.322
W_{D3}/W_L	0.012	0.010	0.010	0.012	0.009	0.009	0.011	0.008	0.008	0.007	0.006	0.006	0.007
P_{D3}/P_{To}	0.312	0.248	0.256	0.380	0.277	0.252	0.401	0.330	0.301	0.300	0.302	0.264	0.343
$(W_C - W_{BT})/W_L$	0.635	0.635	0.625	0.587	0.593	0.573	0.543	0.551	0.547	0.493	0.494	0.490	0.458
A_{BT}/A_L	0.192												

REFERENCES

1. Syberg, J.; and Hickcox, T. E.: *Design of a Bleed System for a Mach 3.5 Inlet,* NASA CR-2187, January 1973.

2. Smeltzer, D. B.; and Sorensen, N. E.: *Investigation of a Mixed-Compression Axisymmetric Inlet System at Mach Numbers 0.6 to 3.5,* NASA TN D-6078, November 1970.

3. Syberg, J.; and Koncsek, J. L.: *Transonic and Supersonic Test of the SST Prototype Air Intake,* FAA-SS-72-50, April 1972.

4. Koncsek, J. L.; and Syberg, J.: *Transonic and Supersonic Test of a Mach 2.65 Mixed-Compression Axisymmetric Intake,* NASA CR-1977, March 1972.

5. Sakamoto, A. N.; and Hill, D. J.: *Test Report—Large Scale Mach 3.5 Axisymmetric Inlet Test Conducted at NASA-Ames,* D6-42334, The Boeing Company, December 1974.

6. Koncsek, J. L.: *Machine Plot Supplement to D6-42494,* D6-42495, The Boeing Company, April 1975.

7. Reyhner, T. A.: *A Computer Program for Finite-Difference Calculation of Compressible Turbulent Boundary Layers,* D6-23236, The Boeing Company, June 1970.

8. Reyhner, T. A.; and Hickcox, T. E.: "A Procedure for Combined Viscous-Inviscid Analysis of Supersonic Inlet Flow Fields," AIAA Paper 72-44, 17 January 1972.

*U.S. GOVERNMENT PRINTING OFFICE: 1975 - 635-275/4